ABSTRACT

WU, YANG. Signal Processing Tools for MRI Perfusion-Weighted Imaging Data Analysis. (Under the direction of Professor Hamid Krim).

In dynamic susceptibility contrast (DSC) magnetic resonance (MR) approaches, by injecting a bolus of paramagnetic contrast agent intravenously, the measured MR signal is converted to a concentration time course to estimate hemodynamic parameters like cerebral blood flow (CBF), cerebral blood volume (CBV) and mean transit time (MTT).

Before estimating hemodynamic parameters, recirculation effects need to be removed by a gamma-variate fit of the concentration curve. In this dissertation, however, it has been found and demonstrated by simulation that fitting may not discern recirculation from the first-pass in case of cerebral ischemia. A new methodology using temporal independent component analysis (ICA) to remove recirculation in both normal and ischemic brain tissues while preserving the first-pass is therefore proposed. This should improve hemodynamics accuracy particularly in ischemic lesions.

In DSC MR approaches, bolus delays between the arterial input function (AIF) and tissue curves may induce significant CBF quantification error. Our second contribution is using ICA to estimate bolus arrival time for each 5×5 region of interest (ROI) throughout the brain parenchyma. A global AIF measured from a major artery can then be shifted in accordance to define a local AIF for each ROI. The bolus delay may therefore be minimized, and the general shape of the AIF is preserved. This should improve the flow quantification.

Transfer function has been widely used to characterize an unknown system. In DSC MR approaches, vascular transfer function (VTF) represents the probability density function of the vascular transit time. Our third contribution is to propose a new tool to estimate intracranial VTF non-invasively. This should provide an alterative means of assessing tissue perfusion status, particularly in patients with cerebrovascular diseases.

Bolus dispersion between the AIF and tissue curves may induce flow quantification error, which cannot be minimized without the knowledge of vasculature. Our final contribution is to develop an extended cerebral vascular model to minimize delay and dispersion dependence by modelling flow heterogeneity in both bulk small arteries and capillary bed. This should yield more stable flow rates less sensitive to bolus delay and dispersion.

Signal Processing Tools for MRI Perfusion-Weighted Imaging Data Analysis

by

Yang Wu

A dissertation submitted to the Graduate Faculty of
North Carolina State University
in partial satisfaction of the
requirements for the Degree of
Doctor of Philosophy

Electrical Engineering

Raleigh

2005

Approved By:

Dr. Kazufumi Ito	Dr. Weili Lin
Dr. Brian L. Hughes	Dr. Griff Bilbro
Dr. Hamid Krim Chair of Advisory Committee	Dr. Jeffery Macdonald

Dedication

To my husband Lei

and

my parents Zhonghua and Shasha

for their endless love and support

Biography

After entering university at age 15, Yang Wu received her B.S. and M.S. degrees in Radio Engineering from Southeast University, Nanjing, China, in 1997 and 2000 respectively. In Fall 2001, she started her Ph.D study in Electrical Engineering at North Carolina State University, Raleigh, NC. Her research interests are statistical signal/imaging processing particularly medical image analysis.

Acknowledgements

A single tree makes no forest; one string makes no music. A successful team beats with one heart. This thesis is the result of three and half years of work whereby I have been accompanied and supported by many people. It is a pleasant aspect that I have now the opportunity to express my gratitude for all of them.

First, I would like to thank my advisor, Dr. Hamid Krim, whose help, stimulating suggestions and encouragement helped me in all the time of research for and writing of this thesis. I knew him since Fall 2001 when I started my Ph. D study in NCSU. It is Hamid who opened the first door of signal and imaging processing for me. I learned a lot from his courses, "Random Processes" and "Detection and Estimation". From his inspired lectures, I built a solid theoretical background on stochastic signal processing, which is and will be beneficial for my whole life. I joined Hamid's group since Fall 2002. It is Hamid who gave me such a wonderful opportunity to work on so many interesting biomedical signal processing projects. Keeping the idea that my research work may save peoples' lives in mind, I am always motivated and feel proud of my work. Hamid always trusts me and supports me both academically and financially. His enthusiasm and integral view on research has made a deep impression on me. He could not even realize how much I have learned from him.

Second, I would like to thank the other members of my PhD committee who monitored my work and were available when I need their advices: Dr. Griff Bilbro, Dr. Brian L. Hughes, Dr. Kazufumi Ito, Dr. Jeffery Macdonald, and Dr. Weili Lin. I thank you all. Also, my gratitude is owed to Dr. Marc G.Genton, who was on my committee but no longer available due to his move. I benefited from several books recommended by him.

Third, my gratitude goes to Dr. Jeffery Macdonald from Biomedical Department, UNC at Chapel Hill. I knew Jeff since 2002 during my first project on pattern recognition for diagnosing human liver cirrhosis. At that time, I knew nothing about biochemistry or biology, and I never heard of nuclear magnetic resonance imaging or cirrhosis. He introduced this new area to me and is never tiring of responding to my questions and emails.

In addition, the MRI group from UNC at Chapel Hill also supported me in the development of this thesis work. Especially the strict and extensive comments and many discussions with Dr. Weili Lin had a direct impact on the final quality of this thesis. I would like to thank Dr. Hongyu An, for our many discussions and helping me collecting MRI data. I thank Liangsheng for doing the animal surgery.

Especially, I would like to thank the current as well as former students from our group and all my friends whom I have enjoyed spending time with all these years. I would like to thank Xinying particularly for helpful discussions and encouragement.

Last but not the least, I would like to give my special thanks to my best friend Lesly, my husband Lei here, and my parents Zhonghua and Shasha overseas. Although I am going to complete my Ph.D program successfully soon, I feel very guilty for having been too busy to go back to China to visit my parents. Without their endless love, understanding and encouragement, I couldn't go this far in my life and career.

Contents

List of Figures

List of Tables

List of Abbreviations

ADC	Apparent diffusion coefficient
AIF	Arterial input function
AUC	Area underline the receiver operating characteristic curve
BBB	Blood-brain barrier
BIC	Bayesian information criterion
CBF	Cerebral blood flow
CBV	Cerebral blood volume
CGAIF	Contralateral global arterial input function
cMCA	Contralateral middle cerebral artery
CSF	Cerebral spinal fluid
cSVD	Singular value decomposition deconvolution with a block-circulant matrix
DSC	Dynamic susceptibility contrast
DTPA	Diethylenetriaminepentaacetic acid
DWI	Diffusion-weighted imaging
EM-ICA	Expectation maximization independent component analysis
EPI	Echo planar imaging
EVTF	Power of the first mode of the vascular transport function
FN	False negative
FOV	Field-of-view
FP	False positive
FPR	False positive ratio
FWHM	Full-width-half-maximum
GAIF	Global arterial input function

IC	Independent component
ICA	Independent component analysis
IGAIF	Ipsilateral global arterial input function
ICAML	Infomax algorithm with a maximum likelihood formulation analysis
iMCA	Ipsilateral middle cerebral artery
LAIF	Local arterial input function
MCA	Middle cerebral artery
MRI	Magnetic resonance imaging
MTT	Mean transit time
NRM	Nuclear magnetic resonance
PCA	Principal component analysis
PWI	Perfusion-weighted imaging
RD	Relative dispersion
rMTT	Relative mean transit time
ROC	Receiver operating characteristic
ROI	Region of interest
rrCBV	Relative regional cerebral blood volume
SNR	Signal-to-noise ratio
SSE	Sum of squared error
SVD	Singular value deconvolution decomposition
TE	Echo time
TH	Slice thickness
TN	True negative
TOI	Tissue of interest
TP	True positive
TPR	True positive ratio
TR	Repetition time
TTA	Time to arrival
TTP	Time to peak
VTF	Vascular transport function

Chapter 1

Introduction

1.1 Magnetic Resonance Imaging

Studying characteristics of *in vivo* tissues in a human body has been a big challenge over the last century. Magnetic resonance imaging (MRI) is the use of nuclear magnetic resonance (NMR) phenomenon to study biological properties of *in vivo* tissue. It has been developed maturely and as a consequence, MRI is routinely applied on clinical diagnosis and scientific research.

Only nuclei with spin quantum number $I \neq 0$ can absorb/emit electro-magnetic radiation, thereby providing nuclear magnetic resonance spectra. The spin states of the nucleus or the so called magnetic quantum number, m, are quantified as

$$m = \{I, (I-1), (I-2), \cdots, -I\}. \tag{1.1}$$

For example, for the most common and biologically relevant nuclei like H^1, $m = \{1/2, -1/2\}$, which means that only two energy levels can be taken by hydrogen.

The human body is primarily made of fat and water. Fat and water have so many hydrogen atoms that the human body is approximately 63% hydrogen atoms. Since hydrogen nuclei are abundant in human body and hydrogen has a NMR signal, MRI primarily images the NMR signal from the hydrogen nuclei in human body. We will focus the discussion on hydrogen nuclei with $I = 1/2$.

Magnetic moment, μ, is a vector quantity that gives the direction and magnitude of the "nuclear magnet", and may be expressed as

$$\mu = \gamma I h/2\pi, \tag{1.2}$$

where h is the Planck constant, and γ is the gyromagnetic ratio depending on the nature of each nucleus.

In the ground state all hydrogen nuclear spins are disordered, and there is no energy difference between them. Since they have a magnetic moment, as shown in Fig. 1.1, once we apply a strong external magnetic field B_0, they can align in either the same direction or in the opposite direction of the external magnetic field. This creates an energy difference between nuclei aligned with and against B_0. The energy difference is related to the resonance frequency ν given by $\nu = \gamma B_0/2\pi \quad (Hz)$.

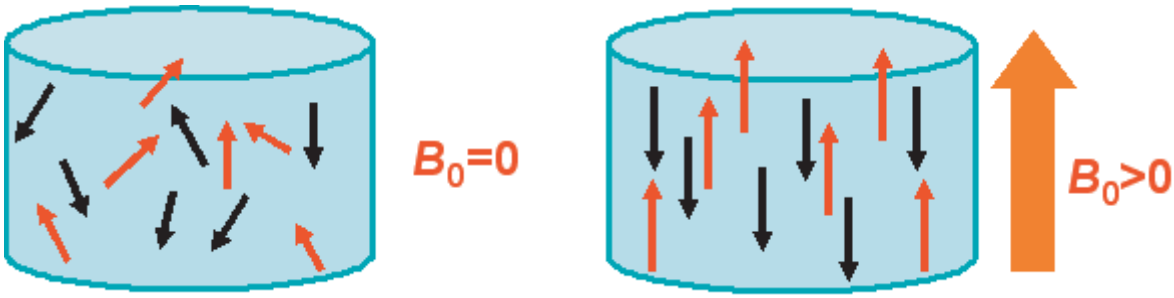

Figure 1.1: Effect of an external magnetic field on hydrogen nuclei

Assume a hydrogen nucleus spins around its z axis. Now, if we put it in an external magnetic field B_0, the interaction between the magnetic moment μ and B_0 will generate a torque. Since the nucleus is spinning, there are two forces acting on it. One that wants to bring it towards B_0 and the other wants to keep it spinning. As shown in Fig. 1.2, μ ends up precessing around B_0. The frequency at which μ precesses around B_0 or the Larmor frequency, ω_0, is defined as

$$\omega_0 = 2\pi\nu = \gamma B_0 \quad (rad/s). \tag{1.3}$$

Fig. 1.3 shows the effects on the macroscopic magnetization where contributions from different nuclei have been averaged. We can decompose the magnetic moment of each

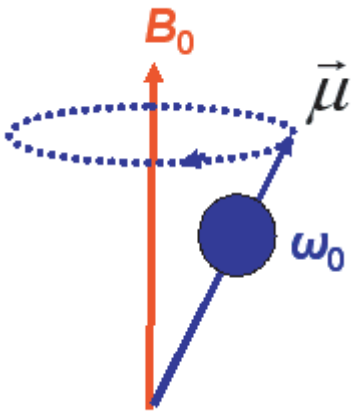

Figure 1.2: Precession

nucleus into a z contribution and an xy plane contribution. The components in the xy plane are randomly distributed and hence cancel out. Those in the z direction, yield a net magnetization M_0 proportional to the population difference.

By letting the system absorb energy to affect the spin population, we are able to take the magnetization away from this condition and observe how it goes back to equilibrium. The energy source is an oscillating electromagnetic radiation generated by an alternating current. Let B_1 be the oscillating magnetic field created by the alternating current and it points perpendicular to the static field B_0. When the frequency of the alternating current is equal to the Larmor frequency, ω_0, then we achieve a resonant condition. The tiny alternating magnetic field and M_0 interact, generating a torque on M_0, and the system absorbs energy. As illustrated in Fig. 1.4, since the system absorbs energy, which results in modification of the populations of the energy levels, the equilibrium of the system is altered. As a result, M_0 is taken away from the direction of B_0 to the xy plane and it precesses about B_0 and B_1. The final position of the magnetization depends on the length of time that B_1 is applied. In the absence of the external magnetic field B_1, M_{xy} will try to return to M_0, a phenomenon referred to as "relaxation". The oscillation of M_{xy} generates a fluctuating magnetic field which can generate a current in the receiver coil.

The mechanism that brings the magnetization M_{xy} back to the equilibrium state M_0 is called relaxation. There are two types of relaxation, and both are time-dependent

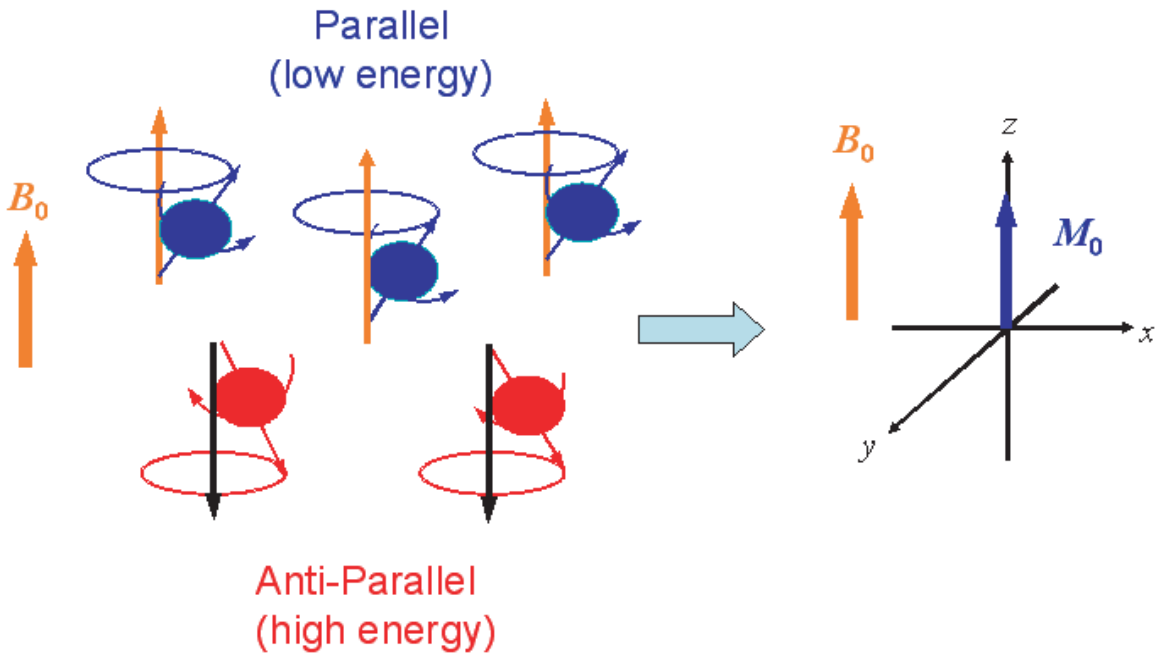

Figure 1.3: Bulk magnetization

exponentially decaying processes.

The first one, called longitudinal (or spin-lattice) relaxation, is the result of the interaction between the spins and the surroundings (or "lattice"). This energy loss brings the magnetization components aligned with the z axis, M_z, back to the equilibrium state M_0. The longitudinal time constant T_1 or the relaxation rate $R_1 = 1/T_1$ determines how fast magnetization returns to the orientation with the main magnetic field as reflected by $M_z = M_0(1 - e^{-t/T_1})$.

The other one is called transverse (or spin-spin) relaxation. It dephases the components of magnetization lying on the xy plane (M_{xy}) by spin-spin interactions and thus brings the transverse magnetization to their equilibrium value of zero. This transverse magnetization should decay at least as fast as the longitudinal magnetization relaxes to the z axis. However, since the spin-spin interaction does not necessarily require any change in energy, the transverse magnetization may relax to its zero equilibrium value faster than the relaxation rate of the longitudinal relaxation. The transverse time constant or the relaxation rate $R_2 = 1/T_2$ determines how fast the transverse magnetization varnishes as

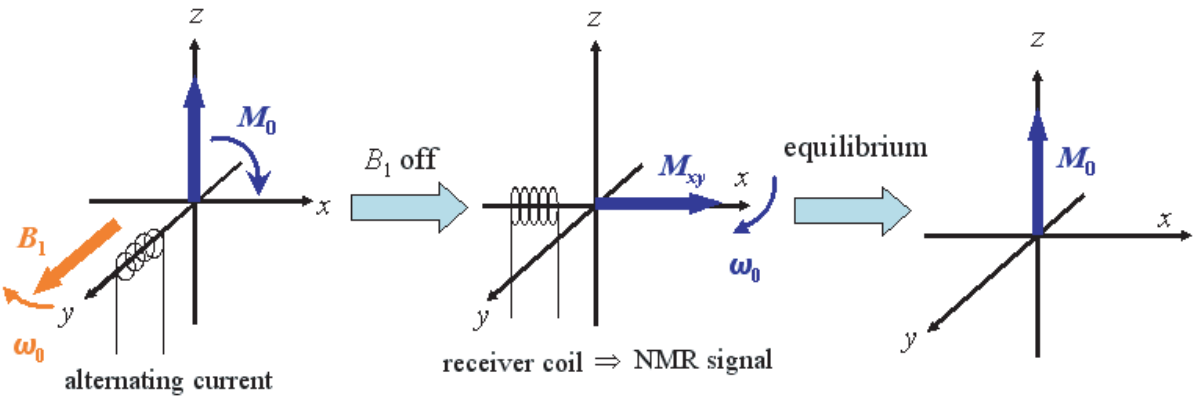

Figure 1.4: NMR excitation

reflected by $M_{xy} = M_0 e^{-t/T_2}$ as illustrated in Fig. 1.5.

Different tissues have different T_1 or T_2 relaxation times. For example, the longitudinal and transverse relaxation times of gray matter differ from those of white matter and cerebral spinal fluid (CSF). This can give us different image contrast among different *in vivo* tissues.

1.2 Dynamic Susceptibility Contrast Perfusion-weighted Imaging

Perfusion refers to the delivery of blood at the capillary level, where exchange of oxygen and nutrients between blood and tissue takes place. It is measured by volume in milliliters of blood delivered to 100g of tissue per minute.

Dynamic susceptibility contrast (DSC) approaches have been widely utilized in the study of tissue perfusion. DSC Magnetic resonance (MR) perfusion-weighted imaging (PWI) uses signal loss resulting from the susceptibility effect of the intravascular paramagnetic tracers to derive various hemodynamic quantities.

In a DSC experiment, we inject a bolus of paramagnetic contrast agent (for example, Gd-DTPA) into the brain. The tracers remain intravascular in the capillaries. The presence of intravascular paramagnetic contrast agent induces a large susceptibility dif-

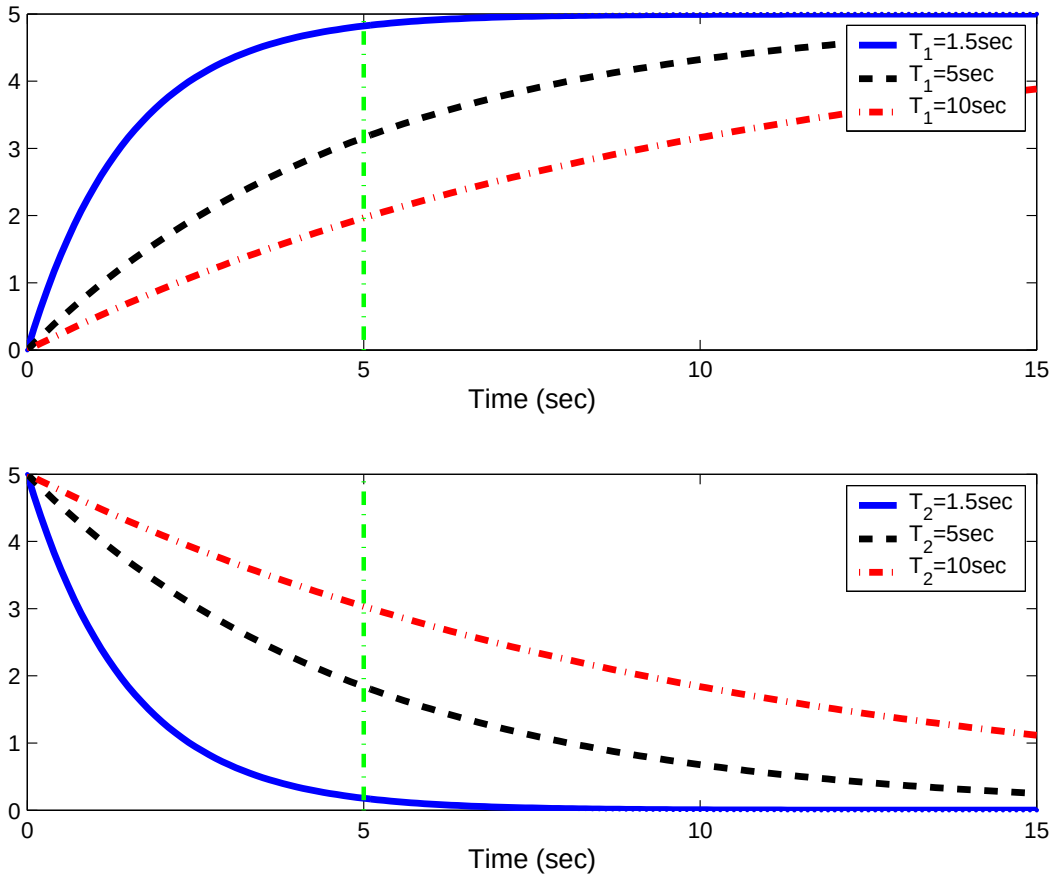

Figure 1.5: Longitudinal and transverse Relaxation

ference between the capillaries containing the paramagnetic tracers and the surrounding tissues, yielding strong local field gradients in the neighborhood of the vessel walls. As a result, spins will process at different frequencies depending on their locations. The presence of signal dephasing results in shortening of the proton spin relaxation times or in increasing of the relaxation rates as follows:

$$\begin{cases} R_1(t) = R_1^{(o)} + \Delta R_1(t), \\ R_2(t) = R_2^{(o)} + \Delta R_2(t), \end{cases} \tag{1.4}$$

where R_1 and R_2 are respectively the longitudinal and transverse relaxation rates, and $R_i^{(o)}$ is the original relaxation rate (i=1,2), while $R_i(t)$ is the relaxation rate after contrast agent injection (i=1,2).

The effects of diffusion as well as local magnetic field extend the effects of T_2 interaction. We can use this large signal change to monitor a contrast agent bolus passing through the brain.

Upon injecting a paramagnetic contrast agent in the blood, a susceptibility MR signal drop due to the first passage of the contrast agent through the brain tissue follows. For normal volunteers, there is no difference between the two brain hemispheres as shown in Fig. 1.6.

Acute ischemic stroke refers to stroke caused by the formation or the presence of a blood clot within a blood vessel, or the sudden obstruction of a blood vessel by an abnormal particle circulating in the blood. For acute stroke patients, damaged brain tissues with reduced perfusion (e.g., ischemic tissue marked by the arrows in Fig. 1.7) only allow passage of a small amount of contrast agent and therefore remain bright during the bolus passage. DSC perfusion images thus can yield useful physiological information to detect ischemic lesion.

By rapidly acquiring images prior to, during and after the injection of a contrast agent, the temporal signal changes induced by the presence of the contrast agent may be obtained. These typically consist of a baseline signal, a first passage and a recirculation of the contrast agent as shown in Fig.1.8. The baseline signal is measured before the tracers arrive in the region of interest (ROI). Once the tracers arrive in the ROI, a large signal loss due to the signal dephasing is observed. As the tracers flow out of the ROI, the signal intensity will eventually return to the baseline. The extent of the signal recovery depends on the extent of the re-enter of the tracers into the ROI. This re-enter effect is called "recirculation".

Villringer *et al.* [1] have experimentally shown that the susceptibility MR signal intensity due to a bolus of tracers such as Gd-DTPA is reflected by

$$S(t) = S_0 \cdot e^{-TE \cdot \Delta R_2(t)}, \tag{1.5}$$

where S_0 is the baseline signal, TE is the echo time of the used sequence and $\Delta R_2(t)$ is the change in R_2 relaxation rate due to the presence of the contrast agent. In order to compute various hemodynamic parameters, we need to convert the measured MR signal intensity variations to changes in the tracer concentration, $C(t)$, as illustrated in Fig.1.9.

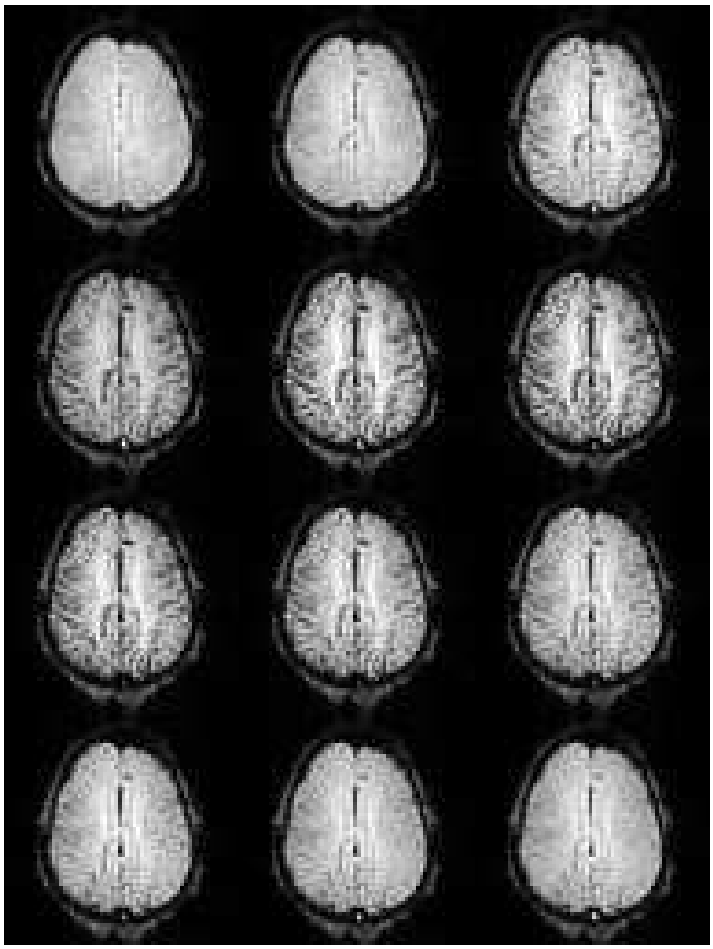

Figure 1.6: DSC perfusion images of a healthy volunteer. During the bolus passage, a MR signal drop can be visualized. After the bolus passage, the signal returns to normal.

$$C(t) = \kappa \Delta R_2 = -\frac{\kappa}{TE} \ln\left(\frac{S(t)}{S_0}\right) \tag{1.6}$$

where $S(t)$ is the susceptibility signal intensity measured in the ROI at time t, κ is a constant depending on the tissue, contrast agent, field strength and the pulse sequence parameters, and $C(t)$ is the concentration of tracers in the ROI at time t.

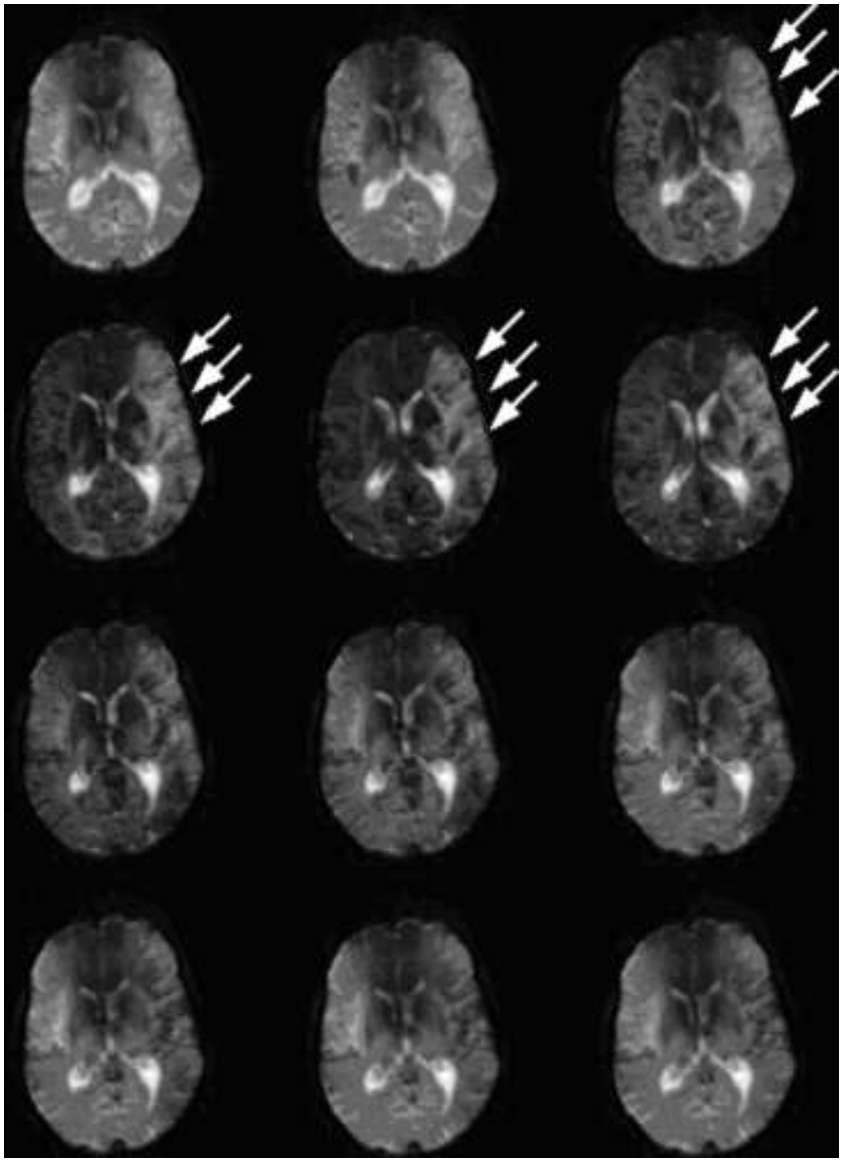

Figure 1.7: DSC perfusion images of an acute stroke patient. Within the ischemic lesion territory marked by the arrows, the MR signal drop is much less than that in the contralateral normal hemisphere.

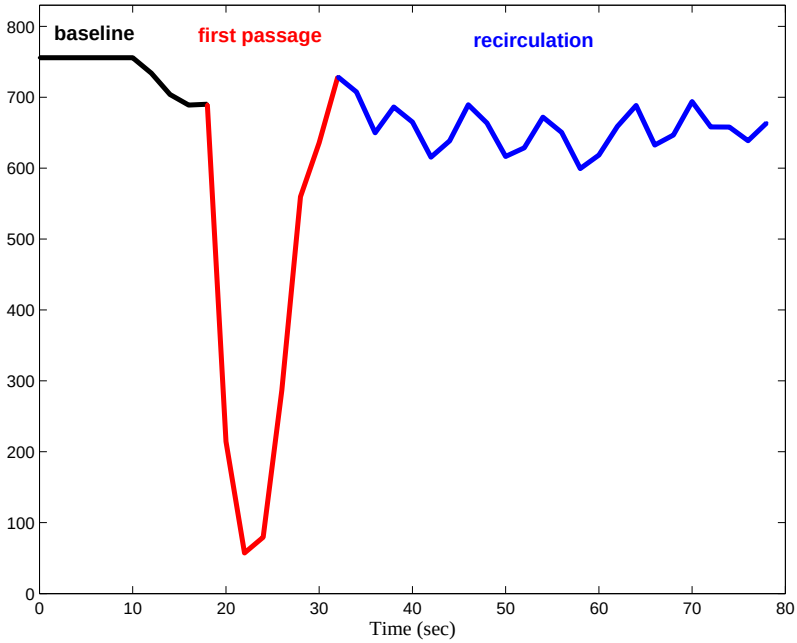

Figure 1.8: MR susceptibility signal variation

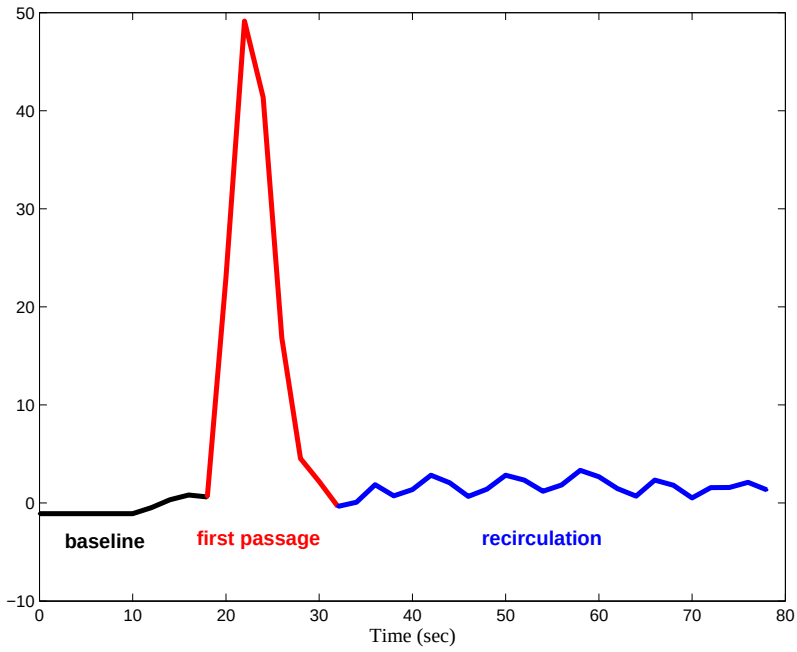

Figure 1.9: Tissue concentration curve

1.3 Perfusion Quantification Model

When we compute hemodynamic parameters, only the first pass of the contrast agent through the brain tissues should be considered. Recirculation effects therefore need to be removed prior to estimating hemodynamic parameters. In the subsequent discussion of hemodynamic quantification model, we assume the recirculation effects are eliminated in concentration curves.

The perfusion quantification model is based on tracer kinetics for a bolus of non-diffusible tracers, and on the assumption that the contrast agent remains intravascular due to the intact blood-brain barrier (BBB). An intact BBB protects the brain from unwanted chemicals or large molecules, as well as most systematically delivered therapeutic agents, in the blood stream.

Assume an ideal instantaneous unit bolus injection, and suppose Q mg of contrast agent is injected at time $t = 0$. Each tracer particle has a different path and hence a different transit time through the tissue of interest (TOI). Also assume that as $t \to \infty$, the contrast agent will flow out of the TOI. Let F be the average volume of blood delivered to 100g of brain TOI per minute, and $C_v(t)$ be the concentration of the contrast agent at the venous output of the TOI. During a short time period $[\tau, \tau + d\tau]$, the outgoing blood flow is $Fd\tau$ ml. At time τ, $Fd\tau C_v(\tau)$ mg contrast agent flows out the TOI. When $\tau \to \infty$, all tracers should leave the TOI, i.e. $Q = \int_0^\infty Fd\tau C_v(\tau)$. The rate that the tracer leaving the VOI at time t may thus be defined as $h(t) = \frac{FC_v(t)}{\int_0^\infty Fd\tau C_v(\tau)}$.

The transport function $h(t)$ defines the probability density function of the transit times. During $[\tau, \tau + d\tau]$, the fraction of the tracer injected at $\tau = 0$ that leaves the TOI is $h(\tau)d\tau$. At time t, the fraction of the tracer injected at $t = 0$ that leaves the system is thus $\int_0^t h(\tau)d\tau$. The residue function $R(t)$, in contrast, refers to the fraction of injected contrast agent that entered the TOI at $t = 0$ which is still present in the TOI at time t. $R(t)$ is related to $h(t)$ by

$$R(t) = 1 - \int_0^t h(\tau)d\tau. \tag{1.7}$$

From Eq. (1.7), ideally $R(t)$ is a decreasing nonnegative function with $R(0) = 1$.

In practice, the tracers enter the TOI as some function of time, $C_a(t)$ mg/ml, other than a delta function. The concentration of tracers in the venous output of the TOI, $C_v(t)$, is determined by the arterial input function (AIF) $C_a(t)$ and the transport function $h(t)$ as

Eq. (1.8).

$$C_v(t) = \int_0^t C_a(\tau)h(t-\tau)\,d\tau = C_a(t) * h(t), \tag{1.8}$$

where $*$ denotes linear convolution.

It has been shown that the residual tracer concentration within the TOI is given by [2]:

$$C_{TOI}(t) = F \cdot \int_0^t C_a(\tau)R(t-\tau)\,d\tau. \tag{1.9}$$

Eq.(1.9) can be derived as follows. At time t, the amount of tracer remaining in the TOI is given by

$$Q_{TOI}(t) = F\int_0^t C_a(\tau)d\tau - F\int_0^t C_v(\tau)d\tau. \tag{1.10}$$

We hence, have,

$$\begin{aligned} Q_{TOI}(t) &= F\int_0^t C_a(\tau) * (\delta(\tau) - h(\tau))d\tau = F\int_0^t C_a(\tau) * \left(1 - \int_0^t h(\tau)d\tau\right)' d\tau \\ &= F\int_0^t C_a(\tau) * R(\tau)d\tau. \end{aligned} \tag{1.11}$$

F is not an absolute flow, but rather a relative flow in a specific TOI with volume of V ml. $Q_{TOI}(t)$ can thus be viewed as the relative mass of the tracer (mg) remaining in a TOI with volume of V ml, i.e. it can be approximately viewed as the residual concentration of the tracers in the system, $C_{TOI}(t)$ mg/ml.

Eq. (1.11) may also be viewed as follows: During a short period $[t-\tau, t-\tau+d\tau]$, the flow is $Fd\tau$ ml, and $Fd\tau C_a(t-\tau)$ mg of tracer is injected in the TOI. After a period of τ time units is elapsed, the fraction of the tracer injected at $t-\tau$ that is still present in the TOI at time t is $R(\tau)$. For those tracers injected at $t-\tau$, $Fd\tau C_a(t-\tau)R(\tau)$ mg tracer remains in the system. At time t, hence $Q_{TOI}(t) = F\int_0^t C_a(t-\tau)d\tau R(\tau)d\tau$ mg tracer remains in the TOI.

Cerebral blood flow (CBF) is measured by volume in milliliters of blood delivered to 100g of tissue per minute. As shown in Eq. (1.9), it may be obtained through the deconvolution of the tissue concentration with an appropriately selected AIF.

Cerebral blood volume (CBV) is the fraction of the total tissue volume within a voxel occupied by blood (ml/100g tissue). For an intact blood-brain barrier, CBV may be computed [3, 4] as

$$CBV = \frac{\int C(t)\,dt}{\int C_a(t)\,dt}. \tag{1.12}$$

Mean transit time (MTT) is the average time required for any given particle of tracer to pass through the tissue. It can computed using the transport function and is given by

$$MTT = \int_0^\infty th(t)\,dt. \tag{1.13}$$

CBF, CBV and MTT are related by the central volume theorem [3, 4] given by

$$MTT = CBV/CBF. \tag{1.14}$$

From Eq. (1.12), CBV can be estimated straightforwardly if the AIF $C_a(t)$ is known. However, sometimes one is interested in a relative CBV without the knowledge of $C_a(t)$. The relative regional cerebral blood volume (rrCBV) may be computed as the area under $C(t)$ [5, 6] as shown in Fig. 1.10 and given by

$$rrCBV = \int C(t)\,dt \tag{1.15}$$

1.4 MRI Data Acquisition

Throughout this thesis, images were respectively acquired at a 3T scanner (Allegra, Siemens Medical Systems Inc.) and at a 1.5T scanner (Vision, Siemens Medical Systems Inc.) for the normal volunteer and the acute stroke patient studies. All experimental protocols were approved by the institutional review board and written informed consent was obtained prior to imaging studies. The acute stroke patients were recruited as part of the clinical trials for neuroprotective agents. For the normal volunteer study, a single shot T_2^*-weighted echo planar imaging (EPI) sequence was used to acquire DSC images. The imaging parameters were as follows: repetition time (TR) = 1.5 sec; echo time (TE) = 28 msec; field-of-view (FOV) = 220×220 mm^2; acquisition matrix = 64×64; slice thickness

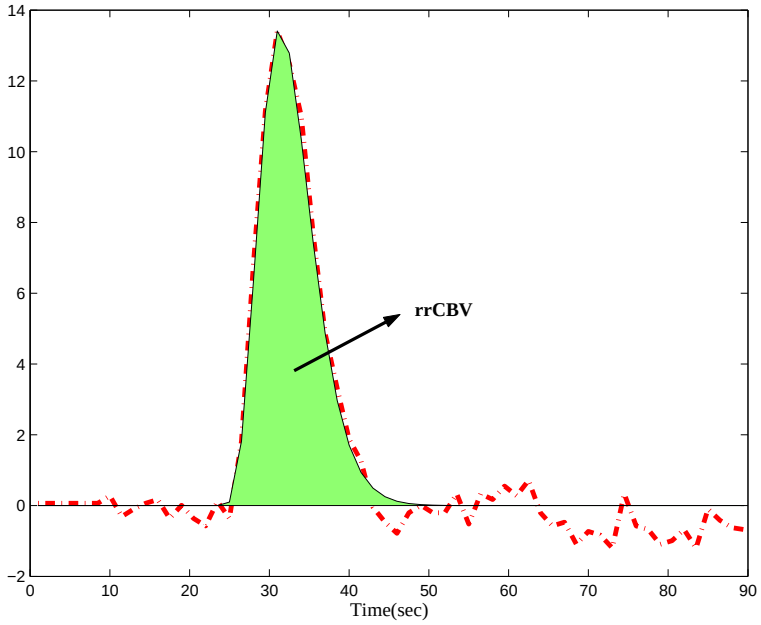

Figure 1.10: Relative regional cerebral blood volume

(TH) = 5 mm and interslice gap = 1.5 mm. A total of 12 slices were acquired. This sequence was also used for patient studies with the exception that TR and TE were 2 sec and 54 msec, respectively. The DSC perfusion sequence was repeated 60 and either 40 or 50 times for the normal volunteer and patient studies, respectively. The contrast agent (Gd-DTPA, 0.1 mmol/kg) was injected by hand, at a rate of $\sim$ 2ml/s, after the completion of 5^{th} scan while subjects laid still inside the magnet.

In addition to DSC images, diffusion-weighted imaging (DWI) and T_2-weighted images were also acquired for acute stroke patients. DWI images with $b = 0$ and $b = 1000\ s/mm^2$ along all three main axes were acquired and subsequently trace apparent diffusion coefficient (ADC) maps were calculated. The imaging parameters for the DWI sequence were as follows: TR = 2 sec; TE = 100 msec; TH = 7 mm; FOV = $240 \times 240\ mm^2$ and 20 slices. All patients were imaged three times with the first time point (tp1) occurring within 6 hours, the second time point (tp2) within 3-5 days, and the third time point (tp3) taking place 1 or 3 months after symptom onset. The follow-up T_2-weighted images consisted of 12 slices (TH = 6 mm, interslice gap = 1 mm, FOV = $220 \times 220\ mm^2$ and acquisition matrix = 256×256). The DSC and DWI images acquired at tp1 and tp2 were

spatially coregistrated to the follow-up tp3 T_2-weighted images[1].

1.5 Motivation

Stroke is the third lead cause of death in the United States. For an acute stroke, prompt medical attention is very important. Thrombolysis is the use of drugs to dissolve blood clots. Research suggests that when used to treat stroke, thrombolysis can prevent paralysis and other problems that otherwise might result. For thrombolysis to be effective in treating strokes, prompt medical attention is crucial. For an acute stroke, the use of thrombolysis within 3 hours after symptom onset is an established therapy. Usage beyond that time window is still a matter of debate. In many parts of the world, including the United States, most stroke patients reach hospital long after 3 hours or even 6 hours. There are about 616,000 ischemic stroke occurrences in the United States each year, and only a small percentage of patients presenting with an acute stroke ever receive thrombolysis.

Advanced MRI techniques can provide diagnostic imaging information for stroke patients. Compared to conventional CT or MRI T_2-weighted images, DSC perfusion-weighted images can yield various cerebral hemodynamic parameters such as CBF, CBV and MTT which are highly sensitive in diagnosing acute cerebral ischemia.

As shown in Fig. 1.11, prior to estimating hemodynamic parameters, recirculation effects need to be removed from the tissue concentration curve. Since conventional approaches such as gamma-variate fitting cannot effectively minimize recirculation effects especially in case of a reduced MR signal change and a temporal overlap between the first and subsequent passages of the contrast agent, hemodynamic parameters such as CBV may be over- or under-estimated as it is directly proportional to the area underlying the tissue concentration curve. For this reason, a better method that is capable of effectively removing recirculation is highly desirable.

After recirculation effects are removed, CBF can be estimated by deconvolving the tissue concentration curve with an appropriately selected arterial input function as shown by Eq.(1.9). Normally a global AIF measured in large vessels such as middle cerebral artery (MCA) is used to estimate CBF for all brain voxels. This global AIF may lead or lag some tissue curves, which inevitably induces delays between the global AIF and tissue concen-

[1] An automated image registration software package, AIR 5.2.5 (University of California at Los Angeles) [7, 8] using an affine, 12-parameter transformation model and trilinear interpolation was used for coregistration.

tration curves. It has been shown that bolus delay, particularly in patients with cerebral ischemia, will lead to inaccurate estimates of CBF using singular value decomposition deconvolution (SVD) for images obtained with the DSC approaches. The bolus delay, thus, need to be eliminated to obtain an accurate estimation of CBF.

Analysis of the transfer function has been widely used to characterize an unknown system. In DSC MR approaches, vascular transfer function (VTF) represents the probability density function of the vascular transit time. The ability to estimate the intracranial VTF non-invasively should potentially provide highly relevant physiological information, particularly in patients with cerebrovascular diseases.

It has been shown that bolus delay and dispersion between the AIF and tissue curves may induce flow quantification error by SVD. Although bolus delay may be minimized, bolus dispersion may not be corrected without the knowledge of vasculature of the blood vessel bed.

It is, therefore, necessary to find an alternative method to remove recirculation effects while preserving the first passage of the contrast agent for DSC perfusion data acquired from both normal volunteers and acute stroke patients. In addition, approaches to correct bolus delay are needed to obtain an accurate estimate of CBF. Moreover, methodology to estimate intracranial vascular transfer function non-invasively is of great interest. Furthermore, vascular models describing cerebral flow heterogeneity in both small arteries and capillary bed should yield more stable CBF quantification comparing to the SVD approach. This thesis aims to develop a novel methodology to effectively remove recirculation, techniques to correct bolus delay on flow estimation, as well as method to non-invasively estimate intracranial VTF and a modified vascular model to describe cerebral flow heterogeneity. This should improve estimation of hemodynamic parameters as well as provide an alterative means of assessing tissue perfusion status, and thus yield more accurate delineation of acute perfusion abnormality.

1.6 Main Contributions

In Chapter 2, we propose a novel methodology to remove recirculation effects in dynamic susceptibility contrast MRI images using temporal independent component analysis. Assuming the first-pass and the recirculation of the contrast agent may be distinguished

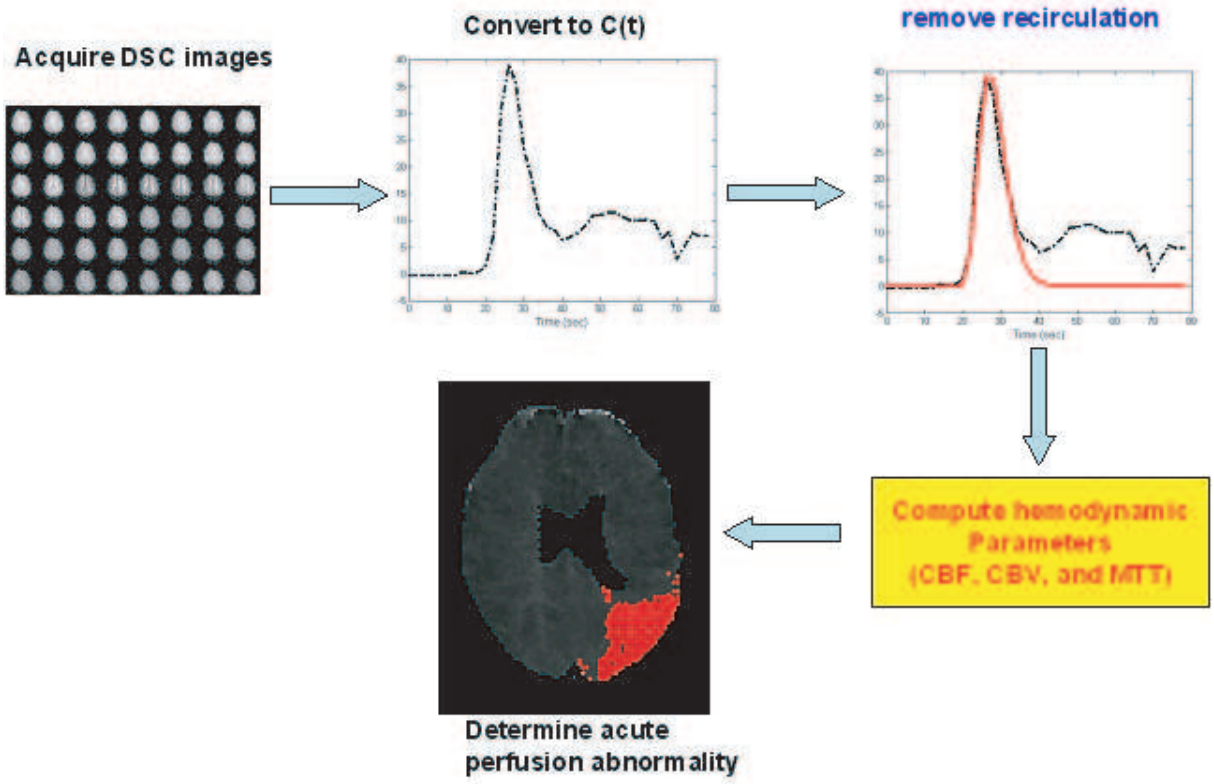

Figure 1.11: Clinical application of DSC perfusion imaging

as different temporally independent components, recirculation may be eliminated from the temporal tissue curves. The capability to accurately remove effects of recirculation while preserving the first-pass even when they are overlapped, should further improve the accuracy of DSC MRI for obtaining cerebral hemodynamics.

In Chapter 3, an alternative approach to correct bolus delays between the global arterial input function and tissue curves on cerebral blood flow quantification is proposed. The correct bolus arrival time may be obtained based on temporal independent component analysis of DSC MRI images. By shifting the global AIF to the correct bolus arrival time for each 5×5 region of interest, the general characteristics of AIF is preserved, while the bolus delays may also be corrected. More accurate estimation of cerebral blood flow using SVD may be obtained.

In Chapter 4, a novel tool to non-invasively estimate VTF based on spatial independent component analysis is proposed. Local arterial input function may be constructed

by applying spatial independent component analysis to DSC MRI data. Voxel-by-voxel VTF may be subsequently estimated through the deconvolution of the local AIFs with a global AIF using SVD but with a block-circulant matrix (cSVD). The VTF may offer an alterative means of assessing tissue perfusion status.

In Chapter 5, a modified vascular model is developed to model cerebral flow heterogeneity using normal rat cerebral MR data. Not only the vasculature between the major vessel and any local vessel, but also the vasculature between any local vessel to the tissue of interest may be modelled. By modelling the blood flow heterogeneity in small arteries, as well as in the capillary bed, more stable flow rates may be obtained in comparison to the conventional SVD approach.

In Chapter 6, we provide some extensions and new research arenas for future work.

Chapter 2

Recirculation Removal in Dynamic Susceptibility Contrast MRI

In DSC perfusion-weighted imaging, effects of recirculation are normally minimized by a gamma-variate fitting procedure on the concentration curves prior to estimating hemodynamic parameters. The success of this method, however, hinges largely on the extent to which MR signal is altered in the presence of a contrast agent and a temporal separation between the first and subsequent passages of the contrast agent. Moreover, important physiological information might be compromised by imposing an analytic equation on all measured concentration curves. We propose to exploit independent component analysis [9] to minimize effects of recirculation in DSC. Results obtained from simulation, normal healthy volunteers and acute stroke patients demonstrate that such a technique can greatly minimize the effects of recirculation despite a substantial overlap between the first passage and recirculation. This in turn should improve estimation of cerebral hemodynamics particularly when an overlap between the first passage and recirculation is suspected as in the case of an ischemic lesion.

2.1 Introduction

Dynamic susceptibility contrast approaches have been widely utilized in the study of tissue perfusion [2, 10–16]. In a DSC experiment, a bolus of paramagnetic contrast agent (for example, Gd-DTPA) is injected intravenously, and its passage through blood vessels induces signal reduction when a T_2^*/T_2-weighted sequence is used. By rapidly acquiring images prior to, during and after the injection of a contrast agent, temporal signal changes induced by the presence of the contrast agent can be measured. MR susceptibility signal change is subsequently converted to a relative concentration time course. Finally, various post-processing approaches such as SVD [2], are used to estimate CBF, CBV and MTT.

While approaches to estimate these physiological parameters differ, they share a common goal of removing the effects of recirculation so that a more accurate estimate of cerebral hemodynamics may be obtained. To this end, fitting the concentration time curves to a gamma-variate function [17, 18] has been one of the most commonly employed approaches. Although widely utilized, this approach has two major limitations. One primary limitation is that the success of this approach hinges largely on the extent to which MR signal is altered in the presence of a contrast agent and on a temporal separation between the first and subsequent passages of the contrast agent. When normal and young volunteers are studied, these two requirements are easily fulfilled, making it straightforward to separate the first passage from the recirculation. In contrast, substantially broadened concentration curves with a reduced signal change may be present in patients with cardiovascular and/or cerebrovascular diseases. Under such condition, it can be a challenge to effectively minimize recirculation by fitting a gamma-variate function to the concentration time curve. Another limitation of this approach is that important physiological information may potentially be lost by imposing an analytic equation on all measured concentration time curves. New approaches capable of minimizing effects of recirculation while preserving the original characteristics of the concentration time curves are therefore warranted.

Independent component analysis (ICA) has been widely used to determine underlying independent signal sources from observed data with minimal knowledge of the sources [9, 19–24]. This blind source separation method has previously been used to identify regions of activation in functional magnetic resonance imaging [25–31], to remove large vessel effects [32] and to define local arterial input functions [33] in DSC MRI images, to segment different brain tissues [34], and to remove artifacts and random noise in diffusion

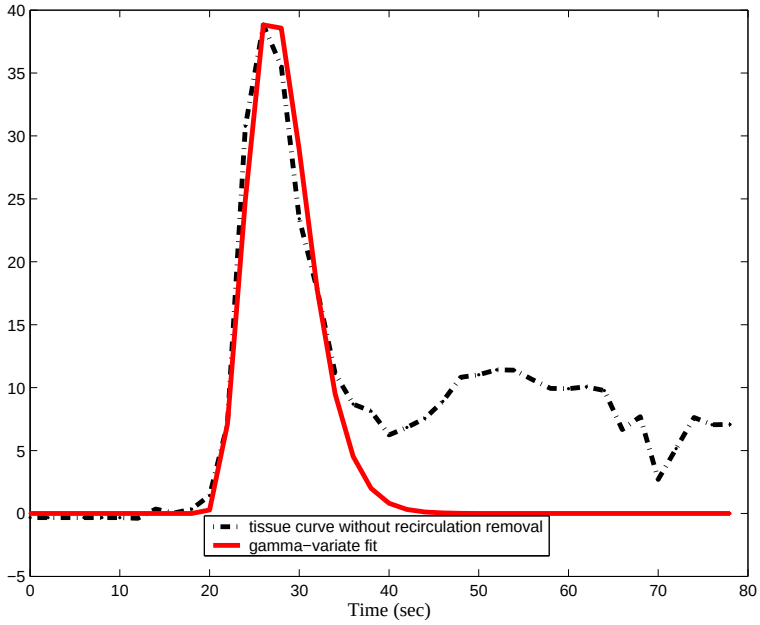

Figure 2.1: Fitting the tissue curve with a gamma-variate function to remove recirculation

tensor images [35]. Assuming that the concentration time curves are linear superpositions of MR signal changes arising from contributions such as arteries, veins, tissue, recirculation and noise, we propose to use ICA to minimize effects of recirculation in DSC experiments. Results from simulation, normal volunteers and acute stroke patients will be provided to demonstrate the effectiveness of this ICA approach.

2.2 Previous Work: Gamma-variate Fitting

As illustrated in Fig. 2.1, the concentration curves are normally fitted by a gamma-variate function as proposed in [17,18] in an attempt to remove recirculation [16]. And the gamma-variate function is given by:

$$C_\Gamma(t) = \begin{cases} A(t-t_0)^B e^{-D(t-t_0)} & t_0 \le t \\ 0 & \text{otherwise,} \end{cases} \tag{2.1}$$

where t_0 is the time for the tracers to arrive in the tissue of interest, which is also called "time to arrival" (TTA).

For better efficiency and a reduction in complexity for gamma-variate fitting, a

logarithmic transformation may first be applied to each tissue concentration curve prior to fitting. The time to the peak (TTP) is first estimated as the transformed concentration curve reaches its maximum. A linear model of $\log C_\Gamma(t)$ defined in Eq.(2.2) up to the right turning point may be obtained in the least square sense using the Levenberg–Marquardt method [36–38],

$$\log C_\Gamma(t) = \begin{cases} \log A + B \cdot \log(t - t_0) - D(t - t_0) & t_0 \le t \\ 0 & \text{otherwise.} \end{cases} \tag{2.2}$$

The left and right turning points of transformed concentration curve are estimated to lie in the half maximum before and after TTP, respectively. The initial estimates for the fitting parameters can be obtained as follows: An initial guess for the TTA of the bolus, $t_0^{(0)}$, may be estimated by searching from TTP backward for two successive values which are smaller than 10% of the maximum. Fitting parameters, $\log A^{(0)}$, $B^{(0)}$, and $D^{(0)}$, are estimated such that the maximum and the turning points of $\log C_\Gamma(t)$ correspond to the maximum and the turning points of the logarithm transformed concentration curve. Upon convergence, each fitted curve may be extrapolated from the right turning point to the end, and then transformed back using an exponential transformation to obtain the fitted forward concentration curve.

This approach, however, has several drawbacks. First, the success of this approach hinges largely on the extent to which MR signal is altered in the presence of a contrast agent and on a temporal separation between the first and subsequent passages of the contrast agent. For example, a DWI image of an acute stroke patient is shown in Fig. 2.2(a), delineating the presence and extent of the acute ischemic lesions[2]. The red dot indicates a voxel randomly selected from the ipsilateral hemisphere[3]. Similarly, the follow-up T_2-weighted image of the same patient is shown in Fig. 2.2(b), delineating the presence and extent of the final infarction[4]. The tissue concentration curve without recirculation removal (dash-dot line) and its gamma-variate fit (solid line) are shown in Fig. 2.2(c). Comparing to the tissue concentration curve shown in Fig. 2.1, which is obtained from a normal voxel located in the contralateral hemisphere of the same patient, the tissue curve obtained from the ipsilateral hemisphere has a relatively small MR signal change and the first and sub-

[2]The DWI abnormalties can be visualized as regions with hyperintensities in a DWI image.

[3]An ipsilateral voxel means the voxel is located in the same hemisphere as the ischemic lesions. On the other hand, a contralateral voxel is located in the opposite hemisphere with respect to the ischemia lesions.

[4]The T_2 infarction may be visualized as regions with hyperintensities in a T_2 image.

sequent passages of the contrast agent are temporally overlapped. This resulted from the fact that for patients with cardiovascular and/or cerebrovascular diseases, vessel blockage may induce reduced blood perfusion, and hence resulting brain tissue damage. When cerebral hemodynamics is compromised such as cerebral ischemia, thus, the passage of only a small amount of contrast agent is allowed. A substantially broadened concentration curve is anticipated, leading to the first passage inevitably overlapping with recirculation. It is clear from Fig. 2.2(c) that under such condition, the currently available approaches are unlikely to offer a consistent means for discerning contributions of recirculation from the first passage.

Second, important physiological information may potentially be lost by imposing an analytic equation on all measured concentration time curves. An alternative method is, therefore, in order.

2.3 Simulation Studies

The ICA approach is only valid when the signal sources are independent of each other and at most one source is normally distributed. In the current study, ICA analysis on the basis of a standard Infomax algorithm was used, and this approach is effective only when the distributions of these source signals are super-Gaussian. Simulation studies were conducted to examine the statistical dependence between the first passage and the recirculation, as well as the distributions of concentration curves to determine the validity of the proposed ICA approach in discerning the first passage from recirculation. The kurtosis of each first-pass and the associated recirculation component was calculated to determine whether the sources are super- or sub-Gaussian. In addition, the sum of squared error (SSE) between the estimated and the putative first passage were studied to determine the effectiveness of this approach. Detailed discussion of these simulation studies is given below.

2.3.1 Statistical Independence

One of the main assumptions for the proposed ICA is that the first passage and recirculation are statistically independent. It is therefore, imperative to determine the validity of such assumption. A 5×5 ROI (marked by the black square) was chosen from

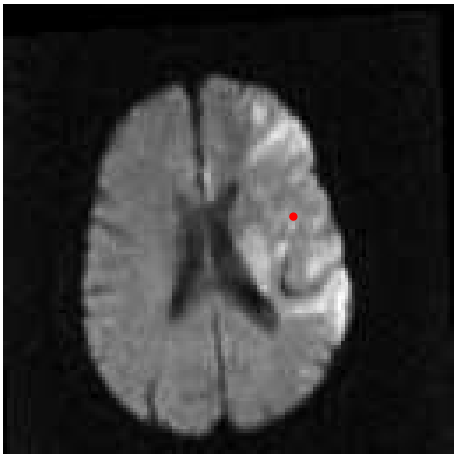

(a) Acute DWI image

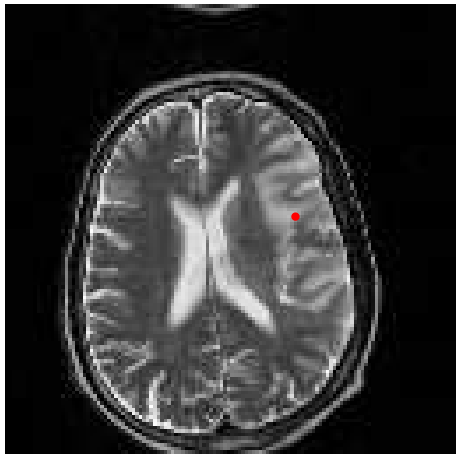

(b) Follow-up T_2 image

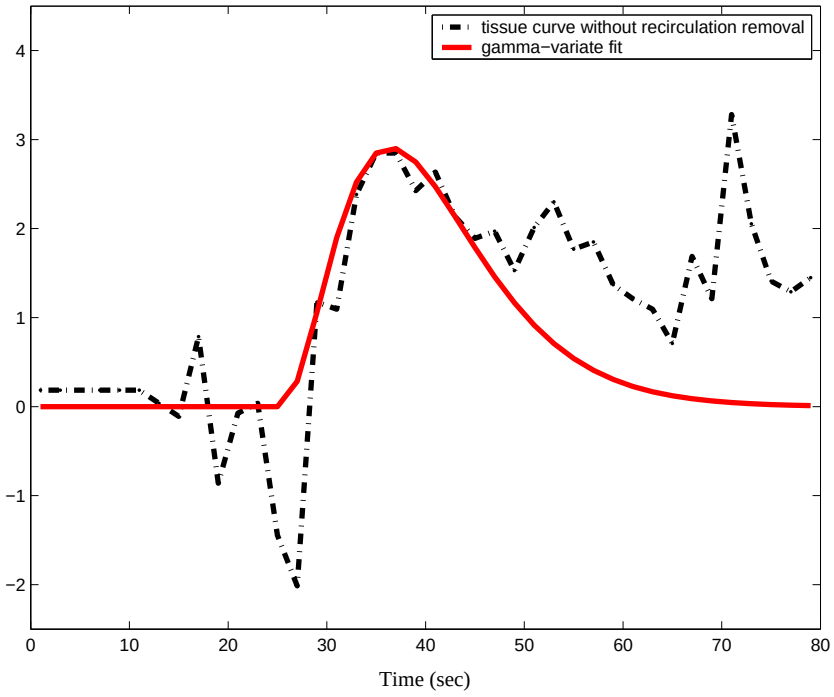

(c) Removing recirculation using gamma-variate fitting

Figure 2.2: Recirculation removal using gamma-variate fitting for an acute stroke patient

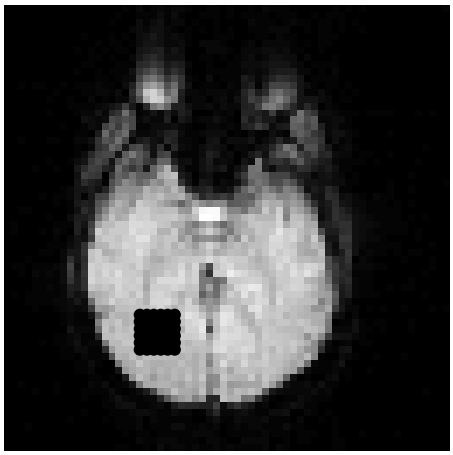

Figure 2.3: The anatomical image of a normal volunteer

one slice of a normal subject as shown in Fig.2.3. A cut-off time was manually determined on the basis of the operator's subjective judgment for each of the 25 concentration time courses within the ROI in order to best separate the putative first passage and recirculation as demonstrated in Fig.2.4. Subsequently, to simulate different degrees of overlap and to increase the ambiguity between the first passage and recirculation, the maximum concentration of the operator-defined recirculation was first scaled to approximately half maximum of the corresponding operator-defined first-pass and was then artificially left shifted in time with respect to the first passage ranging from 1.5 sec to 10.5 sec with an increment of 1.5 sec. For example, Fig.2.5 shows the resulting averaged composite concentration curve of the first-pass and the left shifted (7.5 sec) and scaled operator-defined recirculation within the ROI. Finally, a Spearman rank coefficient test was employed to determine the degree of statistical independence between the first-pass and recirculation.

Spearman Rank Correlation Test

Spearman rank correlation test is one of the widely used non-parametric methods to determine the correlation between two random variables $X = (x_1, x_2, \cdots, x_N)^T$ and $Y = (y_1, y_2, \cdots, y_N)^T$ especially when none of them is Gaussian distributed.

Let random variables $X_r = (x_{r1}, x_{r2}, \cdots, x_{rN})^T$ and $Y_r = (y_{r1}, y_{r2}, \cdots, y_{rN})^T$ be the rank random variables corresponding to X and Y respectively. That is, X_{ri} is the rank

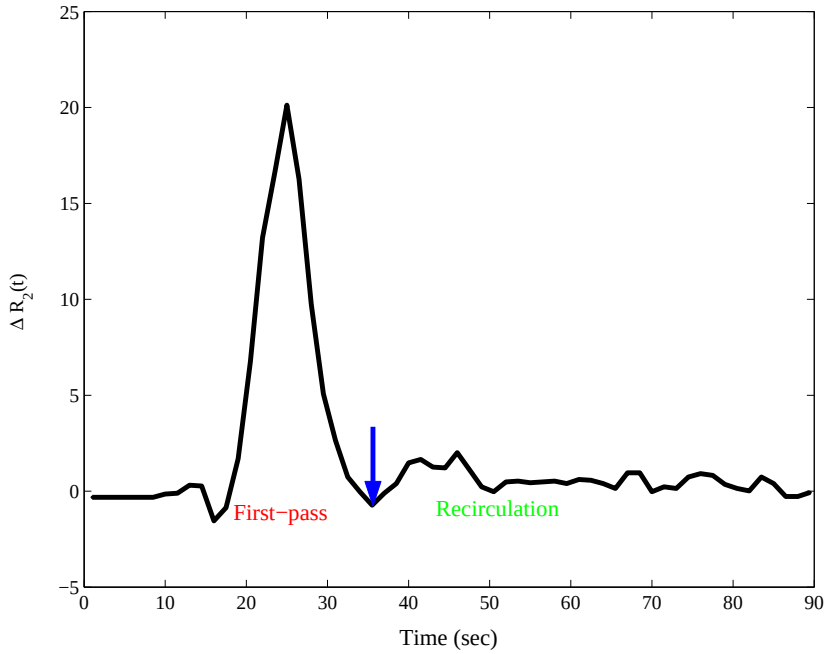

Figure 2.4: An operator-defined cut-off time (marked by the arrow) was selected to best separate the putative first-pass and recirculation.

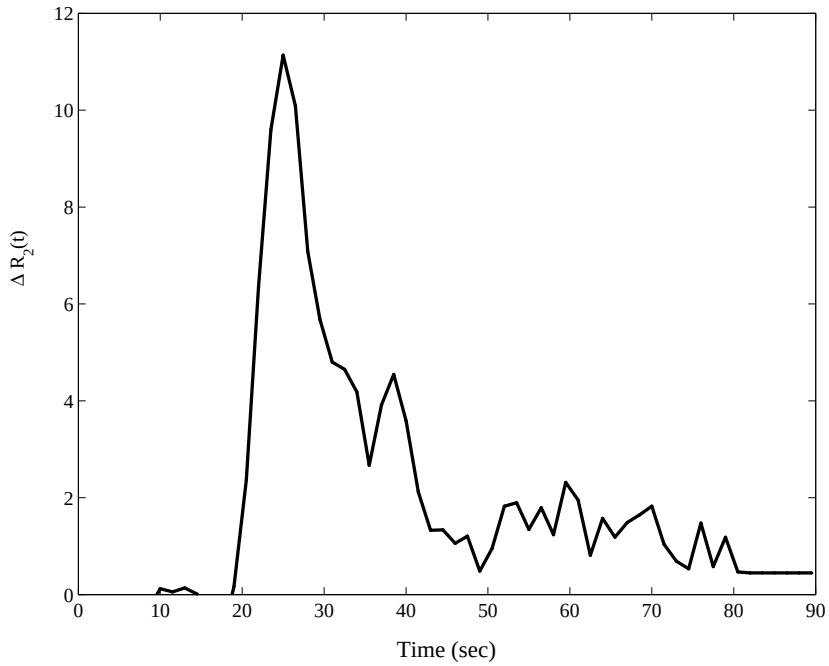

Figure 2.5: Averaged simulated composite time course when the operator-defined recirculation time courses were left shift in time by 7.5 sec

of X_i among all the other values that X takes in the sample, and similarly Y_{ri} is the rank of Y_i among all the other values that Y takes in the sample. If some of the x_i's (or y_i's) have identical values, it is conventional to assign to all these "ties" the mean of the ranks that they would have had if their values had been slightly different. The rank variables X_r and Y_r are, thus, uniformly distributed on $[1, N]$. The Spearman rank correlation coefficient is defined as the linear correlation coefficient between X_r and Y_r as reflected by Eq.(2.3).

$$r_s = \frac{\sum_{i=1}^{N}(X_{ri} - \bar{X_r})(Y_{ri} - \bar{Y_r})}{\sqrt{\sum_{i=1}^{N}(X_{ri} - \bar{X_r})^2(Y_{ri} - \bar{Y_r})^2}} \tag{2.3}$$

Unlike the linear correlation coefficient (or the Pearson correlation coefficient) which is the best estimate of the correlation between X and Y when both of them are Gaussian distributed, the Spearman rank correlation coefficient does not depend on the original distributions of the random variables.

2.3.2 Effectiveness of the ICA Approach

Composite concentration curves with different degrees of overlap between the first-pass and recirculation were first obtained as aforementioned. Both the proposed ICA and the commonly employed gamma-variate fitting methods were employed to extract the first-pass from the composite concentration curves. Since the putative first-pass was available, the SSE between the estimated first-pass using either the proposed ICA approach or the gamma-variate fit and the putative first-pass was calculated to test the effectiveness of each method.

2.4 Independent Component Analysis

In the current study, Infomax [19], one of the most widely used ICA algorithms, was employed to reveal different temporal components in the concentration time curves. The temporal Infomax algorithm with a maximum likelihood formulation analysis (ICAML) was applied to concentration time curves within each 5×5 ROI throughout the entire brain parenchyma as

$$C_i(t_j) = \sum_{k=1}^{M} a_{ik} s_k(t_j) \quad (i = 1, \cdots, 25; j = 1, \cdots, N), \tag{2.4}$$

where $C_i(t_j)$ is the concentration time curve obtained at voxel i at time t_j, a_{ik} is the mixing coefficient, $s_k(t_j)$ is the k^{th} temporal independent component (IC) at t_j, N is the number of measurements (N=60 and either 40 or 50 respectively for normal volunteer and patient studies), and M is the number of sources.

Since the number of latent components, M, is unknown, the Bayesian Information Criterion (BIC) method [39, 40] was employed to estimate the number of sources.

In general, given an observed dataset C, the posterior probability of the model containing m sources is $P(m|C)$ $(m = 0, \cdots, K)$, where K is the number of observed random variables in the dataset. Assuming the model is defined in terms of a parameter vector θ, let $P(C|\theta, m)$ be the generative model density given by the observation. We then have,

$$P(C|m) = \int P(C, \theta|m) d\theta = \int P(C|\theta, m) P(\theta|m) d\theta. \tag{2.5}$$

In practice, it may be difficult to obtain an analytical form of the integral in Eq. (2.5). The Bayesian Information Criterion approximation may be used instead. Approximating the integral by a Gaussian in the vicinity of the maximum posterior parameter vector θ^* which maximizes the integrant, Eq. (2.5) becomes

$$P(C|m) \approx P(C|\theta^*, m) P(\theta^*, m) T^{-d/2}, \tag{2.6}$$

where d is the dimension of the parameter vector θ, and T is the number of training cases.

The posterior probability of the model containing m sources, $P(m|C)$, can thus be obtained using the Bayes Theorem by

$$P(m|C) = \frac{P(C|m)P(m)}{P(C)} \quad (m = 0, \cdots, K), \tag{2.7}$$

where $P(m)$ is the prior probability. Usually a uniform distribution over the set $\{0, \cdots, K\}$ is used if there is no prior belief.

By estimating the posterior probability of the model containing M components, the model order may be determined by $M = \underset{m \in [0,1,\cdots,K]}{\operatorname{argmax}} P(m|C)$ [5].

[5] Matlab code for BIC based ICAML analysis is available through the website [41].

2.5 Identification of Recirculation Components

In order to determine the potential components contributed by recirculation, the following procedures and criteria were employed. First, the relative energy of each IC, $P_k(k = 1, ..., M)$, was calculated as in Eq.(2.8).

$$P_k = \frac{\sum_{i=1}^{25} a_{ik}^2 \sum_{j=1}^{N} s_k^2(t_j)}{\sum_{k=1}^{M} \sum_{i=1}^{25} a_{ik}^2 \sum_{j=1}^{N} s_k^2(t_j)} \quad (k = 1, \cdots, M) \tag{2.8}$$

Second, the full-width-half-maximum (FWHM) of the major dip/peak of each component was obtained. Third, the TTA of the major dip/peak of each component was estimated as the time when the component reaches the half maximum. Fourth, the components with the earliest TTA were first excluded, and the mean TTA of the remaining components was used as a threshold such that any component with a TTA later than this threshold was determined to be a late arrival component. Fifth, the late arrival ICs with a relative energy less than 20% of the total energy and the largest FWHM, which also needs to be at least 10.5 sec for normal subjects and 14 sec for acute stroke patients, were considered as recirculation components. If no recirculation associated IC was found, M was increased and ICA analysis was repeated. Sixth, after determining the recirculation components, other late ICs with relative energy smaller than that of the recirculation components were considered as noise components. Finally, both recirculation and noise components were excluded, and concentration time courses were then reconstructed using the remaining ICs.

2.6 Relative Regional Cerebral Blood Volume Analysis

If recirculation components were not effectively removed from the first passage, rrCBV calculated as the area beneath each concentration time curve [5,6] may be overestimated. A ROI approach was employed to obtain quantitative measures of rrCBV to assess effectiveness of minimizing recirculation. In the normal subject group, mean rrCBV encompassing both hemispheres in one slice was determined for comparison. For acute stroke patients, on the other hand, two ROIs were defined to obtain estimates of rrCBV based on the 1 or 3-month follow-up T_2-weighted images with one ROI encompassing the T_2 lesion

and the other at a similar anatomical region in the contralateral hemisphere. In addition, normalized rrCBV maps were also generated, which is defined as the rrCBV differences between the gamma-variate fitting and the ICA approach and normalized to that obtained using gamma-variate fitting.

2.7 Statistical Analysis

Statistical analyses based on right-tailed paired t-test were employed to compare the performance of ICA and gamma-variate fitting using SSE in simulation studies and rrCBV in stroke patient studies. A P-value less than 0.05 was considered significantly different.

2.8 Results

The proposed methodology was tested using the DSC images acquired from three healthy volunteers (one male, two females, age 24-33) and five acute stroke patients (three males, two females, age 63-83).

The BIC procedure demonstrates that the number of independent components, M, varies at different anatomical locations and among different subjects. For example, Fig. 2.6 and Fig. 2.7 illustrate the optimum number of independent components estimated using BIC for an ipsilateral noninfarction ROI and an infarction ROI of an acute stroke patient respectively. BIC, nevertheless, reveals M ranging between 5 to 7 components. An M of five was therefore typically used in our study. In the event that none of the ICs fulfilled the criteria as a recirculation component, M was increased up to 7, and the entire process was repeated. This approach has proven to be robust in identifying the recirculation components.

2.8.1 Simulation Studies

The Spearman rank correlation test for the composite concentration curves with different degrees of overlaps between the first-pass and recirculation is summarized in Table 2.1. Although the Spearman rank correlation coefficients are nonzero, they are relatively

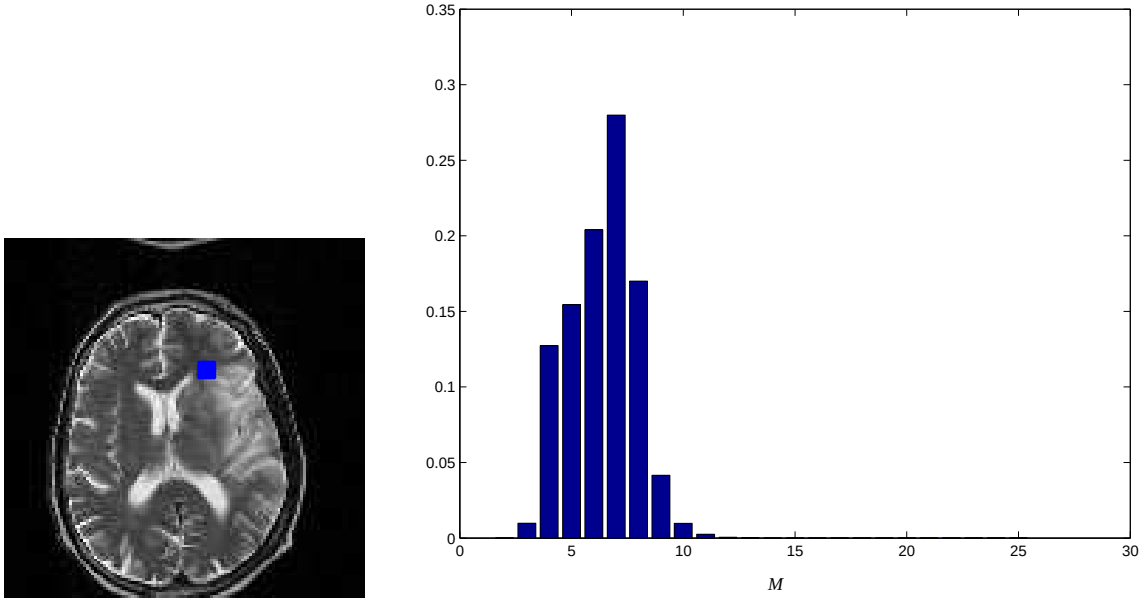

(a) An ipsilateral noninfarct ROI (b) The optimum number of independent components is $M = 7$.

Figure 2.6: Component probability distribution calculated using BIC for an ipsilateral noninfarction ROI from the data acquired on an acute stroke patient

Artificial shift in time (in time)	1.5	3.0	4.5	6.0	7.5	9.0	10.5
Averaged Spearman rank coefficient	-0.078	-0.059	-0.048	-0.019	0.003	0.02	0.046
Averaged P-value	0.551	0.668	0.604	0.565	0.495	0.371	0.346

Table 2.1: Analysis for determining statistical independence between first-pass and recirculation

small (ranges from -0.078 to 0.046). Moreover, even when a substantial overlap is present (time shift = 10.5 sec), an average Spearman rank correlation coefficient of 0.046 ($P > 0.3$) is obtained, suggesting that the first-pass and recirculation remain statistically independent.

Standard Infomax algorithm may fail when the sources are sub-Gaussian. The averaged kurtosis for the putative first-pass and recirculation of the concentration curves within the predefined 5×5 ROI in Fig. 2.3 are 6.68 and 0.42, respectively. Since both the first-pass and recirculation have positive kurtosis, they are likely to be super-Gaussian and thus the standard Infomax algorithm may be used.

The ability of the proposed ICA approach to separate the first-pass from the re-

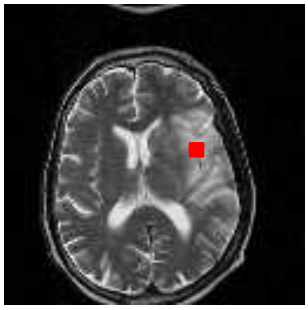

(a) An infarction ROI

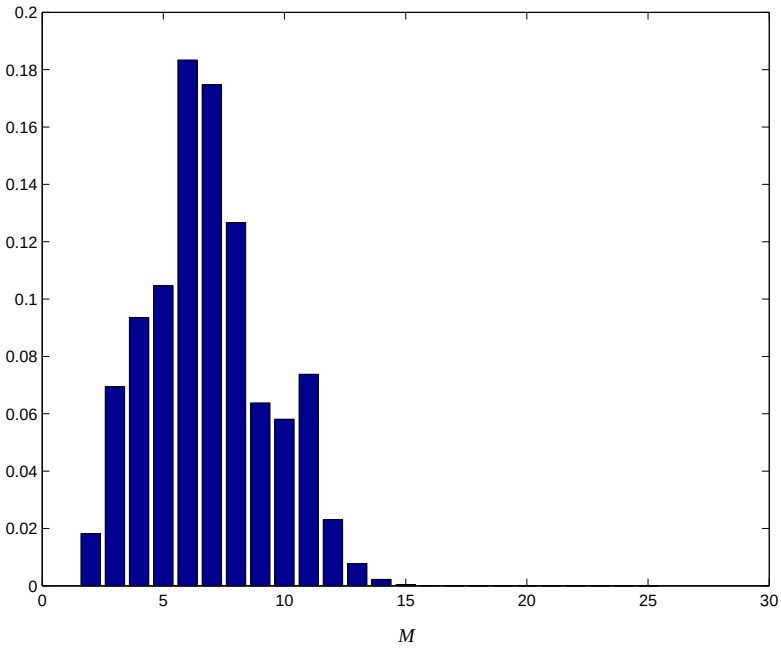

(b) The optimum number of independent components is $M = 6$.

Figure 2.7: Component probability distribution calculated using BIC for an infarction ROI from the data acquired on the same patient shown in Fig. 2.6

circulation is shown in Fig.2.8. The same 5×5 ROI displayed in Fig.2.3 was chosen to illustrate the proposed approach. Although all of the procedures outlined in the Simulation Studies section were carried out on a voxel-by-voxel basis, the averaged concentration curve of the 25 voxels within the ROI is shown for better illustration (this convention is used hereafter unless otherwise mentioned). ICA analysis and gamma-variate fitting were performed for the composite concentration time courses shown in Fig.2.5 when the operator-defined recirculation was scaled and artificially left shifted in time for 7.5 sec with respect to the corresponding first-pass. Seven ICs are observed in Fig.2.8(a) and IC4, IC5, IC6 and IC7 (marked by the arrows) are identified as recirculation or noise components (relative energies of 4.34%, 4.18%, 3.52% and 1.66%, respectively). The averaged operator-defined first-pass (solid line), the averaged gamma-variate fit (dash-dotted line), and the averaged ICA reconstructed time-course (dashed line) after removing IC4, IC5, IC6 and IC7 are shown in Fig.2.8(b). The gamma-variate fit substantially over-estimates the first-pass, whereas the ICA approach provides more similar results to the operator-defined first-pass.

The same 5×5 ROI as shown in Fig.2.3 was used to quantitatively compare the effectiveness of the proposed ICA methodology and that of the gamma-variate fit for minimizing recirculation. The averaged SSEs between the estimated first-pass using either the proposed ICA approach or the gamma-variate fit and the operator-defined first-pass with different time shifts (1.5 sec to 10.5 sec), are shown in Fig.2.9. Statistical analysis reveals that the SSE deviations from the operator-defined first-passages for fitting are significantly larger than those for ICA ($P = 0.03$). Although both the proposed ICA approach and the gamma-variate fit perform equally well for time shift less than 4.5 seconds, a marked increase in SSE deviation is observed when the time shift is greater than 4.5 seconds using the gamma-variate fitting approach, whereas a rather small SSE is observed using the ICA approach for all of the evaluated time shifts. These findings suggest that the proposed ICA approach is more effective than the gamma-variate fitting approach in separating first-pass from recirculation, even when a substantial overlap between the first-pass and the recirculation is present.

2.8.2 Normal Volunteer Study

A representative image from a normal volunteer is shown in Fig.2.10(a). The square indicates the 5×5 ROI used to illustrate the effectiveness of the proposed ICA approach. Five ICs are observed in Fig.2.10(b) where IC4 and IC5 (marked by the arrows) are identified as the recirculation component (relative energy of 1.09%) and the noise component (relative energy of 0.33%), respectively. A direct comparison between the original concentration curve (dash-dotted line) and those obtained using gamma-variate fitting (solid line) or ICA (dashed line) is shown in Fig.2.10(c).

A direct comparison of the normalized rrCBV maps for all three volunteers is shown in Fig.2.11. Consistent with that observed in Fig.2.10, similar rrCBV values are obtained using gamma-variate fitting and ICA. This suggests that both approaches are equally effective in minimizing the effects of recirculation for normal volunteers.

2.8.3 Acute Stroke Patient Study

A representative T_2-weighted image from an acute stroke patient is shown in Fig.2.12, delineating the presence and extent of an ischemic lesion. In order to illustrate

the efficacy of the proposed ICA method in minimizing recirculation in different regions with respect to the ischemic lesion, three ROIs were chosen: one at the center of the ischemic core (red square), one at the peri-infarct area (blue square), and the other in the contralateral hemisphere (yellow square). For the ROI in the contralateral hemisphere, five ICs are observed (Fig.2.13(a)) and IC5 (marked by the arrow) is identified as the recirculation component (relative energy of 1.57%). For the ROI containing primarily the core, six ICs are observed (Fig.2.14(a)) and IC4 (marked by the arrow) is identified as the recirculation component (relative energy of 9.33%). In addition, for the peri-infarct region, five ICs are observed (Fig.2.15(a)) and IC4 (marked by the arrow) is identified as the recirculation component (relative energy of 8.25%). A direct comparison of the unprocessed concentration time curves (dash-dotted line), gamma-variate fitting-processed (solid line), and ICA-processed (dashed line) to minimize recirculation effects for the three ROIs, is shown in Fig.2.13(b), Fig.2.14(b), and Fig.2.15(b), respectively. Consistent with the normal volunteer studies, similar results are obtained via the gamma-variate fitting and ICA approach in the contralateral hemisphere, whereas the ICA approach is consistently more effective than the gamma-variate fitting in minimizing the contribution of recirculation in both the core and peri-infarct regions.

Fig.2.16 shows the normalized rrCBV maps for all five acute stroke patients (left to right). For each patient, a follow-up T_2-weighted image (top), delineating the presence and extent of the final ischemic lesions, and the corresponding normalized rrCBV map (bottom) are shown. A marked overestimation of rrCBV using the gamma-variate fitting is observed in regions of ischemic lesions (red areas). Interestingly, some regions exhibit a higher rrCBV using the ICA approach when compared with that obtained using the gamma-variate fits (blue areas).

2.8.4 ROI Analysis

Results obtained from the ROI analysis are summarized in Fig.2.17 for both the normal volunteer and the acute stroke patient studies. For the normal subject study, the rrCBV values obtained using the gamma-variate fitting are comparable to those obtained using the ICA method. In contrast, for acute stroke patient study, even in the contralateral hemisphere, the normalized percent rrCBV difference between gamma-variate fits and ICA results ranges from -0.54% to 14.1%, not to mention that in the final T_2 lesion regions, which

ranges from 16.1% up to 21.1%. Statistical analysis reveals that the averaged percent rrCBV differences ($19 \pm 2\%$) between the gamma-variate fitting and ICA methodology in T_2 lesion tissue are significantly larger ($P < 0.005$) than those obtained from the contralateral tissue ($8 \pm 5\%$).

2.9 Discussion

A new methodology to minimize recirculation effects for DSC PWI is proposed. It entails the decomposition of concentration time courses into temporally and statistically independent sources, and the identification and subsequent minimization of the recirculation components. This methodology was tested on simulated concentration time curves, normal volunteers and acute stroke patients with various degrees of ischemic abnormalities.

Temporal ICA assumes temporal and statistical independence among the components. Although it is possible to consider that the first-pass and recirculation concentration time courses are temporally shifted from one another and conceivably highly correlated, by and large, the paths through which the contrast agent reaches the brain can be different. From a physiological point of view, one could consider that the main path through which the contrast agent reaches the brain during the first-pass, is from the injection site, the heart, and the carotid/vertebral arteries. In contrast, the sources/paths during recirculation are far more complicated. They include, from a very simplistic view, the originally observed contrast agent during the first-pass but travelling through the intracranial venous system, back to the heart and then again reaching the brain as well as the contrast agent which was not observed during the first-pass because it initially travelled through the peripheral circulation. The first-pass and recirculation are, therefore, not very likely to be highly dependent.

Using the Spearman rank correlation test and the composite concentration curves with a varying degree of overlap, a rather small Spearman rank correlation coefficient was obtained, independent of the degrees of overlaps between the first-pass and recirculation. This finding suggests that the first-pass and recirculation are weakly dependent. In addition, both the first-pass and recirculation have positive kurtosis, indicating they are super-Gaussian. Together, these findings indicate that the ICA analysis on the basis of the standard Infomax algorithm should be appropriate to discern the first-pass from recirculation. These

findings are further augmented by simulation results. Composite concentration curves with various degrees of overlaps between the first-pass and recirculation were simulated. When the first-pass and the recirculation are well separated, both gamma-variate fitting and ICA methods successfully remove recirculation effects. In contrast, as the overlap between the first-pass and recirculation increases, the gamma-variate fitting approach fails to minimize the effects of recirculation (Fig.2.8 and Fig.2.9). This finding is not surprising since the success of the gamma-variate fitting approach greatly hinges on the temporal separation between the first-pass and recirculation. As a result, when a substantial overlap between the first-pass and recirculation is present, ICA outperforms the gamma-variate fitting method. These simulation results suggest that the proposed ICA technique is capable of minimizing recirculation even with a broadened curve, underscoring the potential significance and impacts on results obtained from patients with compromised brain perfusion such as cerebral ischemia.

Consistent with the simulation results, both gamma-variate fitting and ICA perform quite well in minimizing the effects of recirculation in normal volunteers as well as the putative normal brain regions of acute stroke patients. However, in regions of ischemic lesions a substantially higher rrCBV is observed using the gamma-variate fitting approach when compared with that obtained using ICA. This finding is likely to be explained by the inability of the gamma-variate fitting approach to minimize effects of recirculation when the concentration curves are broadened. The use of the proposed ICA method should therefore improve, in principle, the quantification of cerebral hemodynamics such as CBV, CBF and MTT especially in case of ischemic stroke.

While the proposed ICA approach is highly effective in minimizing effects of recirculation, it should be noted that the reconstructed concentration time courses after removing the recirculation and noise components are slightly different from the operator-defined first passages (Fig.2.8(b)). Several potential factors could account for the observed discrepancies, including the choice of the number of ICs, the size of ROI for ICA analysis, and the criteria for identifying recirculation components. We will separately discuss these potential factors below. First, with the Bayesian Information Criterion model selection, it suggests that an optimal number of ICs between 5 and 7 can account for most of the temporal MR signal variation. In this study, the number of ICs was, therefore, predefined to be within 5 to 7 components. One of the potential pitfalls associated with this predefined number of ICs, is that if the number of ICs is too large, ICA analysis can split the same information

into several temporal components. As a result, it may lead to sub-optimal temporal decomposition of the concentration time curves. In addition, when using a large number of components, it will become more difficult to interpret each independent component in terms of its underlying physiological origin(s). Although, choosing 5 to 7 components appears to be robust in minimizing the recirculation effects in the current study, contributions coming from the first-pass and the recirculation may not be fully separated in some cases. Some contributions of the first-pass may also be removed (Fig.2.8(b)), and/or the recirculation effects may not be completely removed (blue regions in the bottom row of Fig.2.16). Nevertheless, in contrast to the large errors observed with gamma-variate fitting for broadened curves, the minor ICA imperfection should not greatly affect the estimation of cerebral hemodynamics.

Second, temporal ICA was applied for each 5×5 ROI throughout the brain parenchyma. Such choice of the ROI size represents a balance between signal-to-noise ratio (SNR) and ICA performance. With a smaller ROI size, SNR may not be acceptable to depict components statistically different from noise. On the other hand, if the spatial coverage of the ROI is large, many independent components may result, making it difficult to discern first-pass and recirculation components and leading to inaccurate estimation of cerebral hemodynamics. Furthermore, especially in the acute stroke patient study, a large ROI may encompass both normal and diseased tissues. A ROI of 5×5 was, therefore, chosen in our study to provide an acceptable SNR while minimizing partial volume effects especially for acute stroke patient studies. Nevertheless, this choice of the size of ROI could also contribute to the observed discrepancies between the putative and the ICA estimated first-pass. The evaluation of an optimal choice of all ROI size is, unfortunately, beyond the scope of our current studies.

Third, a set of criteria was established to identify recirculation components, including the requirement that the component has: a relative energy lower than 20% of the total, a late arrival time, and the largest FWHM, which also needs to be greater than 10.5 sec for normal subjects and 14 sec for acute stroke patients. While these criteria may not be the most optimal set of parameters to identify recirculation components, and hence may contribute to the observed discrepancies between the estimated and putative first-pass, both simulation and normal volunteer studies have demonstrated that these criteria are highly effective in minimizing recirculation while preserving the general shape of the first-pass. More importantly, despite extensive overlap between first-pass and recirculation using the

simulated concentration curves, the SSEs remain small using the proposed ICA. This finding has major ramifications for acute stroke studies where a substantial overlap between the first-pass and recirculation is commonly observed, particularly in regions of ischemia. As shown in Fig.2.14(b) and Fig.2.15(b), the proposed ICA approach outperforms the commonly employed gamma-variate fitting approach within both the core as well as per-infarct regions. One may, nevertheless, question the choice of the late arrival time as one of the criteria for identifying recirculation components in stroke patients since even the first-pass will be delayed due to compromised cerebral hemodynamics. This ambiguity should, however, not affect our ability to determine the components arising from recirculation. This is due to the fact that the comparison of the arrival time is carried out for each 5×5 ROI separately. When the ROI is located within or close to the lesion, all of the components will be delayed; the first-pass component should, however, remain the first to arrive in the ROI and thus the criteria should remain effective. One potential problem is in regions that have very low or no flow, leading to minimal MR signal changes. In this case, ICA may not be able to identify any statistically significant sources. This is, however, a common problem associated with the DSC approach, and the proposed approach is unlikely to overcome this difficulty.

Finally, it may be possible to further improve the proposed ICA method. For example, constrained principal component analysis (PCA) [42], probabilistic PCA [43, 44], expectation maximization ICA (EM-ICA) [45] or independent factor analysis [46] may also be used for blind source separation. Although the probabilistic PCA model uses a more sophisticated noise model compared to the standard PCA, it still assumes Gaussian source distributions. While ICA searches for independent projections of the data, in EM-ICA, both the demixing matrix and source distributions are also estimated [45]. In addition, independent factor analysis is an extension of EM-ICA where more general Gaussian noise is modelled [46]. While the methodology proposed herein, may not be the only alternative, its direct comparison with other methods strays us away from our goal of providing a more viable alternative to a well accepted solution, and is hence beyond the scope of this study.

In conclusion, a temporal ICA approach to minimize the recirculation effects in DSC perfusion was described and compared to one of the most commonly used approaches, gamma-variate fitting. While a comparison of the two approaches suggests that they are equally effective in normal subject study, ICA is superior to gamma-variate fitting in minimizing recirculation and in preserving the characteristics of the first-pass of contrast agent

in both simulated and acute stroke patient studies when the concentration time courses are broadened. This finding indicates that the effects of recirculation can be minimized by the ICA approach even in the presence of a substantial overlap between the first-pass and recirculation. The proposed approach is, therefore, believed to provide a more accurate estimation of CBV, CBF and MTT in patients with cerebrovascular diseases.

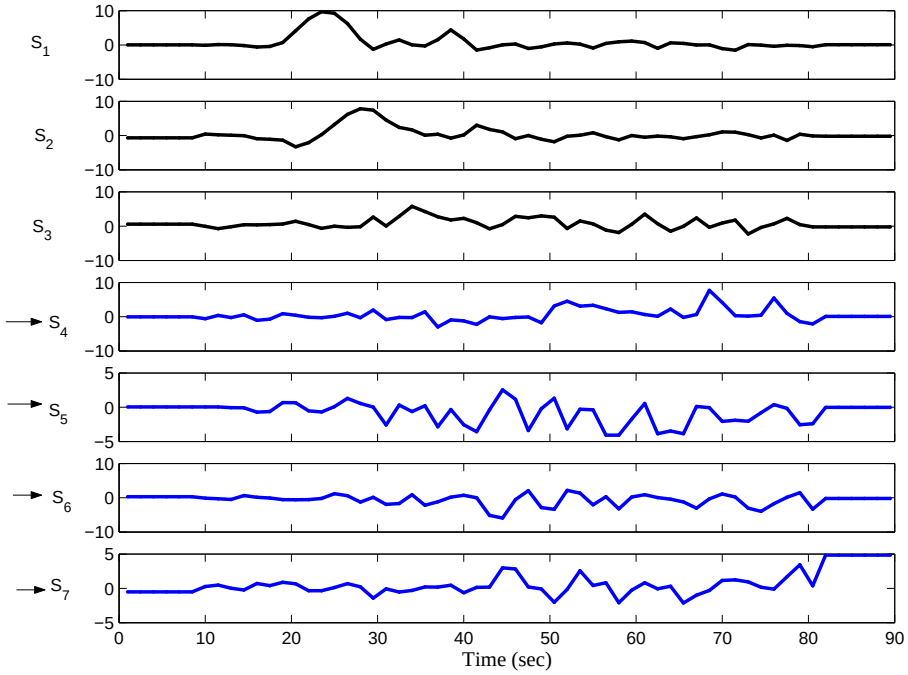

(a) With the simulated composite concentration curves shown in Fig.2.5, seven ICs are obtained with IC4, IC5, IC6 and IC7 identified as recirculation and noise components.

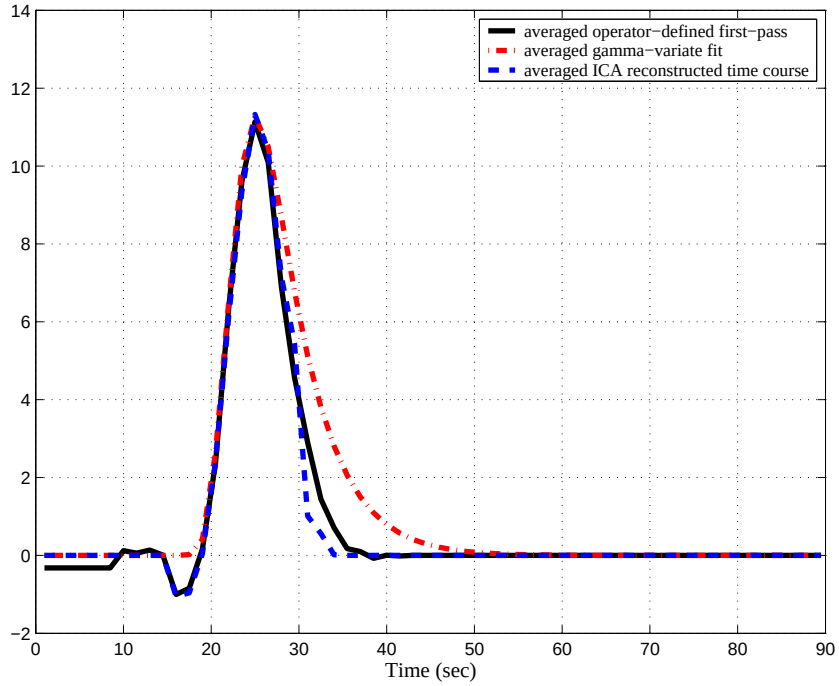

(b) Averaged concentration curves with and without recirculation removal

Figure 2.8: An ICA analysis example using simulated broadened curves when the operator-defined recirculation time courses were left shift in time by 7.5 sec is illustrated. The same 5×5 ROI displayed in Fig.2.3 was used for obtaining concentration time courses.

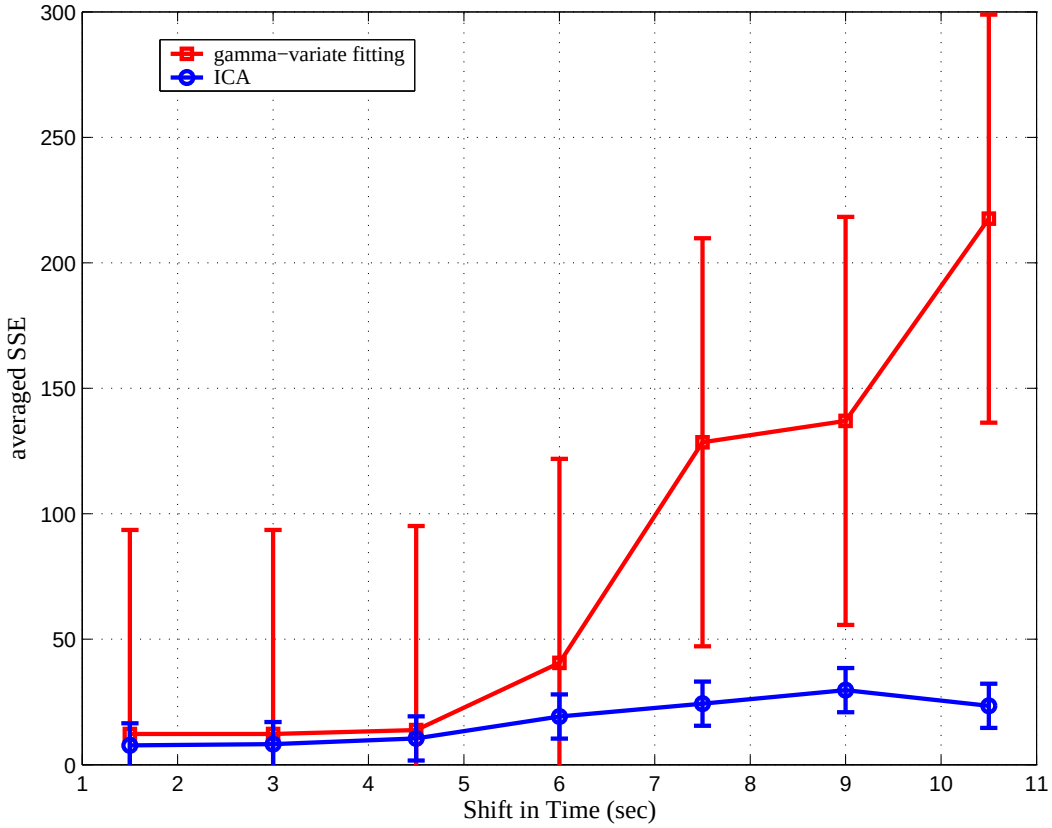

Figure 2.9: Average SSEs between the operator-defined first-pass and that obtained using either the gamma-variate fitting or ICA are shown. The error bars represent 1 standard deviation.

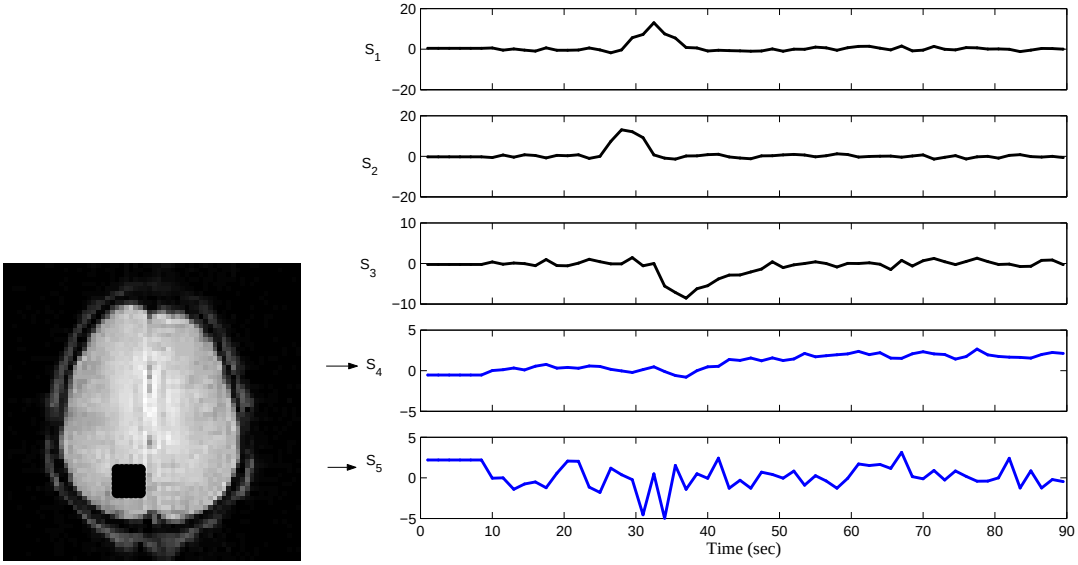

(a) The anatomical image (b) IC4 and IC5 are identified as the recirculation and noise components respectively

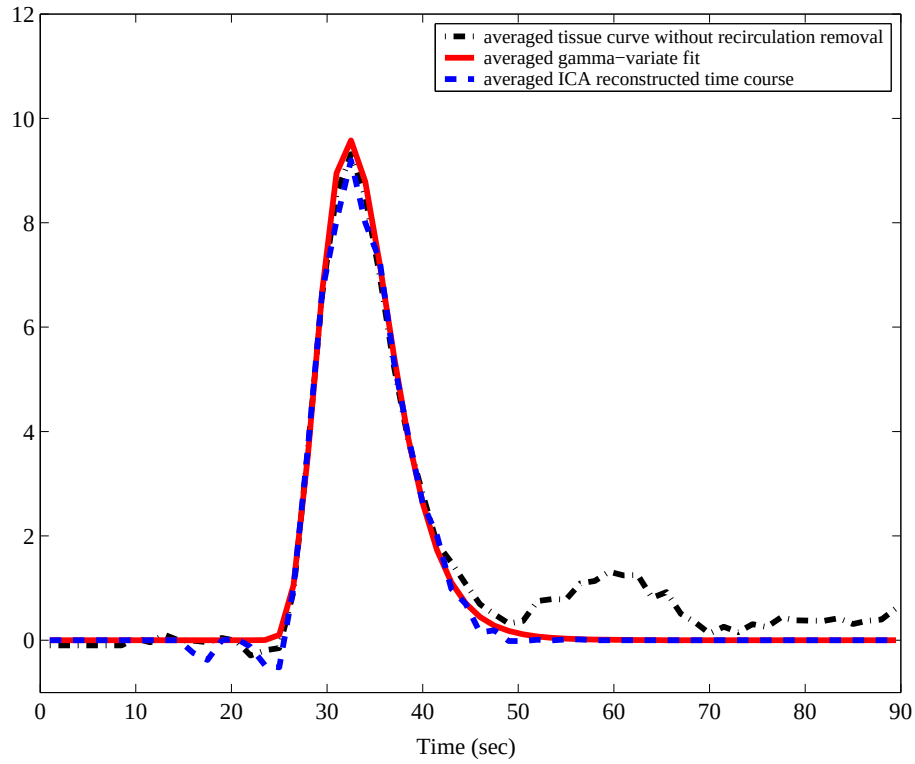

(c) Averaged concentration curves without and with recirculation removal

Figure 2.10: An ICA analysis example for a 5×5 ROI (marked by the black square) chosen from a normal volunteer

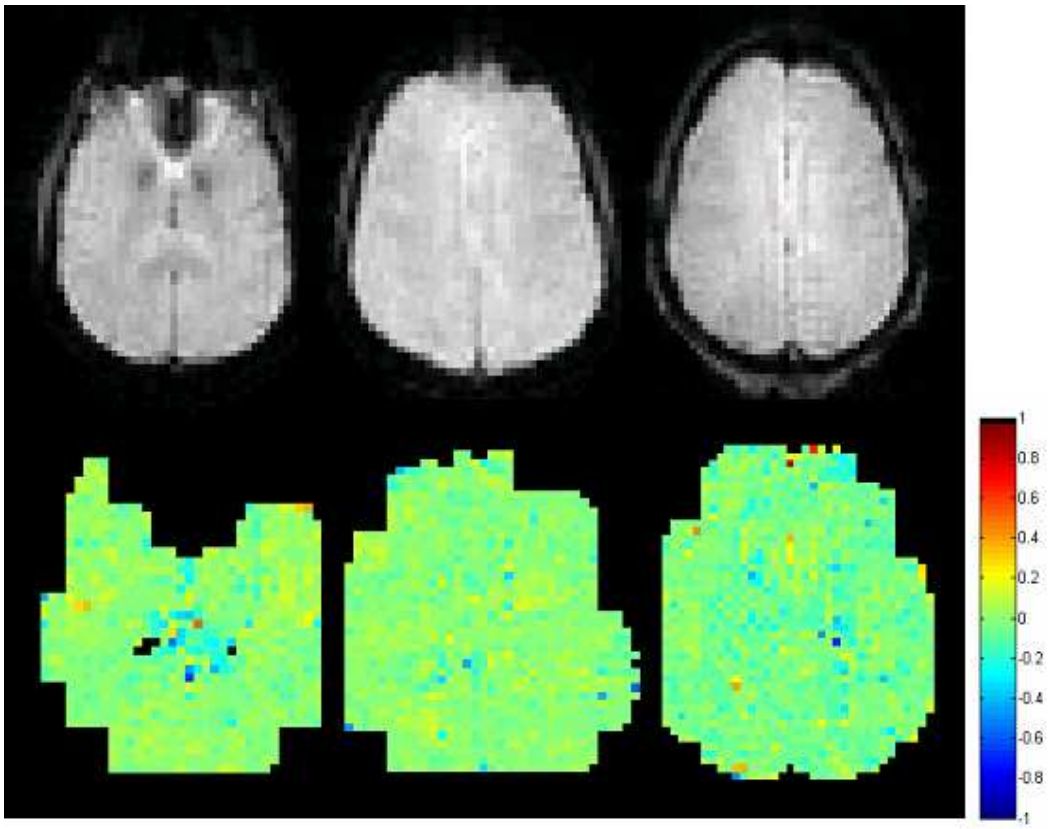

Figure 2.11: Representative normalized rrCBV maps (bottom row) obtained as the rrCBV differences between the gamma-variate fitting and the ICA approach and normalized to that obtained using the gamma-variate fitting are displayed for all three normal subjects (from left to right). The anatomical images are displayed in top row. The color scale depicts the normalized rrCBV differences.

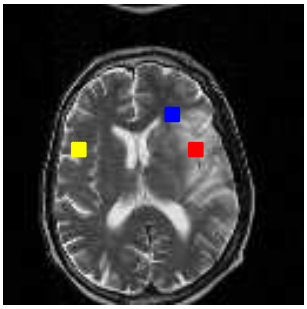

Figure 2.12: A representative T_2- weighted image obtained at the chronic phase depicts the extent of the final lesion. Three 5×5 ROIs (one yellow ROI in the contralateral hemisphere, one red ROI within the ischemic core and one blue ROI at the peri-infarct area) were chosen to demonstrate the performance of the proposed ICA approach.

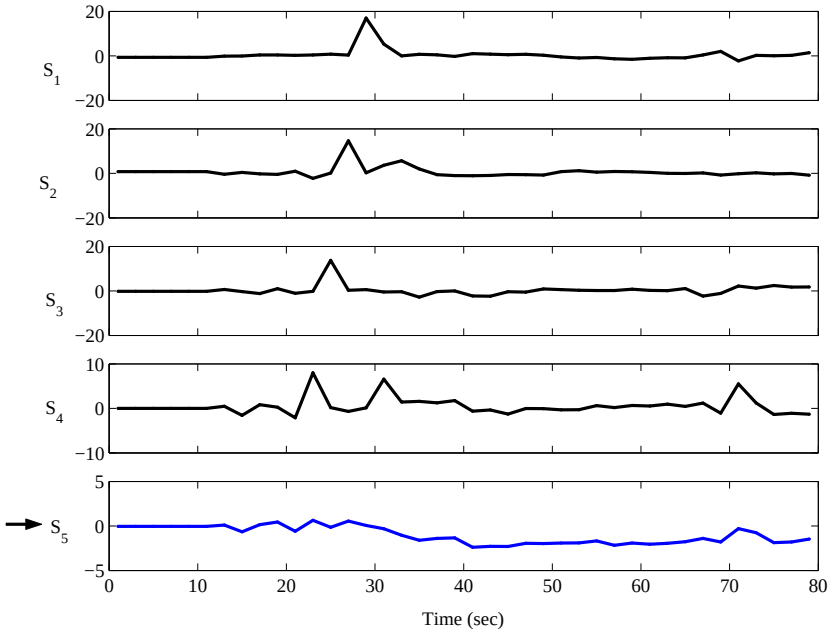

(a) IC5 is identified as the recirculation component.

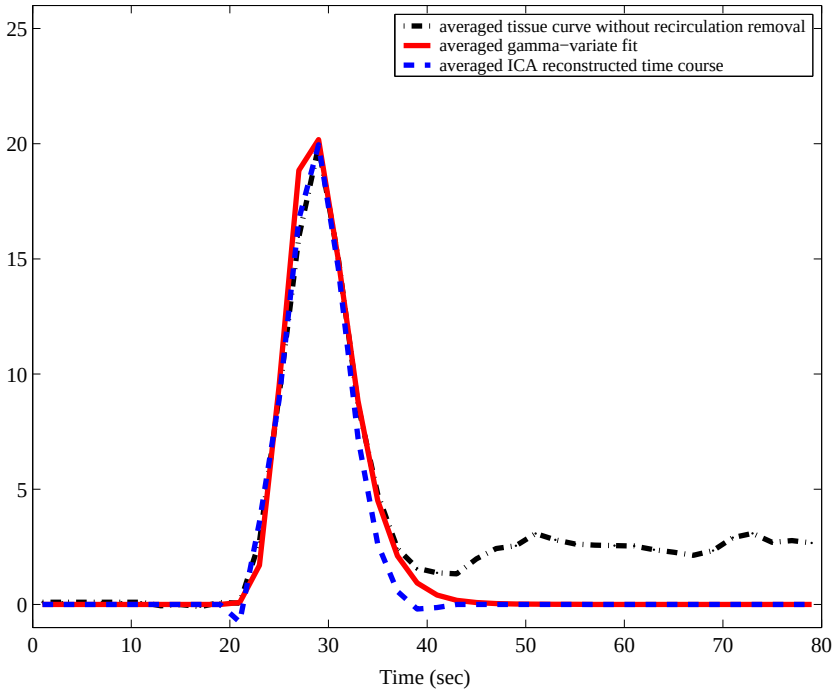

(b) Averaged concentration curves without and with recirculation removal

Figure 2.13: ICA analysis of a contralateral normal ROI chosen from the same patient shown in Fig. 2.12

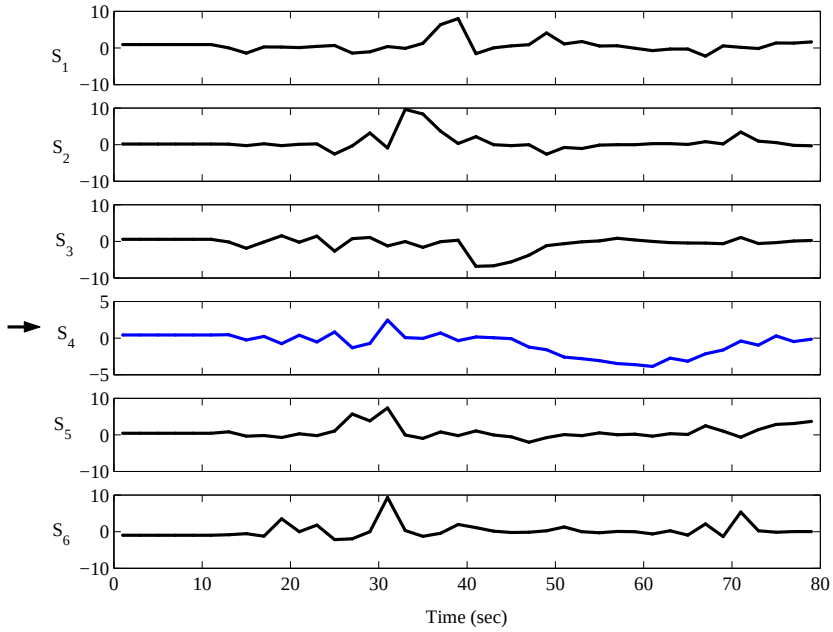

(a) IC4 is identified as the recirculation component.

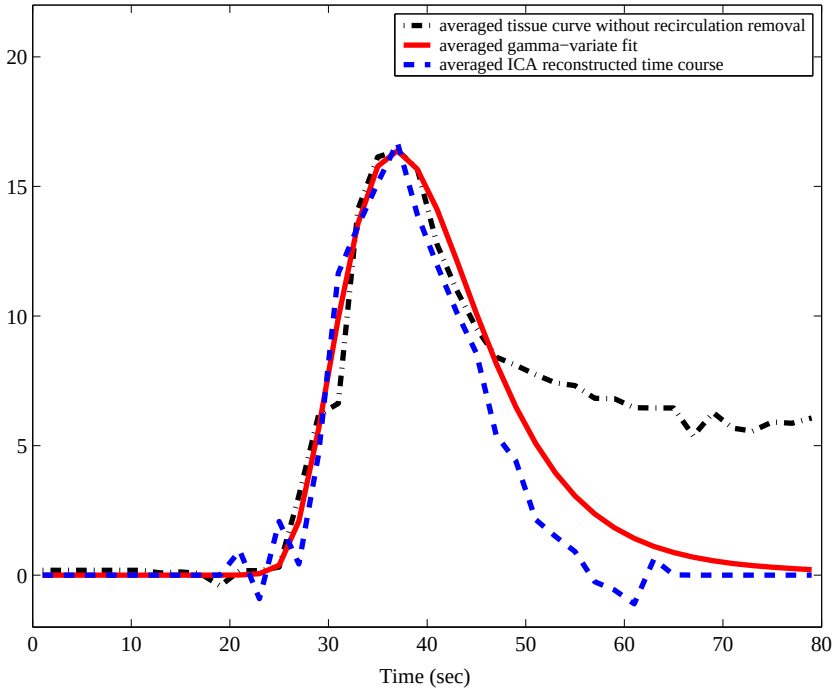

(b) Averaged concentration curves without and with recirculation removal

Figure 2.14: ICA analysis of an ischemic core ROI chosen from the same patient shown in Fig. 2.12

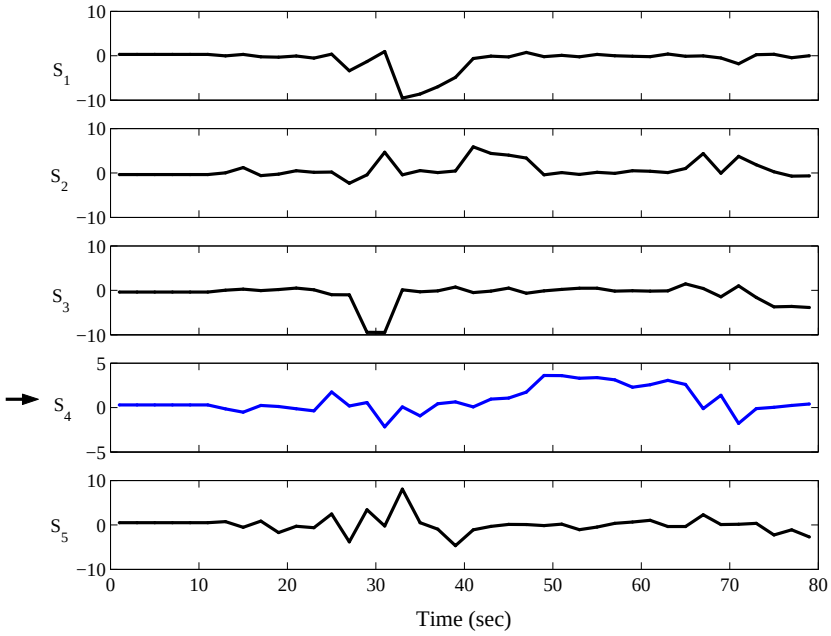

(a) IC4 is identified as the recirculation component.

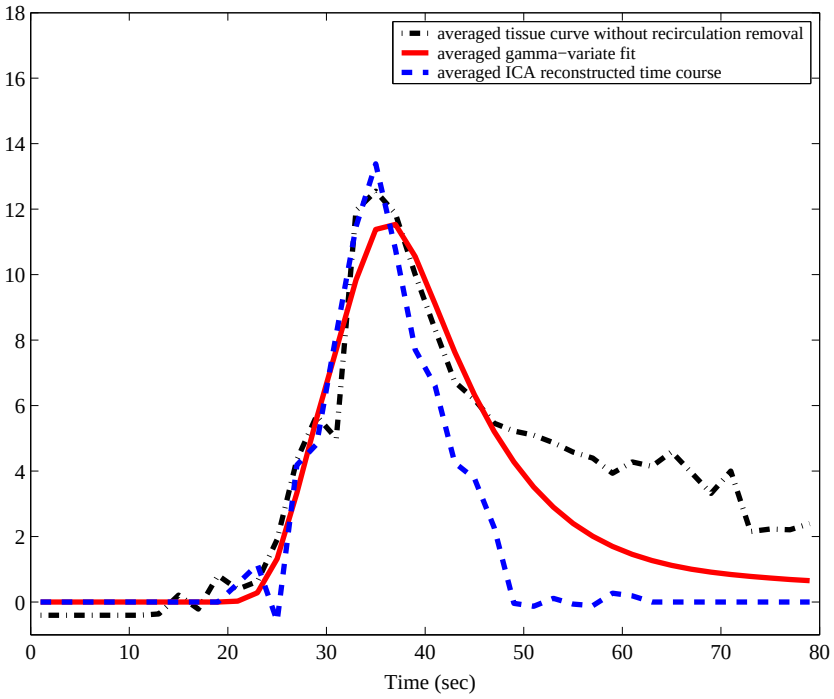

(b) Averaged concentration curves without and with recirculation removal

Figure 2.15: ICA analysis of a peri-infarct area ROI chosen from the same patient shown in Fig. 2.12

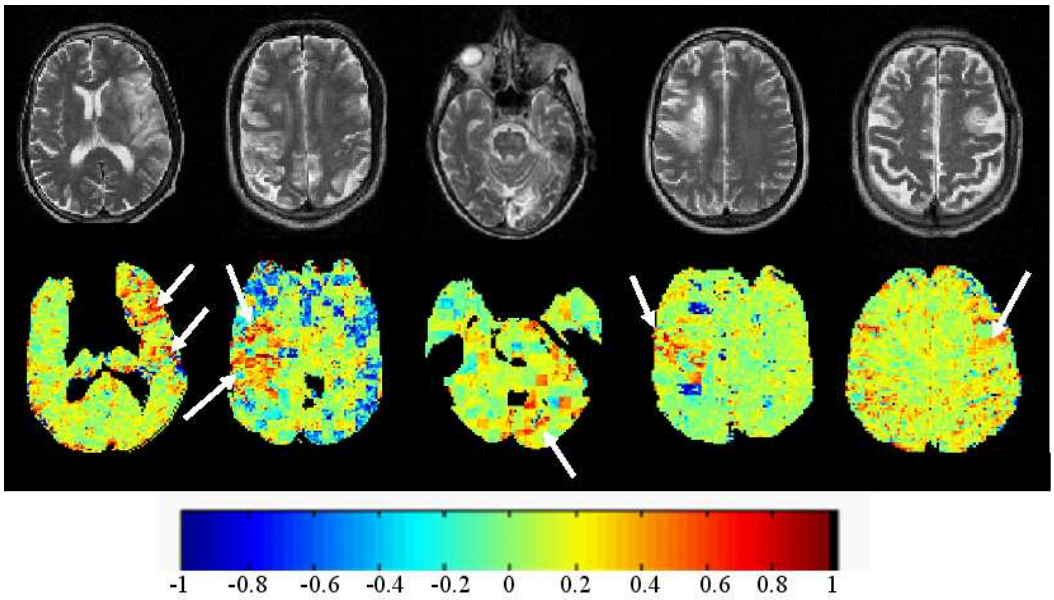

Figure 2.16: The rrCBV comparisons for all of the stroke patients (left to right) are shown. A representative T_2-weighted image acquired at the chronic phase of each patient is shown (top). The rrCBV differences between gamma-variate fitting and ICA were normalized by the gamma-variate fitted rrCBV (bottom). The color bars indicate the normalized rrCBV differences.

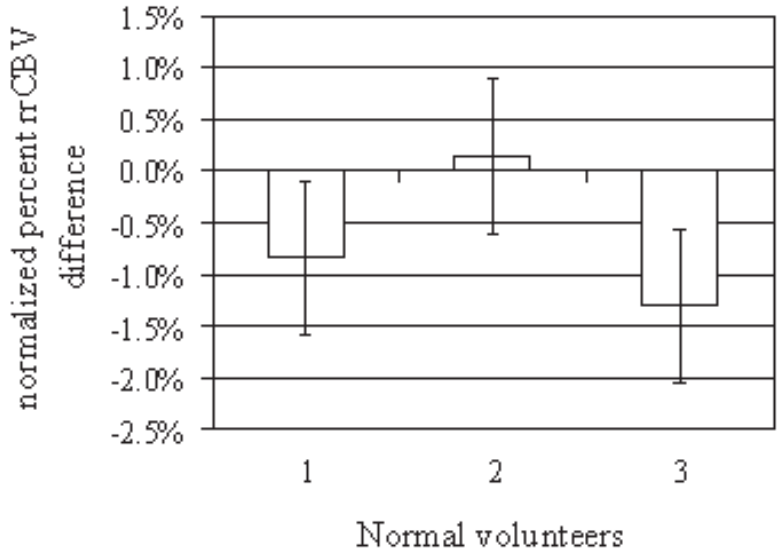

(a) For normal volunteers

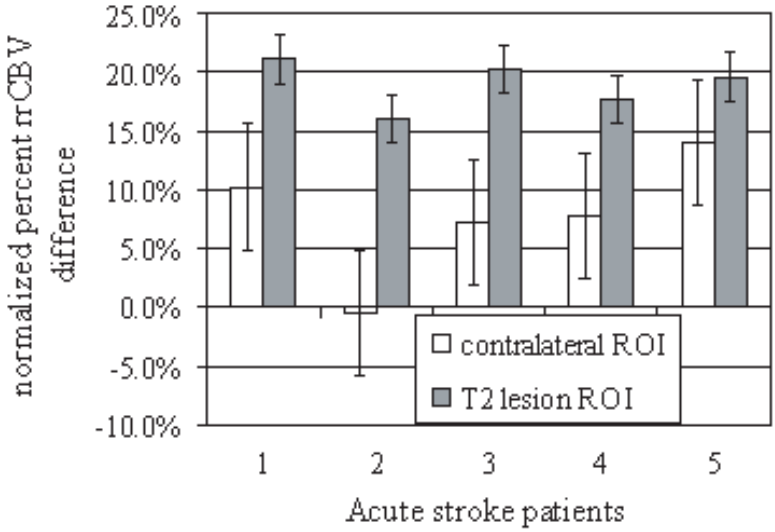

(b) For acute stroke patients

Figure 2.17: The rrCBV differences between the gamma-variate fitting and the proposed ICA and normalized to that obtained using the gamma-variate fitting are shown. The error bars represent 1 standard deviation.

Chapter 3

Bolus Delay Correction on Flow Estimation in DSC MR Imaging

3.1 Introduction

Dynamic susceptibility contrast MR approaches can provide hemodynamic parameters indicating important physiological information about perfusion status of brain tissues. By injecting a bolus of paramagnetic contrast agent intravenously, rapid measurement of MR signal change can be obtained during its passage through the brain tissues. The MR signal change can be converted to a concentration temporal signal, $C(t)$, which contains important physiological information.

Assuming an ideal instantaneous unit bolus injection at time $t = 0$, the contrast agent enters the ROI as some function of time, $C_a(t)$, which is AIF. The residue function $R(t)$ is defined as the fraction of injected contrast agent entering the ROI at $t = 0$ which is still present in the ROI at time t. The tissue concentration curve, $C(t)$, is then given by Eq. (3.1) [2], where F is the averaged cerebral blood flow, $C_a(t)$ is the AIF and $R(t)$ is the tissue residue function, and "$*$" denotes linear convolution.

$$C(t) = F \cdot \int_0^t C_a(t)R(t-\tau)\,d\tau = FC_a(t) * R(t) \tag{3.1}$$

From Eq. (3.1), average perfusion may be ideally estimated by deconvolving the temporal tissue curve, $C(t)$, using an AIF measured from a localized small artery in the vicinity of the ROI for each voxel. In practice, however, a voxel may contain more than one tissue type depending on the size of the voxel. And this phenomenon is called partial volume effect. For example, if a small voxel contains only blood vessel or tissue, then as shown in Fig. 3.1, a larger voxel may contain a combination of the two. The MR signal measured from that larger voxel, hence, is the superposition of the weighted MR signals arising from the blood vessel and tissue. As a result, it is a big challenge to measure local AIFs from small vessels in practice [47, 48]. Instead, a global AIF (GAIF) measured in large vessels such as a major cerebral artery is normally used to estimate CBF for all brain parenchyma voxels. This global AIF may thus, lead or lag some tissue curves, which inevitably induces delays between the global AIF and tissue concentration curves. For example, Fig. 3.2(a) shows a PWI image acquired from an acute stroke patient. The global AIF is measured by averaging MR signal changes from the MCA delineated by the green boundary in the hemisphere labelled "R" , while a region of interest is chosen in the hemisphere labelled "L" . As demonstrated from Fig. 3.2(b), significant delays between the global AIF and tissue curves are present since the global AIF may not be the exact input to the region of interest. In cerebral ischemic regions, inaccurate CBF estimation may, therefore, be induced using SVD [49–54] since the bolus delay introduced during its passage from the site of AIF measurement to the ROI is interpreted as occurring within the ROI by the perfusion quantification model.

Approaches to potentially correct this bolus delay have, therefore, been proposed by several investigators. Wu *et al.* propose to utilize a SVD approach but with a block-circulant matrix which is less sensitive to bolus delay and thereby minimizes the inaccuracy [55]. In addition, Calamante *et al.* propose to utilize a spatial ICA to construct the local arterial input functions (LAIF) [33]. Although positive results have been reported using both approaches, cSVD is less accurate in determining low CBF values compared to standard SVD at SNR=20, while the local AIFs constructed using the spatial components may not completely preserve the original shape of the AIF due to, potentially, the imperfection of ICA.

In this study, we investigate an alterative approach where temporal ICA is used to determine the correct bolus arrival time for each 5×5 ROI. Subsequently, the arrival time of the global AIF obtained from the MR signal changes at the contralateral MCA is modified

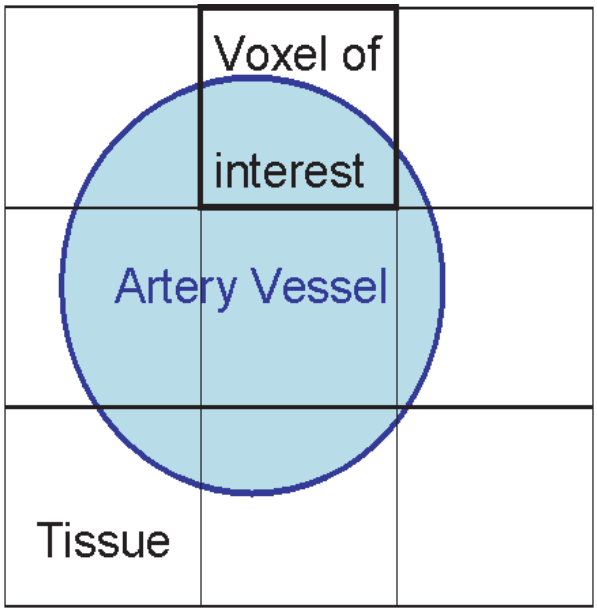

Figure 3.1: A voxel contains both vessel and tissue due to partial volume effects.

in accordance with the bolus arrival time. Finally, the time shifted global AIF is used as the local AIF for each 5×5 region throughout the entire brain parenchyma. By doing so, correct bolus arrival time can be obtained and moreover, the general shape of AIF can be preserved. The defined local AIF can thus be used to obtain estimates of CBF through standard SVD. Our results demonstrate that the global AIF and the local AIF methods are comparable for normal volunteers or acute stroke patients with small ischemic lesions where the bolus delay is expected to be insignificant. In addition, our proposed method yields acute PWI abnormality which is more consistent with the final infarction, particularly for acute stroke patients with large ischemic lesions.

3.2 Previous Work

3.2.1 Minimizing Bolus Delay using Circular SVD

Assuming $t_k = k\Delta t$ $(k = 0, \cdots, N-1)$, the N-point tissue concentration time signal expressed in Eq. (3.1) then may be rewritten in a discretized form as Eq. (3.2), which can be further written in a vector form as Eq. (3.3).

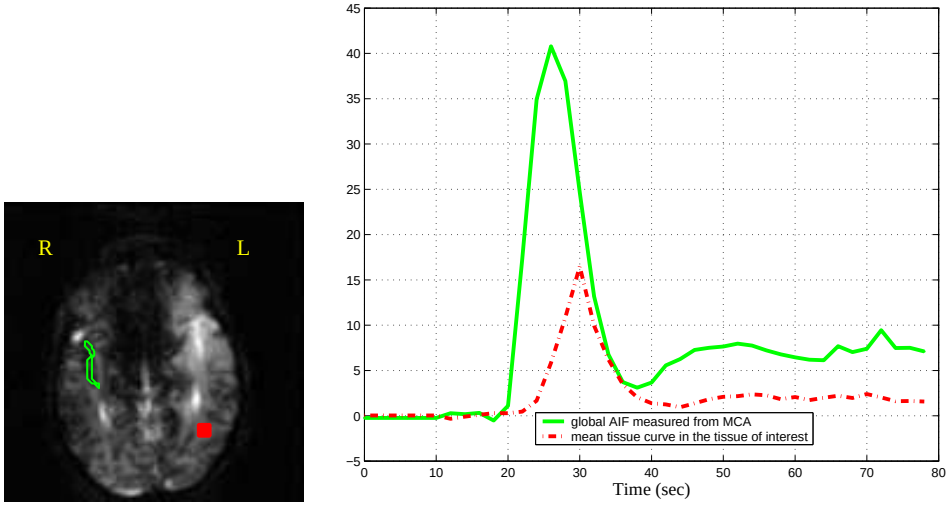

(a) Green: MCA, red: ROI (b) Delays between the AIF and tissue curves

Figure 3.2: Bolus delays

$$C(t_j) = F \cdot \Delta t \cdot \sum_{i=0}^{j} C_a(t_i) R(t_j - t_i) \tag{3.2}$$

$$\begin{pmatrix} C(t_0) \\ C(t_1) \\ \vdots \\ C(t_{N-1}) \end{pmatrix} = \Delta t \cdot \begin{pmatrix} C_a(t_0) & 0 & \cdots & 0 \\ C_a(t_1) & C_a(t_0) & \cdots & 0 \\ \vdots & \vdots & \vdots & \vdots \\ C_a(t_{N-1}) & C_a(t_{N-2}) & \cdots & C_a(t_0) \end{pmatrix} \cdot \begin{pmatrix} R(t_0) \\ R(t_1) \\ \vdots \\ R(t_{N-1}) \end{pmatrix} \cdot F \tag{3.3}$$

Eq. (3.3) may be written as Eq. (3.4) by defining $c = [C(t_0), C(t_1), \cdots, C(t_{N-1})]^T$, $b = F \cdot [R(t_0), R(t_1), \cdots, R(t_{N-1})]^T$ and

$$A = \Delta t \cdot \begin{pmatrix} C_a(t_0) & 0 & \cdots & 0 \\ C_a(t_1) & C_a(t_0) & \cdots & 0 \\ \vdots & \vdots & \vdots & \vdots \\ C_a(t_{N-1}) & C_a(t_{N-2}) & \cdots & C_a(t_0) \end{pmatrix},$$

$$c = A \cdot b. \tag{3.4}$$

We can form a matrix $A = (a_{ij})_{N\times N}$ with elements given by Eq. (3.5) to prefilter the AIF in the aim of reducing noise contributions and compensating for discretization errors [2].

$$a_{ij} = \begin{cases} \Delta t \cdot \frac{C_a(t_{i-j-1})+4C_a(t_{i-j})+C_a(t_{i-j+1})}{6} & 0 \le j \le i \\ 0 & \text{otherwise} \end{cases} \tag{3.5}$$

The singular value decomposition of A is then given by Eq. (3.6),

$$A_{N\times N} = USV^T, \tag{3.6}$$

where U and V are $N \times N$ orthogonal matrices, i.e. $UU^T = U^TU = VV^T = V^TV = I_{N\times N}$. The matrix $S = diag(S_{11}, S_{22}, \cdots, S_{NN})$ is a nonnegative diagonal matrix and S_{ii} $(i = 1, \cdots, N)$ are the singular values. In our analysis, the SVD threshold was chosen to be 20%, i.e. only those singular values that are larger than 20% of the highest singular value were selected. The larger threshold is, the more the decomposition is immune to noise at a cost of larger quantification bias.

Define $W = S^{-1}$. From Eq. (3.4) and Eq. (3.6), we get $A^{-1} = VWU^T$ and $\hat{b} = A^{-1}c = VWU^Tc$. From Eq. (3.1), the deconvolution of the tissue curve and the AIF should be $F \cdot R(t)$. However, based on the definition of the residual function, assuming an ideal instantaneous unit bolus injection at t_0, the injected tracer entering the ROI at t_0 is still present in the ROI at time t_0, i.e. $R(t_0) \approx 1$. The maximum of the deconvolved function should, therefore, be the estimate of CBF which often does not occur at the zero time point due to tracer arrival delay as reflected by

$$\hat{F} = max(\hat{b}). \tag{3.7}$$

Notice that Eq. (3.3) presumes causality, i.e., the tissue concentration temporal curve cannot arrive earlier than the AIF. However, since the global AIF may not be the exact input to the tissue of interest, in the presence of ischemic abnormalities, the AIF may lag the tissue curve by a time delay τ especially when it is measured from a highly diseased vessel. If causality is assumed, the true residual function therefore cannot be properly estimated by SVD. However, circular convolution and linear convolution are equivalent by zero-padding the N-point time series $C_a(t)$ and $C(t)$ to length $2N$. By replacing matrix A with a block-circulant matrix, D, whose elements are given by Eq. (3.8), one can therefore use singular

value decomposition deconvolution but with a block-circulant matrix to improve the flow estimation.

$$d_{ij} = \begin{cases} a_{ij} & j \leq i \\ a_{2N+i-j,0} & \text{otherwise} \end{cases} \tag{3.8}$$

Comparing to standard SVD, better CBF estimation can be obtained by cSVD when the AIF lags the tissue curves (for example, if the AIF is selected from a highly diseased vessel) since causality assumption is not required. However, if we always select the AIF from the MCA in the contralateral hemisphere, it is not common that the AIF will lag the tissue curves. Moreover, assuming no delay between the AIF and tissue curves, the performance of standard SVD and cSVD in flow estimation are comparable. In addition, when the AIF leads the tissue curves, SVD performs comparably to cSVD at high SNR, while cSVD is less accurate in determining low flow values compared to SVD at SNR=20.

Although cSVD is less sensitive to delay, other alternative approaches yielding better flow estimation especially when the AIF leads the tissue curves should, thus, be of great interest.

3.2.2 Constructing Local AIF using Spatial ICA

Based on the assumption that the tissue concentration time curves throughout the whole brain parenchyma can be separated into spatially segregated and statistically independent components such as vascular, tissue and artifact components, Calamante *et al.* proposed to use spatial independent component analysis to decompose the concentration time curves into different spatial independent components throughout the entire brain parenchyma [33].

The optimal number of independent components, M, is estimated according to the Bayesian Information Criterion. The tissue curves are then decomposed into M independent sources. Local arterial sources are subsequently identified on the basis of both the spatial mappings and of the temporal characteristics of the components. A local AIF dataset is then constructed using arterial sources, and voxel-by-voxel perfusion is finally estimated by deconvolving the tissue concentration curves with the constructed local AIFs using standard SVD [33].

While this method shows improved CBF estimation, due to the imperfection of

ICA, the shape of the independent component may not be reliable. For example, when the number of sources is too large, the same information can be decomposed into multiple components such that the energy distribution of components is changed. Using the independent component directly to define the local AIF hence may not be adequate to preserve the general shape of AIF.

3.3 Bolus Delay Correction using Temporal ICA

3.3.1 Determining Bolus Arrival Time using Temporal ICA

The voxel-by-voxel MR susceptibility signal change was converted to a tissue concentration temporal signal first. A global AIF, $C_{ga}(t)$, was then measured from signal changes at the MCA in the contralateral hemisphere. Subsequently, recirculation was removed by a gamma-variate fit of the global AIF. The TTP was estimated as the AIF reaches its maximum. In addition, as demonstrated in Fig. 3.3, the TTA of the global AIF, TTA_g, was estimated as the time point before the TTP when the instant concentration is closest to the half maximum of the time curve.

Subsequently, based on the assumption that the temporal tissue concentration curves within each 5×5 ROI are mixtures of temporally and statistically independent sources such as arterial, venous, tissue, recirculation and noise contributions, Infomax [19], one of the most widely used ICA algorithms, was employed to reveal different temporal components. The temporal Infomax algorithm with a maximum likelihood formulation analysis (ICAML) was applied to concentration time curves within each 5×5 ROI throughout the entire brain parenchyma. The ROI size was chosen to be 5×5 in our study to provide an acceptable SNR while minimizing the partial volume effects especially for acute stroke patient studies. Using Bayesian information criterion, our results reveal that choosing between 5 to 7 sources can account for most of the signal variation. The number of independent components, M, was thus set to 5 first. The TTA of each component was estimated similarly as shown in Fig. 3.3 and the components were ranked by relative energy in descending order. Then both recirculation and noise components were excluded. If no recirculation associated IC was found, M was increased up to 7 and ICA analysis was repeated. Finally, concentration time curves were reconstructed using remaining components. At the same

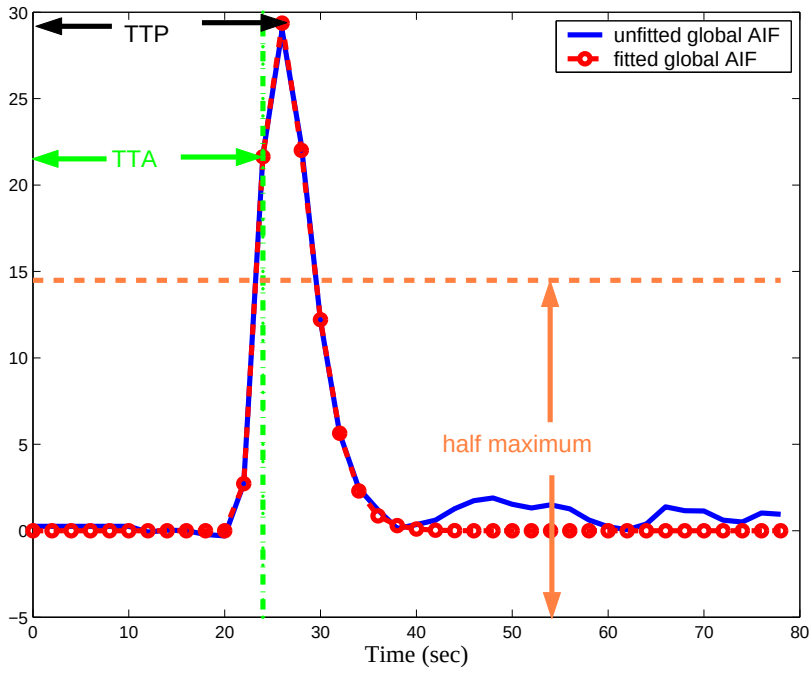

Figure 3.3: TTA and TTP estimation for the global AIF

time, the bolus arrival time within the 5×5 ROI, TTA_b, was estimated as the earliest TTA of the remaining independent components.

Since the global AIF was measured from the signal changes at the contralateral MCA, it is not common that the global AIF will lag the tissue curves. We may hence assume the global AIF always leads the tissue curves without introducing significant CBF quantification error. It has been shown that when the delay between the AIF and tissue curve is large (for example, when the tissue curve is measured from an infarction ROI with significantly delayed perfusion and the AIF is selected from the contralateral MCA), CBF may be underestimated and MTT may be overestimated thus yielding region with hypoperfusion inconsistent with the follow-up infarction [51]. As a result, we want to shift the global AIF properly to minimize the delay when the estimated bolus arrival time is later than the TTA of the global AIF in any 5×5 ROI (i.e. $TTA_b > TTA_g$). In contrast, when the estimated bolus arrival time, TTA_b, is earlier than TTA_g, or there is no time shift between the bolus and the global AIF, we may just keep the global AIF. In conclusion, a local AIF can be defined for each 5×5 ROI as shown in Fig 3.4.

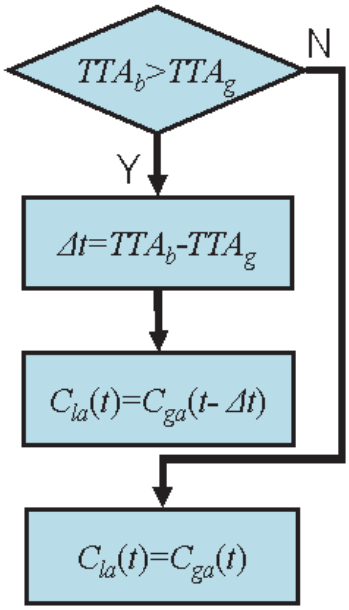

Figure 3.4: Define a local AIF for each 5×5 ROI

Fig. 3.5 shows three representative examples when delay among the tissue curve, the global AIF and the local AIF exists within a 5×5 ROI. When a significant delay between the global AIF and tissue curve occurs, (see, for example scenario (a)), the defined local AIF should be able to minimize the bolus delay and hence reduce the CBF quantification error effectively. In addition, if due to ICA imperfection, the estimated bolus even arrives earlier than the global AIF (see, for example, scenario (b)), by using the global AIF as the local AIF for the ROI, at least no more CBF error would be introduced. In contrast, the defined local AIF may lag the tissue curve sometimes (see, for example, scenario (c)), which may introduce CBF quantification errors. However, by decomposing the tissue curves into several temporal components, the bolus arrival time is estimated from the earliest TTA among all remaining components upon excluding the recirculation and noise sources. As a result, the bolus should arrive earlier than tissue curves. And scenario (c), thus, may not be common in practice. The proposed method should remain a promising alternative approach to minimize CBF quantification errors particularly when the global AIF significantly leads tissue curves.

A representative example from an acute stroke patient is shown in Figures 3.6 and 3.7 to demonstrate the efficacy of temporal ICA to determine local AIFs. An acute

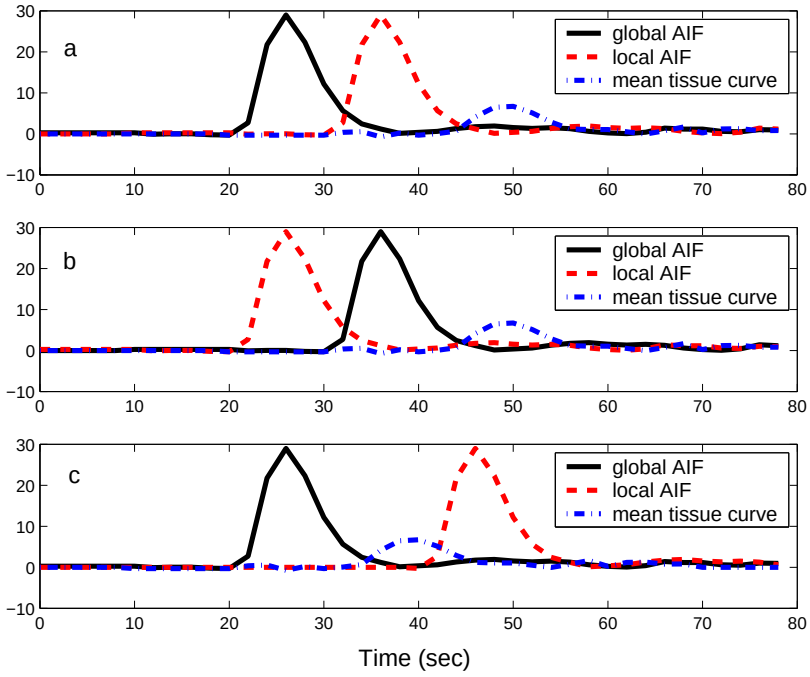

Figure 3.5: Representative examples when bolus delays among the tissue curve, the global AIF and the local AIF exist within any 5×5 ROI

DWI image and a one-month follow-up T_2 image are shown in Fig. 3.6(a) and Fig. 3.6(b) respectively, delineating the presence and extent of the ischemic lesions. Two 5×5 ROIs were chosen: the magenta one was selected from the infarction region, while the green one was chosen from the contralateral hemisphere with respect to the lesion. Five ICs sorted by relative energy in decreasing order are observed for the contralateral ROI as shown in Fig. 3.7(a). The recirculation component, IC4, was first removed, and among all the remaining components with a relative energy larger than the noise power, IC5 (marked by the arrow) is identified as the one with the earliest TTA. Similarly, as illustrated in Fig. 3.7(b), five ICs are observed for the infarction ROI. And IC4 and IC5 are identified as the recirculation component and the one with the earliest TTA among all statistically significant remaining components respectively. The global AIF obtained from signal change at the contralateral MCA (blue solid line), the local AIFs defined for the contralateral ROI (red dash-dot line) and the infarction ROI (black dash line), the averaged tissue curve in the contralateral ROI (green circle line) and the averaged tissue curve in the infarction ROI (magenta plus line) are shown in Fig. 3.8. It is clear that the defined local AIFs effectively minimize the time

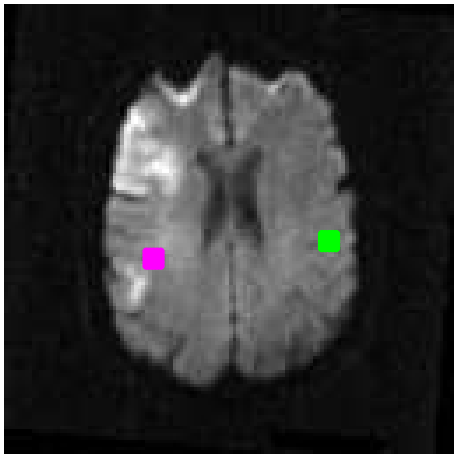

(a) Acute DWI image

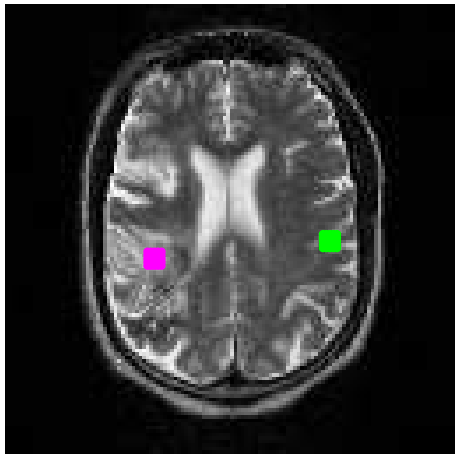

(b) Follow-up T_2-weighted image

Figure 3.6: Acute DWI and follow-up T_2-weighted images of an acute stroke patient

delays between the AIF and the tissue curves particularly in the infarction ROI.

3.3.2 Receiver Operating Characteristic Analysis

Within each 5×5 ROI, let $C(t)$ be the reconstructed voxel-by-voxel tissue curve after removing recirculation and noise components. The tissue curve is related to the local AIF, $C_{la}(t)$, by

$$C(t) = F \cdot \int_0^t C_{la}(t) R(t-\tau)\, d\tau. \tag{3.9}$$

By deconvolving $C(t)$ with either the global AIF or the local AIFs using standard SVD, voxel-by-voxel perfusion F_g and F_l were then estimated respectively. Subsequently, CBV and MTT were estimated using either the global AIF or the defined local AIFs by Eq. (3.10) and Eq. (3.11) respectively.

$$\begin{cases} CBV_g = \int C(t)dt / \int C_{ga}(t)dt, \\ MTT_g = CBV_g / F_g, \end{cases} \tag{3.10}$$

$$\begin{cases} CBV_l = \int C(t)dt / \int C_{la}(t)dt, \\ MTT_l = CBV_l / F_l. \end{cases} \tag{3.11}$$

Finally, to assess the effectiveness of our approach, percentage difference maps of CBF and MTT with the help of $C_{ga}(t)$ and $C_{la}(t)$ were computed by

$$\begin{cases} \Delta CBF = (F_g - F_l)/F_g, \\ \Delta MTT = (MTT_g - MTT_l)/MTT_g. \end{cases} \tag{3.12}$$

Tissue was classified as abnormal if the MTT values were greater than a specified cutoff number of standard deviation (SD) from the mean MTT measured in the contralateral hemisphere. The cutoff values ranged from -15 to 15 in 0.2 increments. By comparing the acute tissue outcome determined by the MTT maps with the final infarction demonstrated on 1-month or later follow-up T_2 image, performance evaluation measures were obtained for the two methods respectively. Let TP be the true positive (i.e. the number of voxels appearing abnormal on the acute MTT map that do infarct on the follow-up T_2 image), and FN be the false negative (i.e. the number of voxels appearing normal on the acute MTT map that actually infarct on the follow-up T_2 image). The true positive ratio (TPR), or the sensitivity, was determined by

$$TPR = sensitivity = \frac{TP}{TP + FN}. \tag{3.13}$$

Similarly, let TN be the true negative (i.e. the number of voxels appearing normal on the acute MTT map that do not infarct on the follow-up T_2 image), and FP be the false positive (i.e. the number of voxels appearing abnormal on the acute MTT map that do not infarct on the follow-up T_2 image). The specificity, or the true negative ratio, and the false positive ratio (FPR) were computed by

$$TNR = specificity = \frac{TN}{TN + FP}, FPR = 1 - TNR = \frac{FP}{TN + FP}. \tag{3.14}$$

Receiver operating characteristic (ROC) curve was then generated by plotting a curve between TPR against FPR. The area under the ROC curve (AUC) was used to assess the performance of the two methods using either the global AIF or the local AIFs.

3.4 Results

Images were acquired from three healthy volunteers (one male, two females, age 24-33) and five acute stroke patients (three males, two females, age 63-78). All selected acute stroke patients have different degrees of major MCA occlusion to obtain a homogenous patient population. Furthermore, all five patients have available 1-month or later follow-up T_2-weighted images to confirm final infarction size.

3.4.1 Normal Volunteer Study

A representative example from a normal volunteer is shown in Figures 3.9 and 3.10. A PWI image is shown in Fig. 3.9. Local AIFs were defined for each 5×5 ROI throughout the brain parenchyma, and CBF was then estimated by deconvolving the tissue curve with either the global AIF or the local AIF using standard SVD for each voxel. Percentage CBF and MTT difference maps are demonstrated in Fig. 3.10(a) and Fig. 3.10(b) respectively. By defining a local AIF using the estimated bolus arrival time for each 5×5 ROI, as anticipated, similar CBF and MTT values are observed comparing to those obtained using the global AIF method since the bolus delay is expected to be small for normal volunteer study.

Pooled results obtained using either the global AIF or the local AIFs are summarized in Fig. 3.11 for normal volunteer study. Consistent with what is shown in the percentage CBF and MTT maps, statistical analysis based on a paired t-test reveals that the CBF values obtained using the global AIF (47.60 ± 15.25 ml/100g/min) are comparable to those obtained using the local AIFs (49.31 ± 15.83 ml/100g/min) ($P > 0.05$). Similarly, the MTT values obtained using the global AIF (3.66 ± 0.29 sec) are comparable to those obtained using the local AIFs (3.50 ± 0.23) ($P > 0.1$).

3.4.2 Acute Stroke Patient Study

A representative example from an acute stroke patient with large ischemic lesion is shown in Figures 3.12-3.14. Acute DWI and 3-month follow-up T_2 images are shown in Fig. 3.12(a) and Fig. 3.12(b) respectively, delineating the presence and extent of the ischemic lesions. Local AIFs were defined for each 5×5 ROI throughout the brain parenchyma, and CBF was then estimated by deconvolving the tissue curve with either the global AIF

or the local AIF using standard SVD for each voxel. Percentage CBF and MTT difference maps are shown in Fig. 3.13(a) and Fig. 3.13(b) respectively. It has been shown that the presence of the bolus delay can induce CBF underestimation and MTT overestimation when the global AIF leads the tissue curves [49–51]. Note that in regions marked by arrows, the normalized CBF percentage differences are negative and the percentage MTT differences are positive, suggesting that CBF was underestimated by using global AIF. This produces prolonged MTT which exhibits regions of hypoperfusion inconsistent with the final lesion demonstrated on the 3-month follow-up T_2 image. When the global AIF leads the tissue curves significantly, by using a local AIF, as anticipated, higher CBF and shorter MTT values are present within the large ischemic lesion region (marked by the arrows). Apparently, the proposed approach substantially minimizes the delay between the AIFs and tissue curves as shown in Fig. 3.13. In addition, as illustrated in Fig. 3.14, the local AIF method has a higher ROC curve (dash-dot line) than the global AIF method (solid line) and the AUCs are 0.75 and 0.71 for the local AIF and global AIF methods respectively, suggesting that the local AIF method performs better than the global AIF method. Moreover, when tissue was classified as abnormal if the MTT values were greater than two SDs from the mean MTT measured in the contralateral hemisphere, one of the most commonly used thresholds in determining MTT abnormality, the two methods have a comparable TPR of 0.67. The local AIF method, on the other hand, has a smaller FPR of 0.28 in comparison to the global AIF method (FPR = 0.31). Note also that the LAIF-based ROC curve appears more sensitive than the GAIF-based curve at high FPR values (FPR>0.25). In contrast, the GAIF-based algorithm has greater sensitivity in ranges of high specificity (FPR<0.25). As demonstrated in Fig. 3.14, in light of the ability of the local AIF method to minimize the bolus delay thus yielding regions of hypoperfusion expectedly more consistent with the final infarction, the local AIF method can effectively reduce the FPR.

A representative example from another acute stroke patient with a small ischemic lesion is shown in Figures 3.15-3.17. Acute DWI and 1-month follow-up T_2 images are shown in Fig. 3.15(a) and Fig. 3.15(b) respectively, delineating the presence and extent of the ischemic lesions. Percentage CBF and MTT difference maps are demonstrated in Fig. 3.16(a) and Fig. 3.16(b) respectively. Although higher CBF and shorter MTT are still observed using the local AIFs within the lesion (marked by the arrows), as illustrated in Fig. 3.17, the local AIF method has a comparable ROC curve (dash-dot line, AUC=0.67)

	Global AIF	Local AIFs
AUC	0.71	0.73
TPR	0.57	0.52
FPR	0.22	0.16

Table 3.1: Performance comparison between the two methods

as the global AIF method (solid line, AUC = 0.65). Moreover, when tissue was classified as abnormal if the MTT values were greater than two SDs from the mean MTT measured in the contralateral hemisphere, the two methods have comparable FPRs (GAIF: FPR = 0.10, LAIF: FRP = 0.08), although the local AIF method has a larger TPR of 0.27 in comparison to the global AIF method (TPR = 0.23). Our approach is, hence, less effective in acute stroke patients with small ischemic lesions when the bolus delays between the global AIF and tissue curves are small.

This local AIF method was tested on data obtained from five acute stroke patients with various cerebrovascular abnormalities due to MCA occlusion. Fig. 3.18 shows the ROC curves of the pooled results across all five acute stroke patients. In addition, the AUC, the TPR and the FPR when tissue was classified as abnormal by the MTT values exceeding two SDs above the mean MTT measured in the contralateral hemisphere, are summarized in Table 3.1 for the two methods. Although the AUCs are similar for the two methods (global AIF: AUC = 0.71, local AIF method: AUC = 0.73), the local AIF method provides a better tradeoff in terms of preserving a high TPR at low FPR.

While the proposed temporal ICA approach is highly effective in minimizing bolus delay on flow quantification, it should be noted that the AUCs of the pooled results for the global AIF and local AIF methods are similar. Several potential factors could account for this observation. First, the local AIF method may be less effective for patients with small ischemic lesions as shown in Fig. 3.17. For a patient with a large ischemic lesion, significant delays between the global AIF and the tissue curves are anticipated, particularly around ischemia lesions with delayed and reduced blood perfusion. This could potentially lead to underestimation of CBF and overestimation of MTT, hence inducing higher FPR. By defining a local AIF using the estimated bolus arrival time for each 5×5 ROI, in contrast, bolus delay can be effectively minimized. As demonstrated from Fig.3.14, the local AIF method has larger TPR especially at high values of FPR, indicating the FPR may be

effectively reduced. On the other hand, for a patient with a small ischemic lesion, the bolus delays between the global AIF and tissue curves are less severe, thus the two methods are anticipated to have similar performance. Since we tested the two methods on data acquired from five stroke patients with various cerebrovascular abnormalities, it is possible that the advantage of the local AIF method over the global AIF method may diminish.

Second, the FPR value depends on both the false positive and the true negative. As shown in Fig. 3.19, suppose the region inside the red ellipse is the final infarction, while the region inside the blue ellipse is the acute MTT abnormality. Then the ipsilateral hemisphere (or even the whole brain parenchyma) can be segmented into true negative, false negative, true positive and false positive voxels. Although the local AIF may effectively reduce the number of false positive voxels especially for patients with large ischemic lesions, as shown in Fig. 3.19, the number of false positive voxels is normally much smaller than the number of true negative voxels, resulting in a less improvement in FPR, which is computed as the ratio between FP to the sum of FP and TN. This may be another potential reason why only slightly improved ROC curve from the local AIF method is observed in Fig. 3.18.

In summary, although the sample size is limited in our test, we have demonstrated that temporal ICA may be applied to define a local AIF for each 5×5 ROI throughout the brain parenchyma, such that bolus delay is corrected, while at the same time the general shape of AIF is preserved. In addition, recirculation and noise can also be removed to improve SNR. By using this alternative approach, accurate CBF estimation may thus be obtained using standard SVD with assumed minimal delays between the local AIFs and tissue curves.

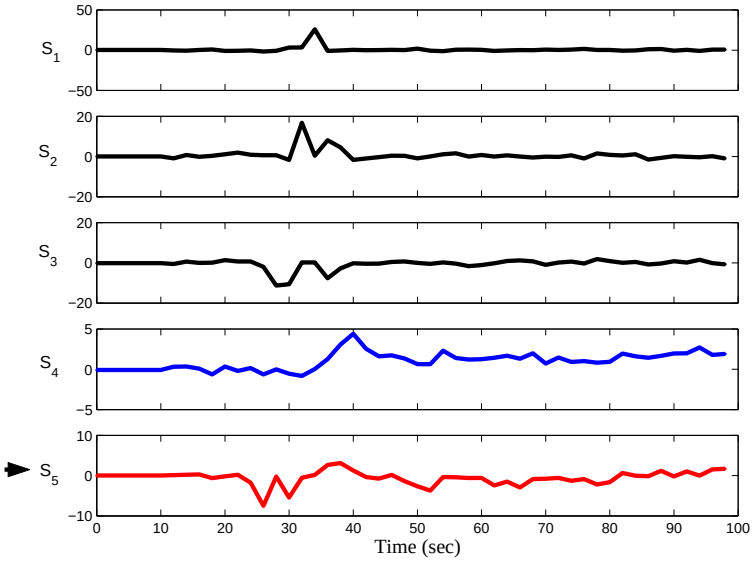

(a) Contralateral ROI

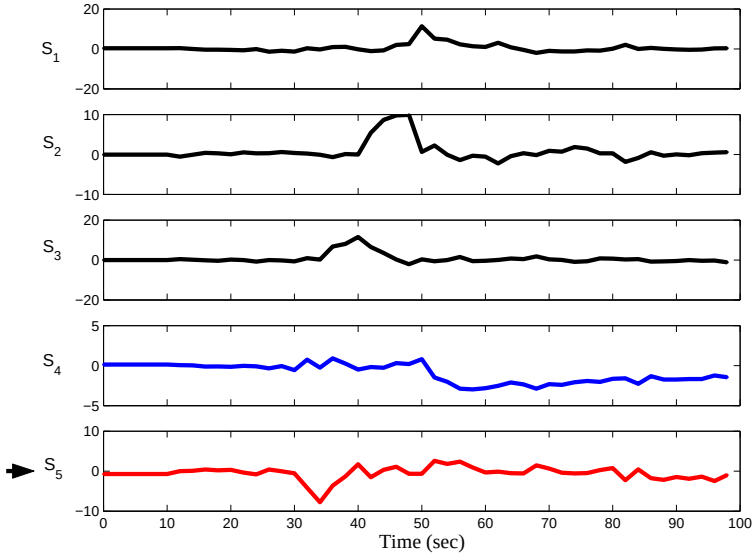

(b) Infarction ROI

Figure 3.7: ICA analysis of tissue curves from the two ROIs shown in Fig. 3.6

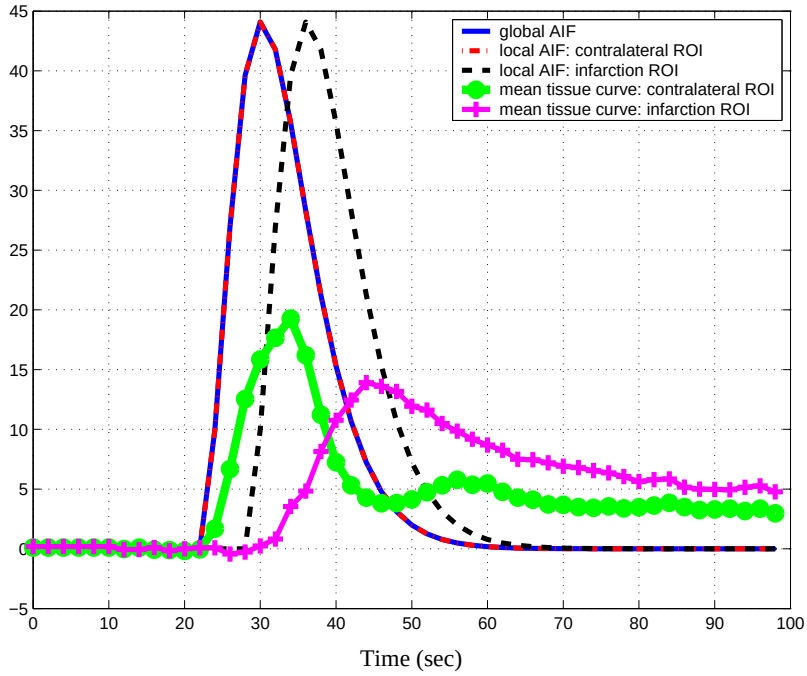

Figure 3.8: Global and local AIFs defined for the two ROIs shown in Fig. 3.6

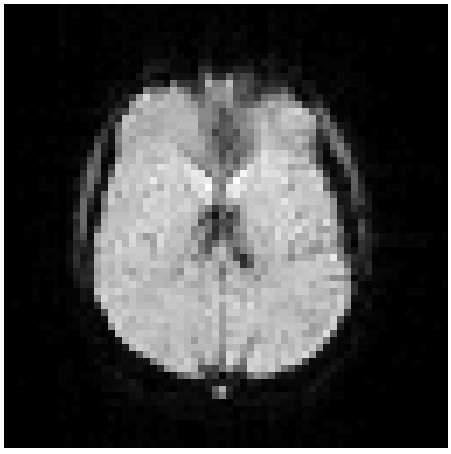

Figure 3.9: A PWI image of a normal volunteer

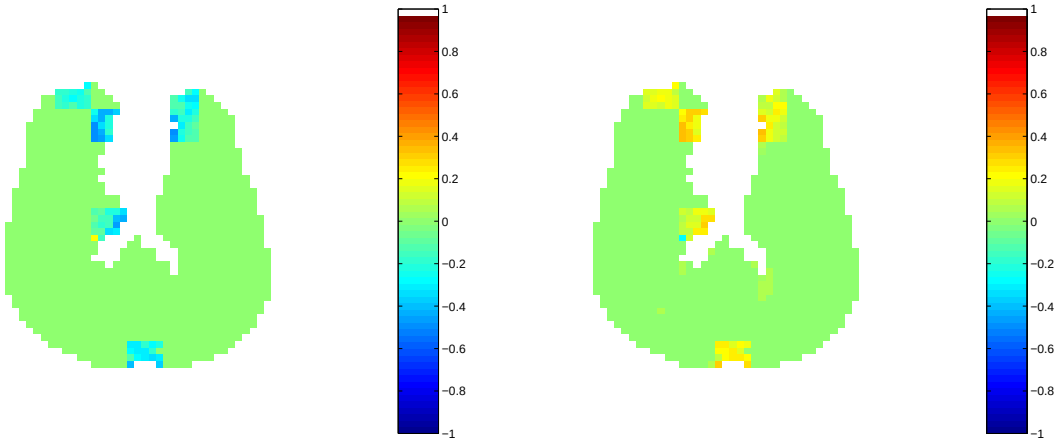

(a) ΔCBF (b) ΔMTT

Figure 3.10: Percentage CBF and MTT differences of the same normal volunteer as shown in Fig. 3.9

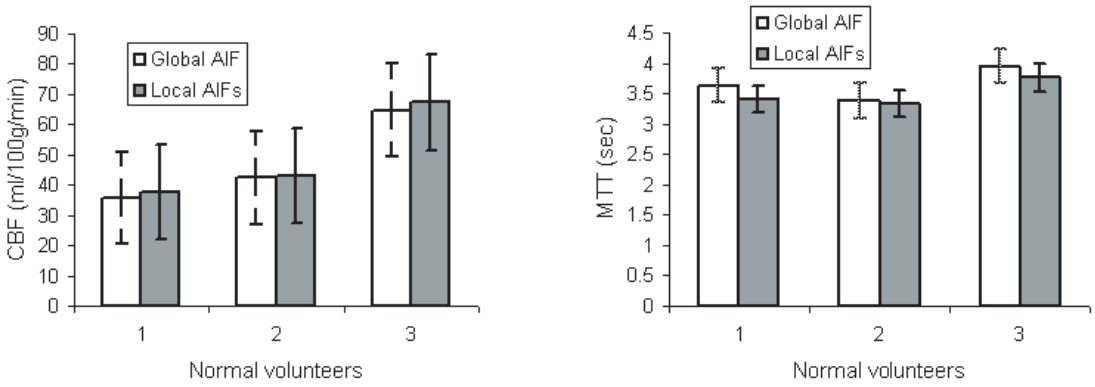

(a) CBF (b) MTT

Figure 3.11: Pooled results across all three normal volunteers are shown. The error bars represent 1 standard deviation.

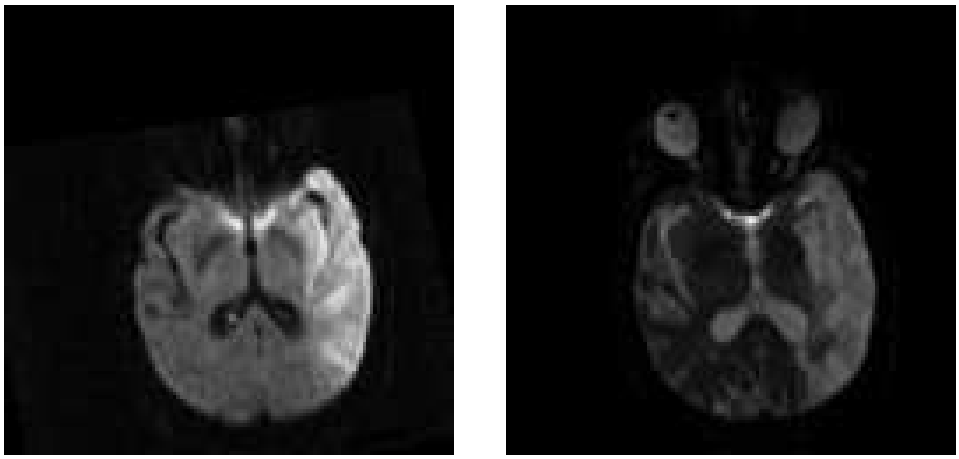

(a) Acute DWI image (b) Follow-up T_2-weighted image

Figure 3.12: Acute DWI and follow-up T_2-weighted images of an acute stroke patient with large ischemic lesion

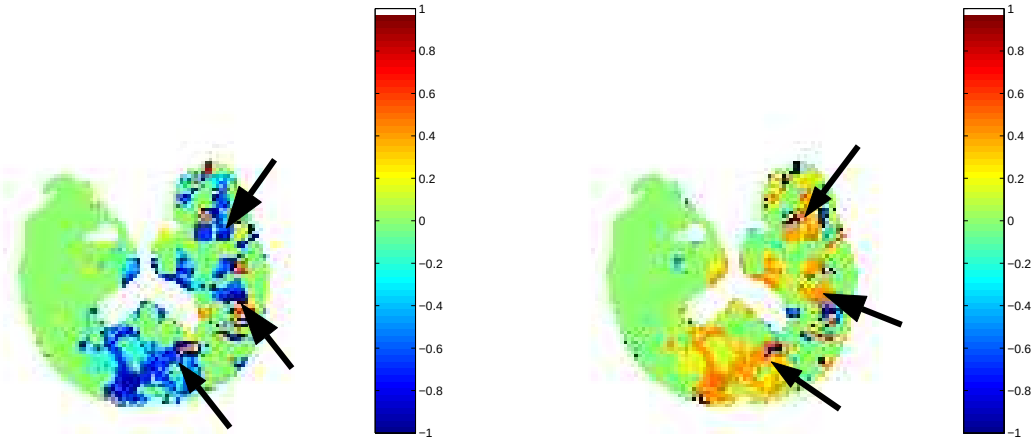

(a) ΔCBF (b) ΔMTT

Figure 3.13: Percentage CBF and MTT differences of the same acute stroke patient as shown in Fig. 3.12

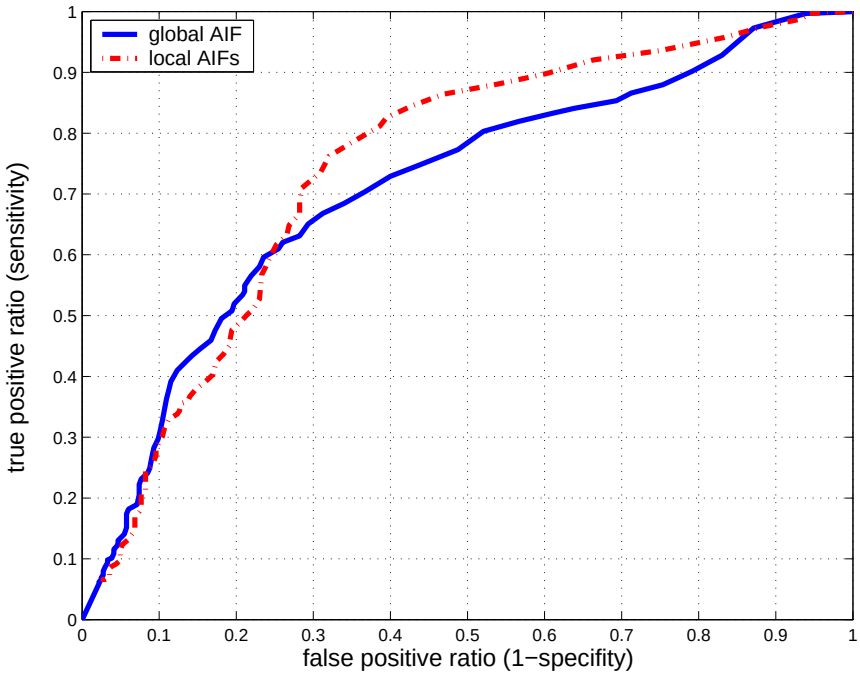

Figure 3.14: ROC curve of the same acute stroke patient as shown in Fig. 3.12

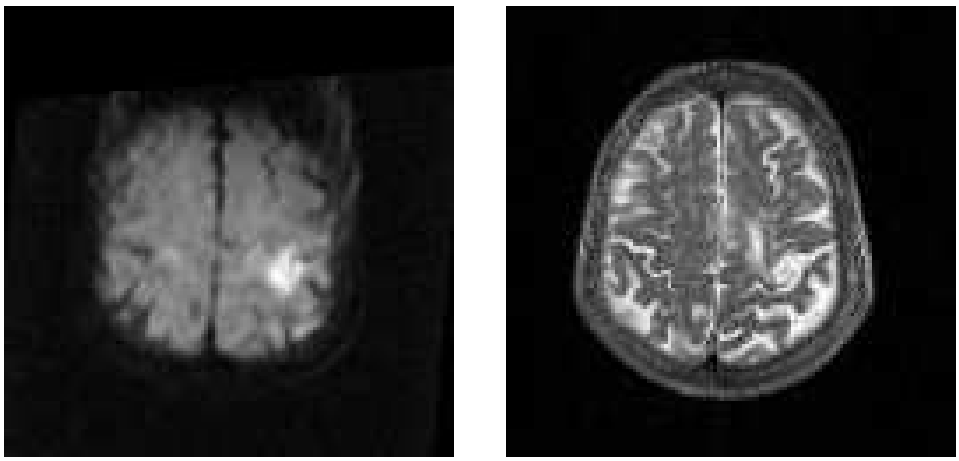

(a) Acute DWI image

(b) Follow-up T_2-weighted image

Figure 3.15: Acute DWI and follow-up T_2-weighted images of another acute stroke patient with small ischemic lesion

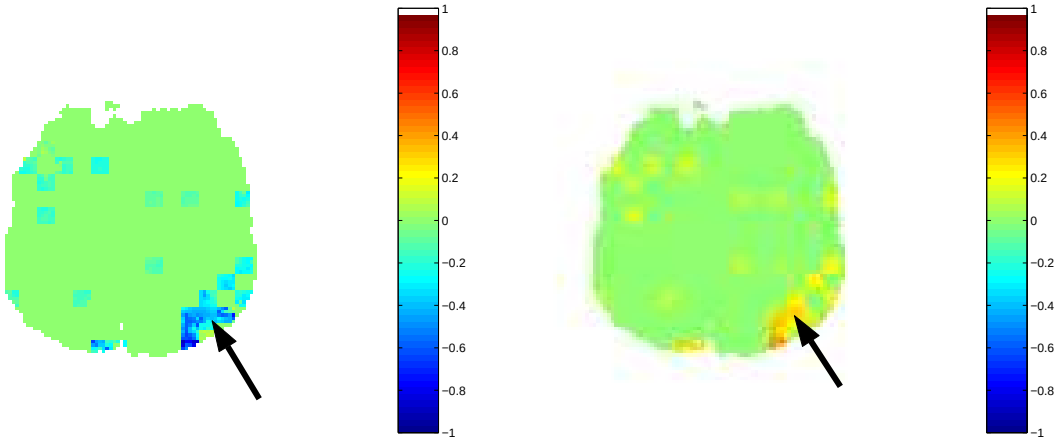

(a) ΔCBF (b) ΔMTT

Figure 3.16: Percentage CBF and MTT differences of the same acute stroke patient as shown in Fig. 3.15

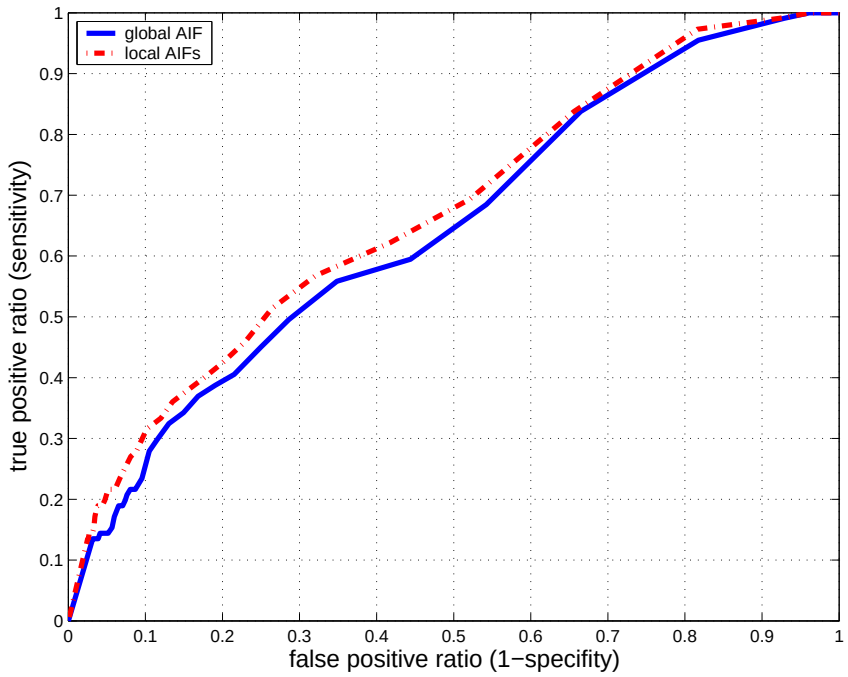

Figure 3.17: ROC curve of the same acute stroke patient as shown in Fig. 3.15

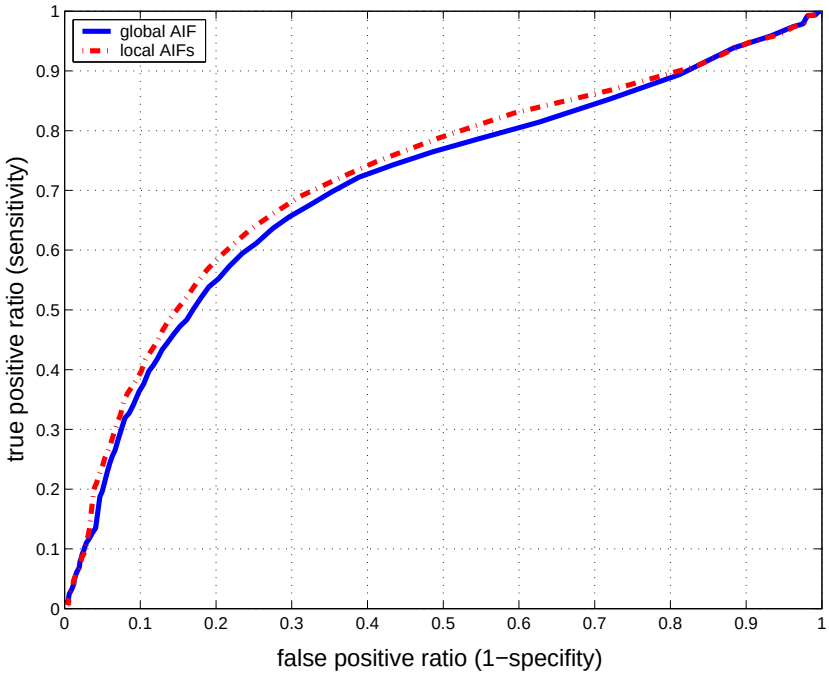

Figure 3.18: ROC curves of the pooled results from the two methods across all 5 patients

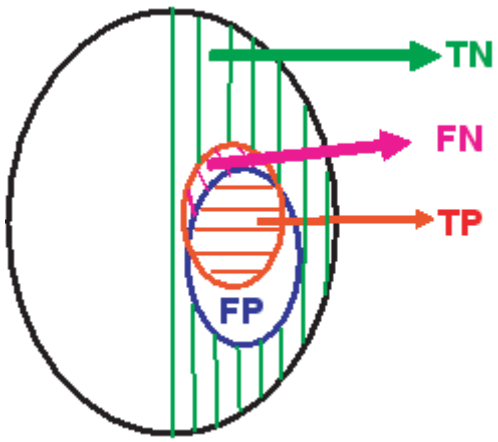

Figure 3.19: Schematic illustration of the computation of FPR

Chapter 4

Intracranial Vascular Transfer Function in Acute Stroke Patients

4.1 Introduction

Analysis of the transfer function has been widely used to characterize an unknown system, which can be a piece of hardware or a biological system. In dynamic contrast susceptibility MR approaches, we consider a vascular flow system. Since in general the vascular structure consists of multiple smaller blood vessels, depending on the paths and travelling velocities, flow particles entering the ROI at the same time may require different time to pass the vascular system. In this case, a distribution of vascular transit time needs to be accounted for. In DSC MR approaches, vascular transfer function represents the probability density function of the vascular transit time.

In DSC MR approaches, CBF quantification requires knowledge of the AIF, which is the concentration of contrast agent entering the ROI at time t. This is normally measured from a major artery. However, in case of cerebrovascular disease, as shown in Fig. 4.1, the arterial input functions may be distorted due to an abnormal flow pattern. For example, assume $AIF_{in}(t)$ is the AIF measured before the dispersion source, while $AIF_{out}(t)$ is the AIF measured after the dispersion source. Then $AIF_{out}(t)$ is the convolution of $AIF_{in}(t)$

and the vascular transport function, $VTF(t)$, as shown in Eq. (4.1),

$$AIF_{out}(t) = AIF_{in}(t) * VTF(t), \tag{4.1}$$

where $*$ denotes linear convolution.

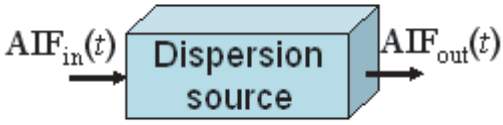

Figure 4.1: Distortion of the AIF due to abnormal flow pattern

Our ability to estimate the intracranial vascular transfer function non-invasively should potentially provide highly relevant physiological information, particularly in patients with cerebrovascular diseases. In this study, we aim to investigate how intracranial vascular transfer function potentially differs among different ROIs in acute stroke patients using MR perfusion-weighted images.

The widely employed DSC MR approach was used to acquire MR PWI images, and spatial ICA was applied to determine local AIFs [33]. Voxel-by-voxel VTF was subsequently derived through the deconvolution of the LAIFs with a global AIF using cSVD as reflected by

$$C_{LAIF}(x,t) = C_{GAIF}(t) * VTF(x,t), \tag{4.2}$$

where the GAIF was obtained from either the contralateral or ipsilateral MCA. Results from acute stroke patients will be provided to demonstrate the ability to non-invasively depict VTF and to potentially offer new insights into blood flow related alterations in acute stroke patients.

4.2 Constructing Local Arterial Input Function

The susceptibility related MR signal changes were first converted to concentration time curves. Two global AIFs were obtained by averaging contrast induced MR signal

changes from the contralateral (CGAIF) and ipsilateral (IGAIF) middle cerebral arteries, with recirculation effects removed using gamma-variate fitting.

4.2.1 Spatial Independent Component Analysis

At any voxel, we assume a temporal concentration signal is resulted from M spatially segregated and statistically independent sources such as arterial sources, venous sources, tissue sources and artifact sources (e.g. movement and scanner drift). These may be added linearly, and the observed temporal concentration signal is thus, the superposition of the signal intensities of the M spatial sources weighted by their fractional expression volumes in the voxel and as written in

$$C(x_i, t_j) = \sum_{k=1}^{M} s_k(t_j) a_k(x_i) \quad (i = 1, \cdots, V; j = 0, \cdots, N-1), \tag{4.3}$$

where $C(x_i, t_j)$ is the concentration time curve of voxel x_i at time t_j, $s_k(t_j)$ is the concentration signal intensity of the k^{th} spatial independent component at time t_j, $a_k(x_i)$ is the expression level of the k^{th} spatial IC at voxel x_i, N is the number of measurements, V is the number of the entire brain parenchyma voxels, and M is the number of spatial ICs throughout the brain parenchyma.

Spatial ICA on the basis of Infomax with maximal likelihood formulation analysis (ICAML) [19] was applied to decompose the concentration time curves $C(x, t)$ into different spatial independent components throughout the entire brain parenchyma. Bayesian Information criterion was again invoked to estimate the optimal number of spatial independent components throughout the whole brain parenchyma. We have determined that ten ICs can account for most of the signal variation, so that the number of sources, M, was fixed to 10 in this study.

4.2.2 Identifying Arterial Spatial Sources

Local arterial sources were identified on the basis of both the spatial mappings and the temporal characteristics of the components [33]. For example, the acute DWI and follow-up T_2 images acquired from an acute stroke patient are shown in Fig. 4.2(a) and Fig.4.2(b) respectively, where the green line in each map delineates the boundary

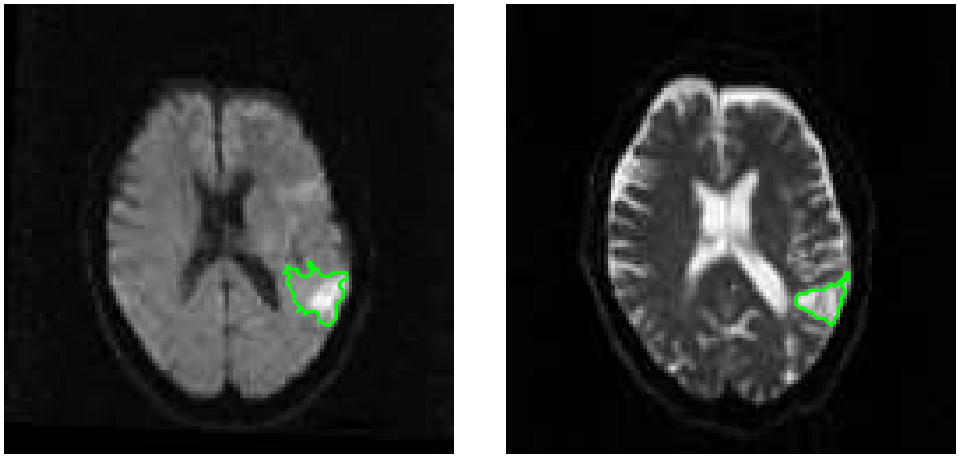

(a) Acute DWI image (b) Follow-up T_2-weighted image

Figure 4.2: Acute DWI and follow-up T_2-weighted images of an acute stroke patient

of the abnormal area. Fig. 4.3 shows the spatial ICA analysis of the acute PWI data acquired from the same stroke patient. Fig. 4.3(a) illustrates the spatial mapping of the 10 components, i.e $a_1(x), \cdots, a_{10}(x)$, while Fig. 4.3(b) shows the temporal characteristics of the corresponding components. For each spatial independent component, the contribution of its temporal concentration signal to the concentration time curve obtained at a given voxel, x, is $a_k(x)$ $(k = 1, \cdots, 10)$. To find the locations where each component is highly expressed, a mask, $m_k(x)$, was first defined such that only voxels with 5% highest expression level were chosen. Having tried different mask thresholds such as 5%, 10%, 20%, 30%, and 40%, it appeared that when voxels with 5% highest expression levels were chosen for each component, the mask included highly expressed voxels which are consistent with the anatomic distribution of each spatial component. Fig. 4.4(a) shows the highly expressed voxels overlaid on the acute PWI images. For example, IC1 is highly expressed at voxels marked by red dots, while IC10 is highly expressed at voxels marked by yellow dots in the spatial map.

Nonarterial components were next discarded on the basis of both spatial maps and temporal characteristics. For example, according to the temporal characteristics shown in Fig. 4.3(b), IC10 cannot not be an arterial component. On the other hand, IC1 and IC8 are highly expressed in veins/tissues as demonstrated from the masks shown in Fig. 4.4(a).

In addition, by comparing the spatial maps of IC6 and IC9 to the acute DWI and follow-up T_2 images shown in Fig. 4.2, we find that both IC6 and IC9 are predominantly expressed at the lesions, and should hence be discarded as well. In contrast, IC2, IC3, IC4, IC5 and IC7 are well expressed at small arteries.

4.2.3 Constructing Local Arterial Dataset

A local AIF dataset may be constructed using the remaining arterial components and the corresponding masks as detailed in Eq. (4.4).

$$C_{LAIF}(x_i, t_j) = \sum_{k=1}^{10} s_k(t_j) a_k(x_i) m_k(x_i) \quad (i = 1, \cdots, V; j = 0, \cdots, N-1). \tag{4.4}$$

Fig. 4.4(b) shows a set of 9 images of the constructed arterial dataset during the bolus passage for the acute PWI data acquired from the same patient whose data is shown in Fig. 4.2. The numbers inserted on each image correspond to the acquisition image order.

Some brain parenchyma voxels may, however, have no ICA-defined local AIF. In this case, an approximated local AIF may be obtained using the local AIFs defined for the neighboring voxels. For any voxel x_j with no ICA-defined local AIF, a Gaussian-weighting updating was applied to approximate the AIF from the surrounding voxels whose AIF $C_{LAIF}(x_i, t)$ were given according to their distance d_{ij} by

$$\begin{cases} C_{LAIF}(x_j, t) = \dfrac{\sum\limits_i w(d_{ij}) C_{LAIF}(x_i, t)}{\sum\limits_i w(d_{ij})}, \\ w(d_{ij}) = \exp(-\frac{d_{ij}^2}{2\sigma^2}), \end{cases} \tag{4.5}$$

where $\sigma = 5$-pixel was chosen empirically and the Gaussian-weighting was truncated to 5×5 pixels to avoid nonlocal contribution.

The constructed arterial dataset was then smoothed using a 3×3 uniform kernel. In addition, using gamma-variate fitting, recirculation was removed from each of the constructed concentration time curves.

4.3 Circular Convolution

Suppose we have two discretized temporal signals of length N, i.e. $x(n) = \{x(0), \cdots, x(N-1)\}$ and $h(n) = \{h(0), \cdots, h(N-1)\}$. We then zero-pad these two series to length of $2N$, i.e. $x^p(n) = \{x(0), \cdots, x(N-1), 0, \cdots, 0\}$ and $h_p(n) = \{h(0), \cdots, h(N-1), 0, \cdots, 0\}$. Let $y(n)$ be the linear convolution of $x^p(n)$ and $h^p(n)$ as shown in Eq. (4.6), and $z(n)$ be the circular convolution of $x^p(n)$ and $y^p(n)$ as given by Eq. (4.7),

$$y(n) = x_p(n) * h_p(n) = \sum_{i=0}^{2N-1} x_p(i)h_p(n-i) = \sum_{i=0}^{N-1} x_p(i)h_p(n-i) \ \ (0 \le n \le 4N-2), \quad (4.6)$$

$$z(n) = x_p(n) \otimes h_p(n) = \sum_{i=0}^{2N-1} x_p(i)[h_p(n-i)_{2N}] \ \ (0 \le n \le 2N-1), \quad (4.7)$$

where $*$ and $\otimes$ denote respectively a linear convolution and a circular convolution.

The first $2N$ values of $y(n)$ may then be expressed using a vector form as in Eq. (4.8).

$$\begin{pmatrix} y(0) \\ y(1) \\ \vdots \\ y(2N-1) \end{pmatrix} = \begin{pmatrix} x^p(0) & 0 & \cdots & 0 \\ x^p(1) & x^p(0) & \cdots & 0 \\ \vdots & \vdots & \vdots & \vdots \\ x^p(2N-1) & x^p(2N-2) & \cdots & x^p(0) \end{pmatrix} \cdot \begin{pmatrix} h^p(0) \\ h^p(1) \\ \vdots \\ h^p(2N-1) \end{pmatrix} \quad (4.8)$$

Define $c = [y(0), y(1), \cdots, y(2N-1)]^T$, $b = [h^p(0), h^p(1), \cdots, h^p(2N-1)]^T$, and

$$A = (a_{ij})_{2N \times 2N} = \begin{pmatrix} x^p(0) & 0 & \cdots & 0 \\ x^p(1) & x^p(0) & \cdots & 0 \\ \vdots & \vdots & \vdots & \vdots \\ x^p(2N-1) & x^p(2N-2) & \cdots & x^p(0) \end{pmatrix},$$

Eq. (4.8) may be written as,

$$c = A \cdot b. \quad (4.9)$$

Similarly, $z(n)$ may be rewritten as Eq. (4.10) by defining $\tilde{c} = [z(0), z(1), \cdots, z(2N-1)]^T$ and

$$D = \begin{pmatrix} x^p(0) & x^p(2N-1) & \cdots & x^p(N+1) & x^p(N) & \cdots & x^p(2) & x^p(1) \\ x^p(1) & x^p(0) & \cdots & x^p(N+2) & x^p(N+1) & \cdots & x^p(3) & x^p(2) \\ \vdots & \vdots & \vdots & \vdots & & & & \\ x^p(N-1) & x^p(N-2) & \cdots & x^p(0) & x^p(2N-1) & \cdots & x^p(N+1) & x^p(N) \\ x^p(N) & x^p(N-1) & \cdots & x^p(1) & x^p(0) & \cdots & x^p(N+2) & x^p(N+1) \\ \cdots & \cdots & \cdots & \cdots & \cdots & \cdots & \cdots & \cdots \\ x^p(2N-2) & x^p(2N-3) & \cdots & x^p(N-1) & x^p(N-2) & \cdots & x^p(0) & x^p(2N-1) \\ x^p(2N-1) & x^p(2N-2) & \cdots & x^p(N) & x^p(N-1) & \cdots & x^p(1) & x^p(0) \end{pmatrix},$$

$$\tilde{c} = D \cdot b. \tag{4.10}$$

Let the i, j^{th} element of D be d_{ij} $(i = 1, \cdots, 2N; j = 1, \cdots, 2N)$. Then comparing D with A, we have:

$$d_{ij} = \begin{cases} a_{ij} & j \leq i \\ a_{2N+i-j+1,1} & \text{otherwise} \end{cases} \tag{4.11}$$

From Eq. (4.6) and Eq. (4.7), it is very easy to show that the first $2N$ values of $y(n)$ are equal to $z(n)$. We hence have,

$$x^p(n) * h^p(n) = x^p(n) \otimes h^p(n) \ \ (n = 0, \cdots, 2N-1). \tag{4.12}$$

For example, Fig. 4.5 shows the original two temporal series, $x(n)$ and $h(n)$, and the zero-padded temporal series, $x^p(n)$ and $h^p(n)$. To illustrate the procedures of linear convolution and circular convolution, $h^p(n)$ was shifted as in Fig. 4.6(a) and circularly shifted as in Fig. 4.6(b), respectively. It is demonstrated from Fig. 4.7 that $y(n) = z(n)$, $(n = 0, \cdots, 2N-1)$.

4.4 Computing Vascular Transport Function

From Eq. (4.2), the voxel-by-voxel VTF, $T(x,t)$, may be obtained by deconvolving the constructed local arterial temporal signal with the global AIF. In case of cerebrovascular disease, if the patient has ipsilateral MCA stroke, when the global AIF is measured from

the highly diseased ipsilateral MCA, it may lag the constructed $C_{LAIF}(x,t)$ by a time delay τ. If causality is assumed, we may not be able to estimate the VTF correctly by SVD.

Suppose for a given voxel x, the VTF, $T(x,t)$ is known. We zero-pad $C_{GAIF}(t)$ and $T(x,t)$, to length $2N$, i.e. $C^p_{GAIF}(t) = \{C_{GAIF}(t_0), \cdots, C_{GAIF}(t_{N-1}), 0, \cdots, 0\}$ and $T^p(x,t) = \{T(x,t_0), \cdots, T(x,t_{N-1}), 0, \cdots, 0\}$. Let $C^p_{LAIF}(x,t)$ be the linear convolution of $C^p_{GAIF}(t)$ and $T^p(x,t)$. $C^p_{LAIF}(x,t)$ is also equivalent to the circular convolution of $C^p_{GAIF}(t)$ and $T^p(x,t)$ as shown by

$$C^p_{LAIF}(x,t) = C^p_{GAIF}(t) * T^p(x,t) = C^p_{GAIF}(t) \otimes T^p(x,t), \;\; (t = t_0, \cdots, t_{2N-1}). \tag{4.13}$$

$T^p(x,t)$ may thus be obtained by deconvolving $C^p_{LAIF}(x,t)$ with $C^p_{GAIF}(t)$ and $T(x,t)$ can subsequently be estimated by

$$T(x,t) = T^p(x,t), \;\; (t = t_0, \cdots, t_{N-1}). \tag{4.14}$$

With the inverse problem of interest in mind, and to estimate the VTF for any voxel x, we may zero-pad the constructed local AIF and the global AIF to $C^p_{LAIF}(x,t)$ and $C^p_{GAIF}(t)$ of length $2N$. A VTF of length $2N$, $T^p(x,t)$, can thus be estimated by deconvolving $C^p_{LAIF}(x,t)$ with the global AIF, $C^p_{GAIF}(t)$, measured from either the contralateral or the ipsilateral MCA using a circular singular value decomposition deconvolution approach, similar to that proposed in [56]. And $T(x,t)$ may thus be estimated using Eq. (4.14).

Let $t_k = k\Delta t \;\; (k = 0, \cdots, 2N-1)$. Since $C^p_{LAIF}(x,t)$ is the linear convolution of $C^p_{GAIF}(x,t)$ and $T^p(x,t)$, it can be expressed in a discretized form as Eq. (4.15).

$$C^p_{LAIF}(x_i,t_j) = \Delta t \cdot \sum_{k=0}^{j} C^p_{GAIF}(t_k) T^p(x_i, t_j - t_k) (i = 1, \cdots, V; j = 0, \cdots, 2N-1). \tag{4.15}$$

Eq. (4.15) may further be simplified into a vector form as Eq. (4.17) by defining $c = [C^p_{LAIF}(x_i,t_0), \cdots, C^p_{LAIF}(x_i,t_{2N-1})]^T$, $b = [T^p(x_i,t_0), \cdots, T^p(x_i,t_{2N-1})]^T$ and

$$A = \Delta t \cdot \begin{pmatrix} C^p_{GAIF}(t_0) & 0 & \cdots & 0 \\ C^p_{GAIF}(t_1) & C^p_{GAIF}(t_0) & \cdots & 0 \\ \vdots & \vdots & \vdots & \vdots \\ C^p_{GAIF}(t_{2N-1}) & C^p_{GAIF}(t_{2N-2}) & \cdots & C^p_{GAIF}(t_0) \end{pmatrix}, \tag{4.16}$$

$$c = A \cdot b. \tag{4.17}$$

The global AIF was prefiltered to reduce noise contributions and to compensate for discretization errors [2]. We hence can form a matrix $A = (a_{ij})_{2N\times 2N}$ with elements:

$$a_{ij} = \begin{cases} \Delta t \cdot \frac{C_{GAIF}(t_{i-j-1})+4C_{GAIF}(t_{i-j})+C_{GAIF}(t_{i-j+1})}{6} & 0 \le j \le i \\ 0 & \text{otherwise.} \end{cases}$$

However, from Eq. (4.13), $C^p_{LAIF}(x,t)$ is also equivalent to the circular convolution of $C^p_{GAIF}(t)$ and $T^p(x,t)$. By defining a block-circular matrix $D = (d_{ij})_{2N\times 2N}$, where the elements of D are given by

$$d_{ij} = \begin{cases} a_{ij} & j \le i \\ a_{2N+i-j+1,1} & \text{otherwise,} \end{cases} \tag{4.18}$$

the constructed local AIF signal can thus be expressed as

$$c = Db. \tag{4.19}$$

Assume the singular value decomposition of D is

$$D_{2N\times 2N} = USV^T, \tag{4.20}$$

where U and V are $2N\times 2N$ orthogonal matrices, the matrix $S = diag(S_{11}, S_{22}, \cdots, S_{2N\times 2N})$ is a nonnegative diagonal matrix and S_{ii} $(i = 1, \cdots, 2N)$ are the singular values. Only those singular values that are greater than a predefined SVD threshold are selected. The larger threshold is, the more immune the decomposition is to noise at a cost of a larger quantification bias.

Defining $W = S^{-1}$, and from Eq. (4.19-4.20), we get

$$D^{-1} = VWU^T, \tag{4.21}$$

$$\hat{b} = D^{-1}c. \tag{4.22}$$

The voxel-by-voxel circular deconvolution of the constructed local arterial dataset and the global AIF is hence $T^p(x,t)$ as shown in Eq. (4.23),

$$\hat{b} = VWU^T c. \tag{4.23}$$

To reduce the spurious oscillation resulted from the amplified leakage frequencies due to the discontinuity at the boundaries $t = 0$ and $t = 2N - 1$, a larger SVD threshold should be used for circular deconvolution. An oscillation index [51] shown in Eq. (4.24) is used,

$$O = \frac{1}{2N\hat{T}^p_{max}}(\sum_{k=2}^{2N-1} |\hat{T}^p(x,t_k) - 2\hat{T}^p(x,t_{k-1}) + \hat{T}^p(x,t_{k-2})|), \tag{4.24}$$

where $\hat{T}^p_{max}$ is the maximum of the estimated $T^p(x,t)$. The SVD threshold we used was 16%, i.e. only singular values larger than 16% of the largest singular value were selected to ensure the oscillation index falls below 10%. $T(x,t)$ $(t = t_0, \cdots, t_{N-1})$ can finally be estimated by Eq. (4.14).

4.5 Statistical Analysis

DWI images depict random motion of water protons. In cerebral ischemia regions, the motion of protons is restricted leading to a reduction of the apparent diffusion coefficient of water and an increase in signal intensity in DWI images. In contrast, hemodynamic parameters can be obtained from PWI images, which may provide physiological information about the pathologically hypoperfused regions ahead of irreversible brain tissue damage taking place.

It has been shown that the hypoperfused region depicted by acute PWI abnormality may be much larger than the acute DWI abnormality [57–60]. Moreover, the acute DWI abnormality has been presumed as an estimate of the ischemic core (i.e. irreversibly damaged tissue), while the mismatched region between acute PWI abnormality and acute DWI abnormality, i.e. PWI/DWI mismatch, has been shown to be a good estimate of the ischemic penumbra [57–59, 61–64]. As shown in Fig. 4.8, the ischemic penumbra refers to hypoperfused but still viable tissue that may be salvaged if perfusion can be restored on time [65, 66]. The PWI/DWI mismatch is thus, helpful in making therapeutic decision about acute-phase treatment [67–70].

The purpose of our study is to investigate how VTF differs among different brain regions, especially those abnormal areas depicted in the acute phase on DWI and PWI images, as well as the final infarction as delineated in the chronic phase on T_2-weighted images for acute stroke patient study. Relative Mean transit time maps were computed to delineate acute PWI abnormality by Eq. (4.25), which requires less postprocessing,

$$rMTT(x,t) = \frac{\int tC(x,t)}{\int C(x,t)}, \tag{4.25}$$

where $C(x,t)$ is the concentration temporal curve at voxel x after removing recirculation effects.

The mean and standard deviation of the values from the contralateral hemisphere were computed for lesion segmentation. Any voxels with intensity larger than mean+2SD in each of the acute DWI, acute rMTT and follow-up T_2 maps were declared as acute DWI abnormality, acute PWI abnormality, and final infarction, respectively.

A ROI approach was employed to quantitatively characterize how VTF differs among different brain regions. For acute stroke patients, acute DWI, acute rMTT and follow-up T_2 images were employed to define three ROIs, namely, core regions defined as the intersection of acute DWI and PWI abnormalities, PWI/DWI mismatched regions and final T_2 infarction. A normal ROI was defined in the contralateral hemisphere. For comparison purpose, two ROIs were selected in the two hemispheres for the normal volunteers.

Finally, FWHM and power of the first mode of VTF (EVTF) were computed to quantitatively determine the discrepancies among the predefined ROIs. For stroke patient study, the mean ETVF obtained in each abnormal ROI was normalized to that obtained from the contralateral ROI. In the normal volunteer group, mean EVTF encompassing one ROI was normalized to that obtained from the other ROI for comparison. Statistical analysis based on paired t-test was employed to compare FWHM and EVTF among different ROIs. A P-value less than 0.05 was considered significantly different.

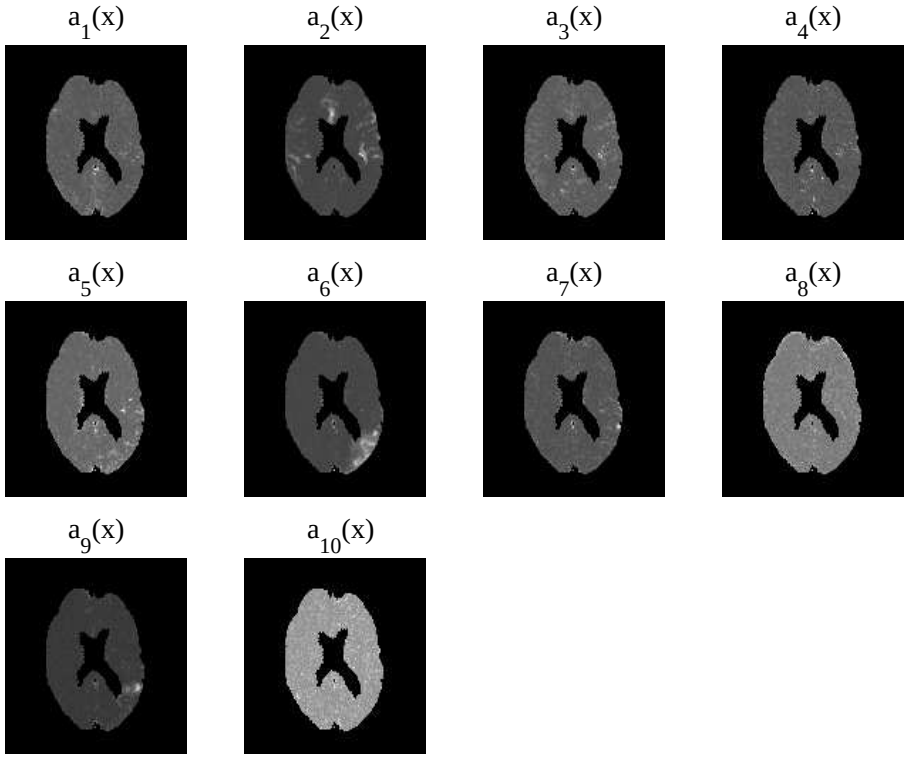

(a) Spatial maps of the independent components

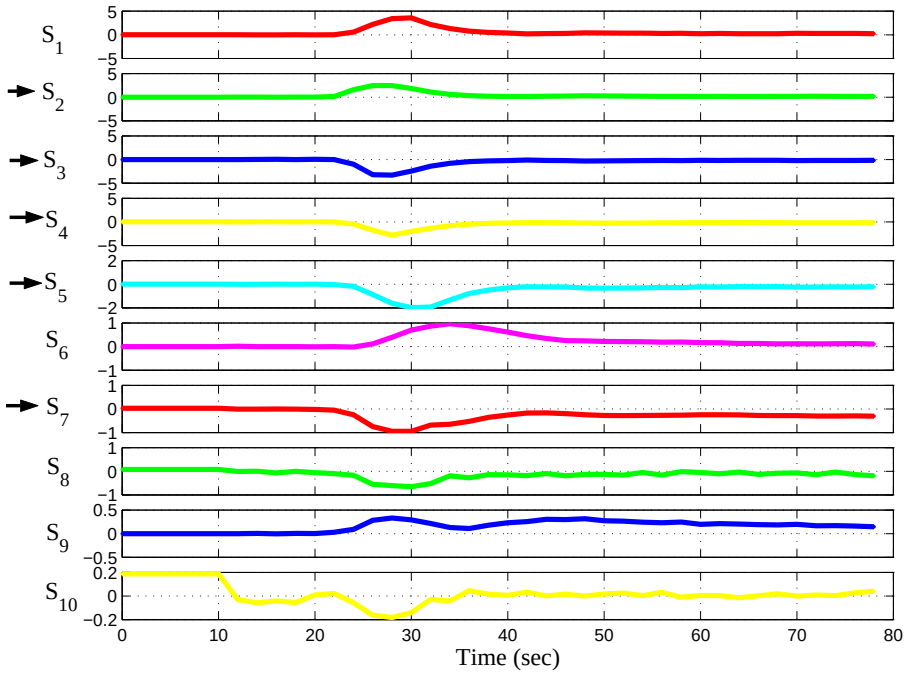

(b) Temporal characteristics of the spatial components

Figure 4.3: Spatial ICA analysis of acute PWI data acquired from the patient shown in Fig.4.2

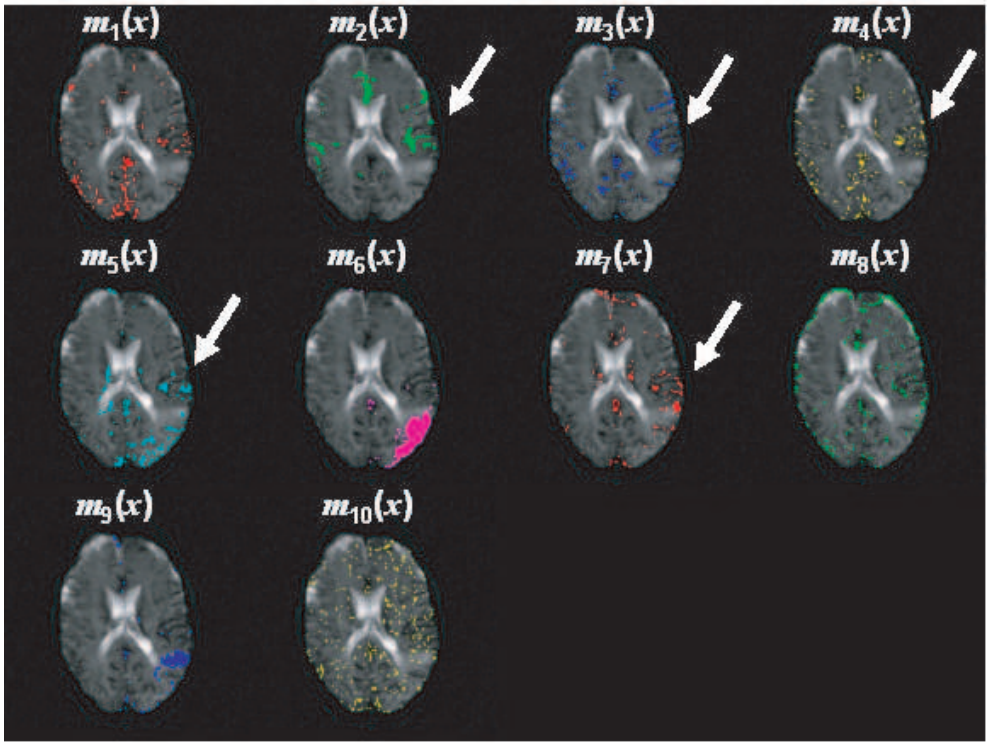

(a) Highly expressed voxels overlaid on the acute PWI images

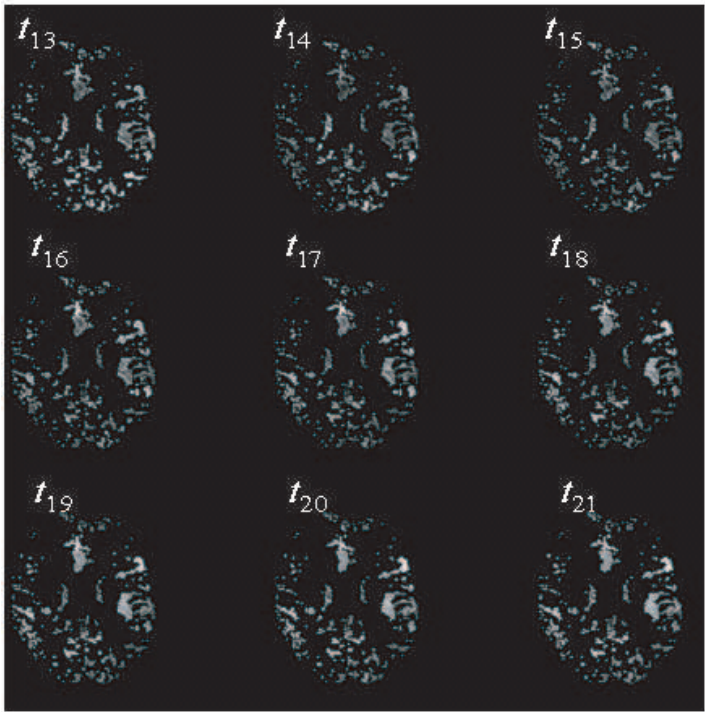

(b) A set of 9 images (during bolus passage) of the arterial dataset

Figure 4.4: Masks and the computed arterial dataset for the same data shown in Fig. 4.2

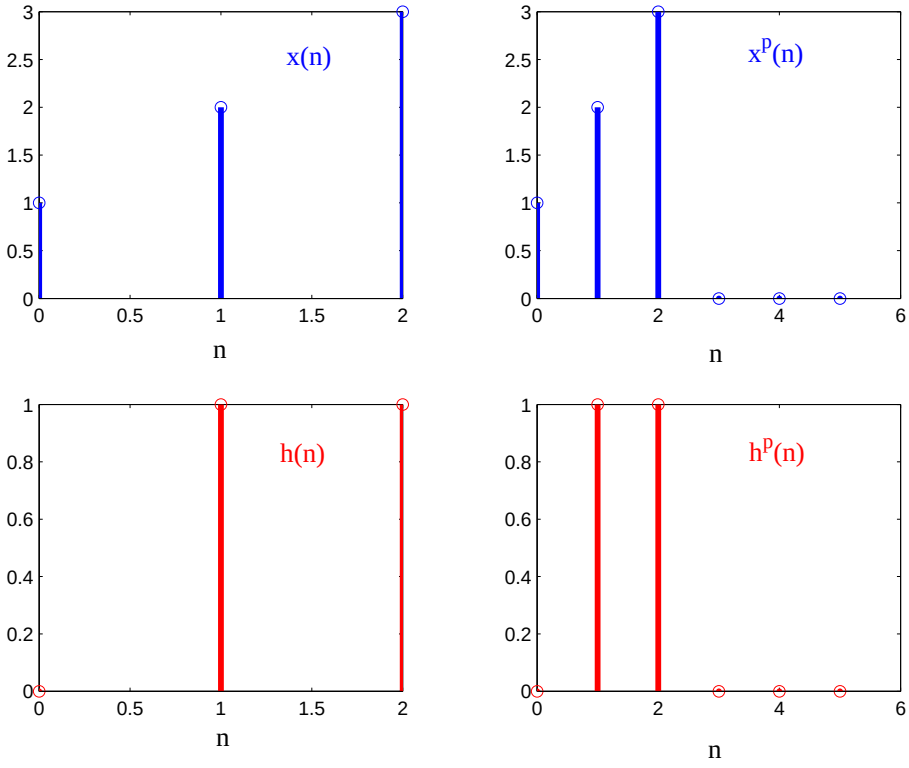

Figure 4.5: Original and zero-padded temporal series

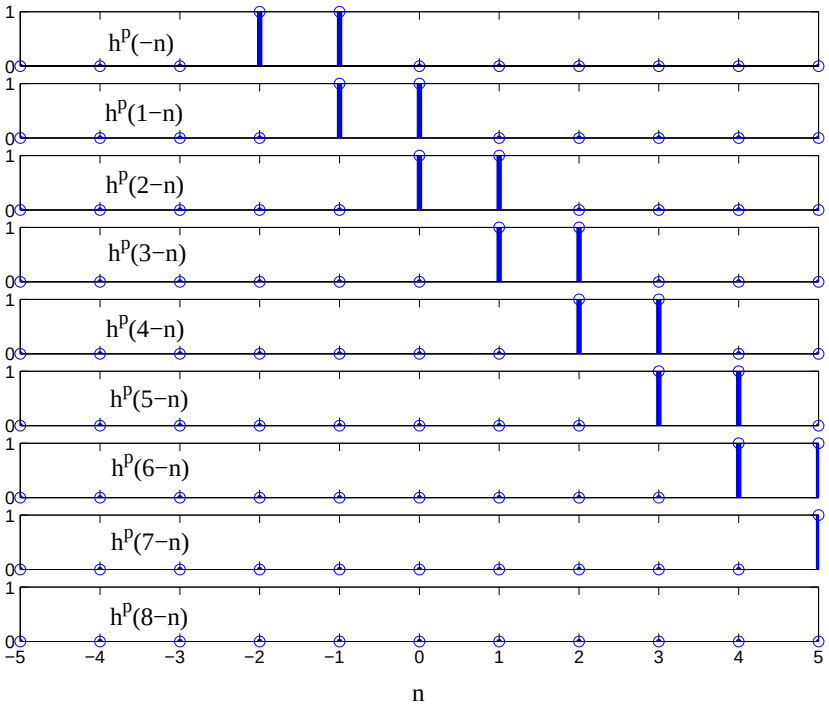

(a) Shift

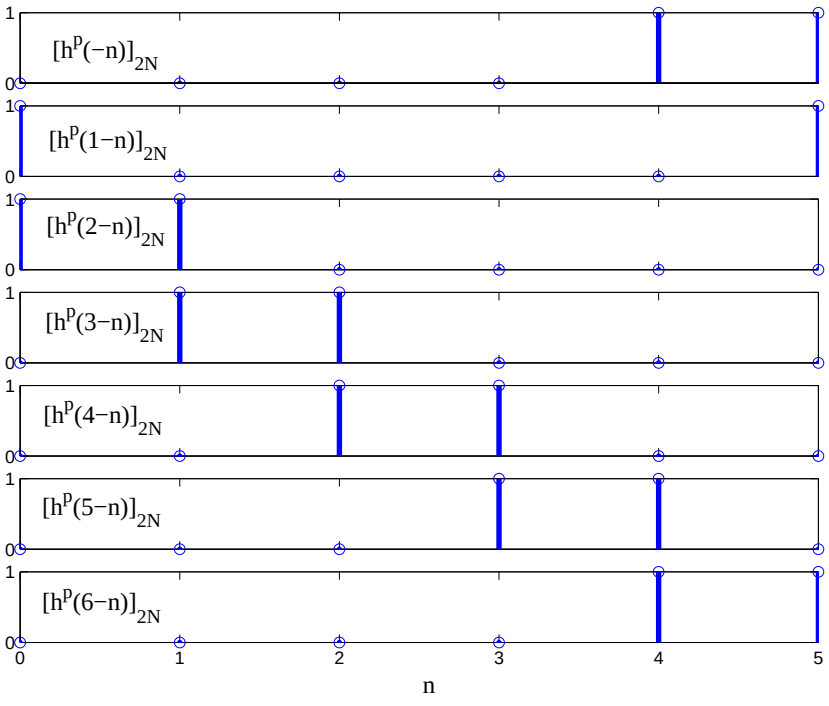

(b) Circular shift

Figure 4.6: Shift and circular shift of the zero-padded temporal series $h^p(n)$

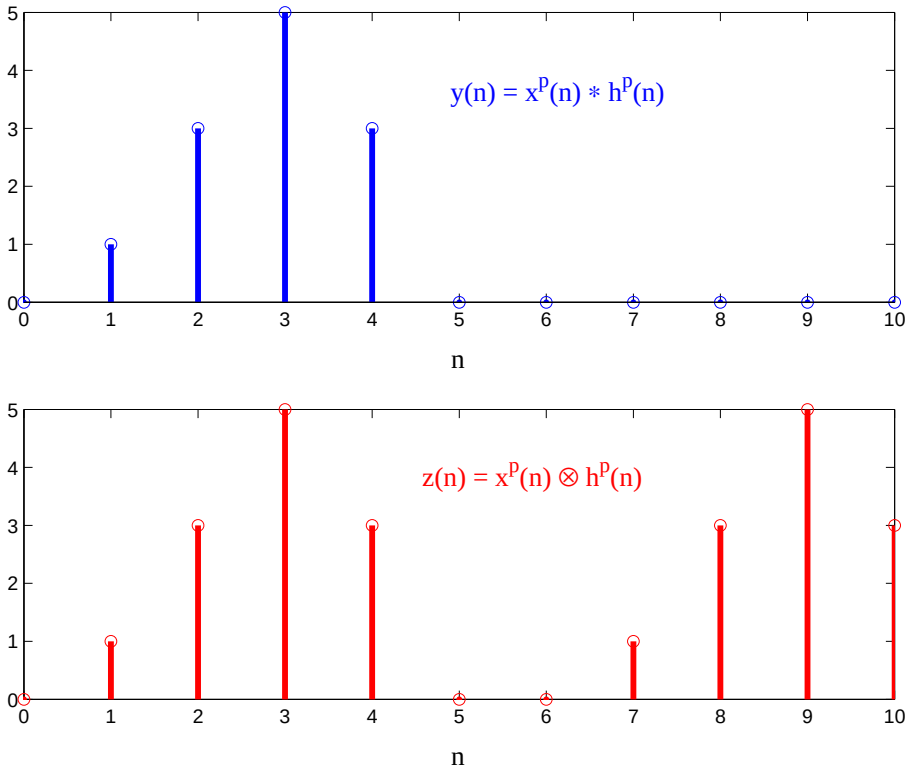

Figure 4.7: Linear convolution is equivalent to circular convolution for the zero-padded temporal series

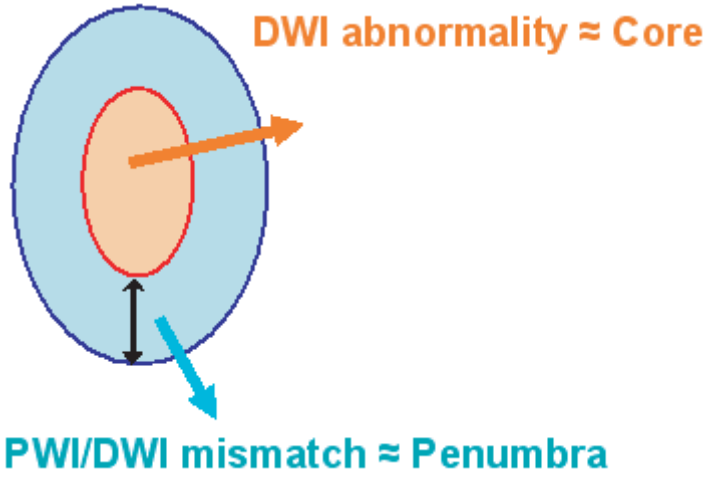

Figure 4.8: Schematic of the definitions of the ischemic core and penumbra.

4.6 Results

4.6.1 Acute Stroke Patient Study

Images were acquired from five acute stroke patients (three males, three females, age 63-78). All five acute stroke patients have DWI and PWI abnormalities within the anterior, posterior, or middle cerebral artery territory during the acute phase of stroke.

The rMTT map of the same slice of the same acute stroke patient shown in Fig. 4.2 are illustrated in Fig. 4.9. The green line delineates the boundary of the acute PWI-defined abnormality. Fig. 4.10 demonstrates the global AIFs measured from the contralateral MCA (cMCA) and ipsilateral MCA (iMCA).

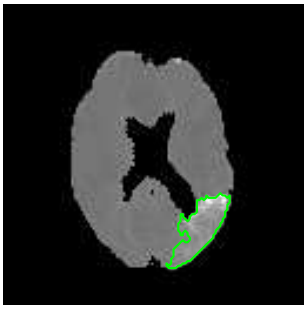

Figure 4.9: The rMTT map of the same acute stroke patient shown in Fig. 4.2

The procedure of using spatial ICA analysis to identify local arterial spatial sources is demonstrated in Fig. 4.3. Nonarterial components were discarded on the basis of both their spatial maps (see, for example, IC1, IC6, IC8 and IC9 in Fig. 4.4(a)) and temporal characteristics (see, for example, IC10 in Fig. 4.3(b)). Subsequently, local AIF dataset was constructed using the remaining arterial components. Finally, VTF was estimated for each voxel using cSVD.

Fig. 4.11 shows the predefined ROIs. For example, the acute PWI abnormality as shown in Fig. 4.9 may further be divided into two ROIs: a core ROI (blue in Fig.4.11(a)) which is defined as the acute PWI abnormal region that appears abnormal on the acute DWI image, as well as a PWI/DWI mismatch ROI (red in Fig.4.11(a)) which refers to the region with reduced perfusion but appears normal on acute DWI image. For comparison purpose, a contralateral ROI (green) was also defined as shown in Fig.4.11(a) and a follow-up T_2

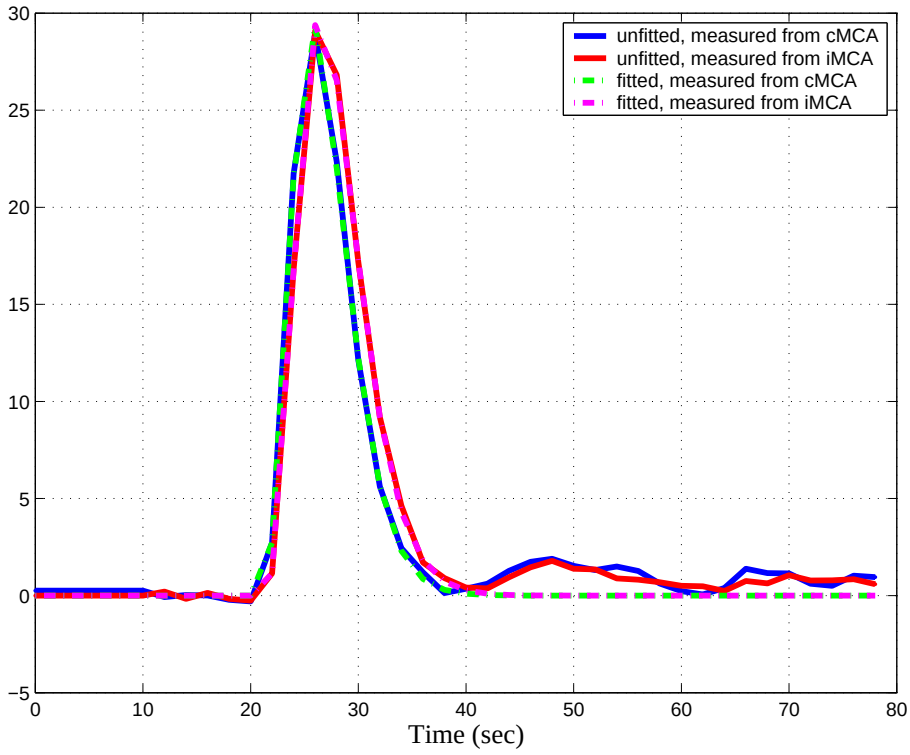

Figure 4.10: Global AIFs for the same acute stroke patient shown in Fig. 4.2

infarction ROI (yellow) is illustrated in Fig.4.11(b).

The averaged VTF in the core (blue solid line), PWI/DWI mismatch (red dash-dotted line), and final T_2 infarction (yellow plus line) regions are shown in Fig. 4.12(a) and Fig. 4.12(b) with the global AIF respectively measured from the cMCA and iMCA. From Fig. 4.12, the mean VTF in the PWI/DWI mismatched region is less dispersed, suggesting the VTF should have narrower FWHM and higher EVTF in PWI/DWI mismatch region.

Fig. 4.13 displays the acute DWI, acute rMTT and follow-up T_2 images acquired from one slice of another acute stroke patient. The global AIFs are shown in Fig. 4.14 where the CGAIF leads the IGAIF for this patient. Fig. 4.15 shows the spatial ICA analysis results. The highly expressed voxels and the temporal characteristics of each of the ten components are demonstrated in Fig. 4.15(a) and Fig. 4.15(b), respectively. IC2, IC3 and IC4 are identified as arterial spatial sources. In contrast, lesion components (for example, IC5 and IC6), tissue/venous components (for example, IC1) and other nonarterial

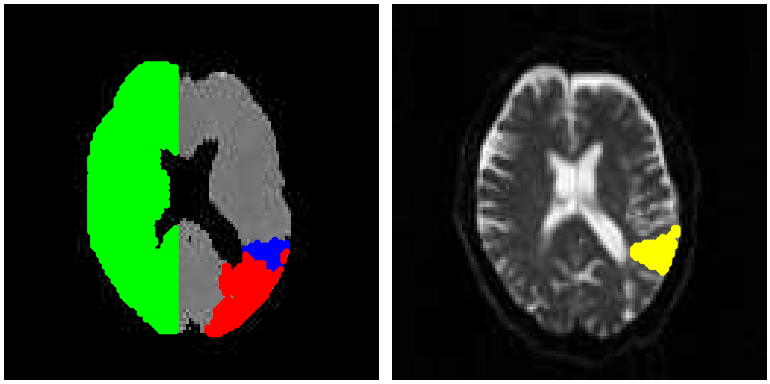

(a) Blue:core, red:PWI/DWI mismatch, green:contralateral ROI

(b) Final T_2 infarction

Figure 4.11: Different ROIs defined for the same acute stroke patient shown in Fig. 4.2,

components (for example, IC7, IC8, IC9 and IC10) were discarded on the basis of both their spatial maps and temporal characteristics. Subsequently, local AIF dataset was constructed using arterial components and voxel-by-voxel VTF was estimated.

In order to illustrate how VTF differs among different regions, three voxels were chosen as shown in Fig. 4.16(a), Fig. 4.16(b) and Fig. 4.16(c): one from the core (blue dot), one from the PWI/DWI mismatch area (red dot), and the other from final T_2 infarction (yellow dot). A direct comparison of VTF obtained from the core (blue solid), PWI/DWI mismatch (red dash-dot line), and final T_2 infarction (yellow plus line) when CGAIF and IGAIF were used, are shown in Fig. 4.16(d)and Fig. 4.16(e), respectively. Although, the VTFs have similar FWHM, the VTF in the PWI/DWI mismatched region has the largest EVTF, which is consistent with the finding shown in Fig. 4.12.

4.6.2 Statistical Analysis

Results obtained from the ROI analysis are summarized in Fig. 4.17 for three normal volunteers (one male, two females, age 24-33) for comparison purpose. For normal volunteer study, the FWHM obtained from the two ROIs are 4.08 ± 0.80 sec and 4.07 ± 0.89 sec, respectively. Moreover, the EVTF values obtained from the two ROIs are comparable

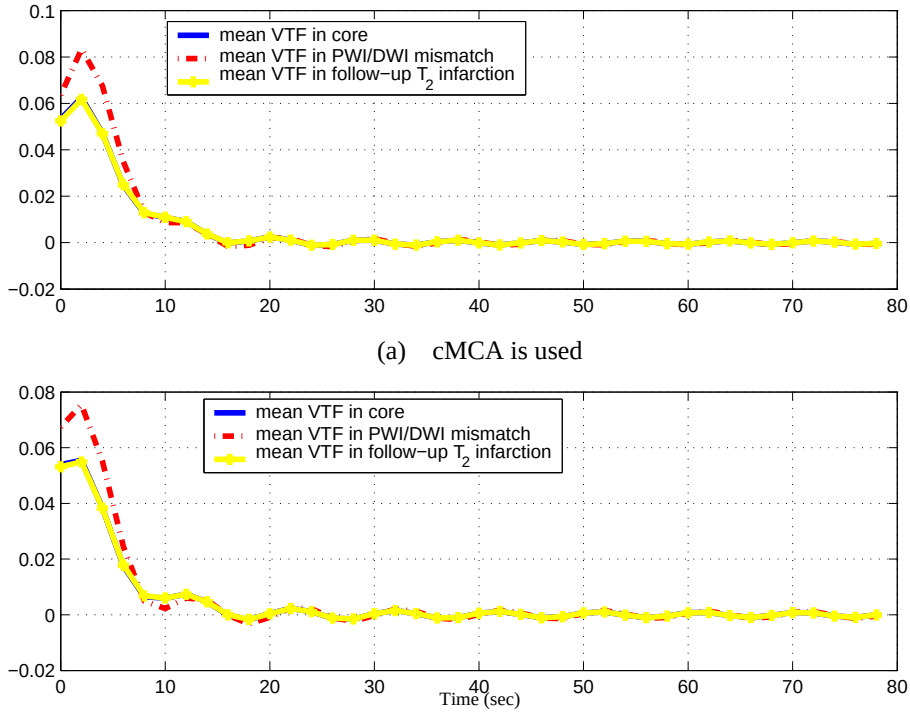

(a) cMCA is used

(b) iMCA is used

Figure 4.12: Averaged VTFs in different ROIs for the same acute stroke patient shown in Fig. 4.2

with a normalized EVTF of 0.96 ± 0.24. It is clear that for the normal volunteer study, the VTF obtained from the two hemispheres have similar dispersion and energy.

In the acute stroke patient study, the results of the FWHM are summarized in Table 4.1. When the CGAIF is used, as shown in Fig. 4.18(a), the contralateral ROI yields the smallest FWHM of 8.49 ± 1.05s, while the core (10.39 ± 1.79s), PWI/DWI mismatch (10.52 ± 1.87s) and the final infarction (10.49 ± 1.83s) have similar FWHM, suggesting more bolus dispersion is observed in the ipsilateral hemisphere. Similar results are also observed from Fig. 4.18(b) when IGAIF is used: 7.43 ± 0.95s, 9.01 ± 0.97s, 9.15 ± 1.08s, and 9.09 ± 0.99s for the contralateral, core, PWI/DWI mismatch, and final infarction, respectively.

The results of the normalized EVTF are summarized in Table 4.2 for the stroke patients. When CGAIF is used as shown from Fig. 4.19(a), the PWI/DWI mismatched region has the largest EVTF ($75.12 \pm 16.79\%$). The EVTF of the core ($64.48 \pm 17.67\%$) is statistically smaller than that obtained from the PWI/DWI mismatched region ($P =$

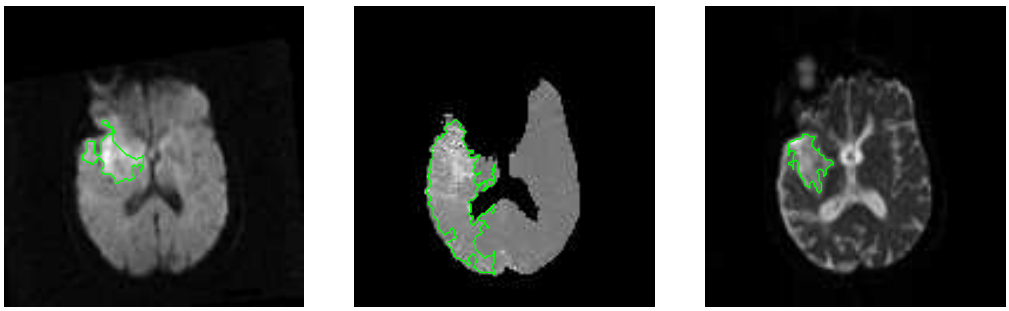

(a) Acute DWI (b) Acute rMTT (c) Follow-up T_2

Figure 4.13: Anatomical images of another acute stroke patient

	core	PWI/DWI mismatch	final infarction	contralateral ROI
CGAIF	10.39 ± 1.79	10.52 ± 1.87	10.49 ± 1.83	8.49 ± 1.05
IGAIF	9.01 ± 0.97	9.15 ± 1.08	9.09 ± 0.99	7.43 ± 0.95

Table 4.1: FWHM (sec) of the VTF for the patient study

0.0319). Moreover, the EVTF in regions of the follow-up T_2-defined infarction ($64.07 \pm 17.20\%$) is also substantially reduced and is statistically smaller than that obtained from the PWI/DWI mismatched region ($P = 0.0465$). Similar results are demonstrated in Fig. 4.19(b) when IGAIF is used. The PWI/DWI mismatched region has the largest EVTF ($73.09 \pm 14.36\%$). The EVTF of the core ($62.99 \pm 18.64\%$) and the EVTF in regions of the follow-up T_2-defined infarction ($62.99 \pm 18.21\%$) are substantially reduced and are statistically smaller than that obtained from the PWI/DWI mismatched region with $P = 0.0141$ and $P = 0.0229$ respectively.

In summary, VTF can be obtained using the proposed approach. For normal

	core	PWI/DWI mismatch	final infarction
CGAIF	64.48 ± 17.67	75.12 ± 16.79	64.07 ± 17.20
IGAIF	62.99 ± 18.64	73.09 ± 14.36	62.99 ± 18.21

Table 4.2: Normalized EVTF (%) of the VTF for the patient study

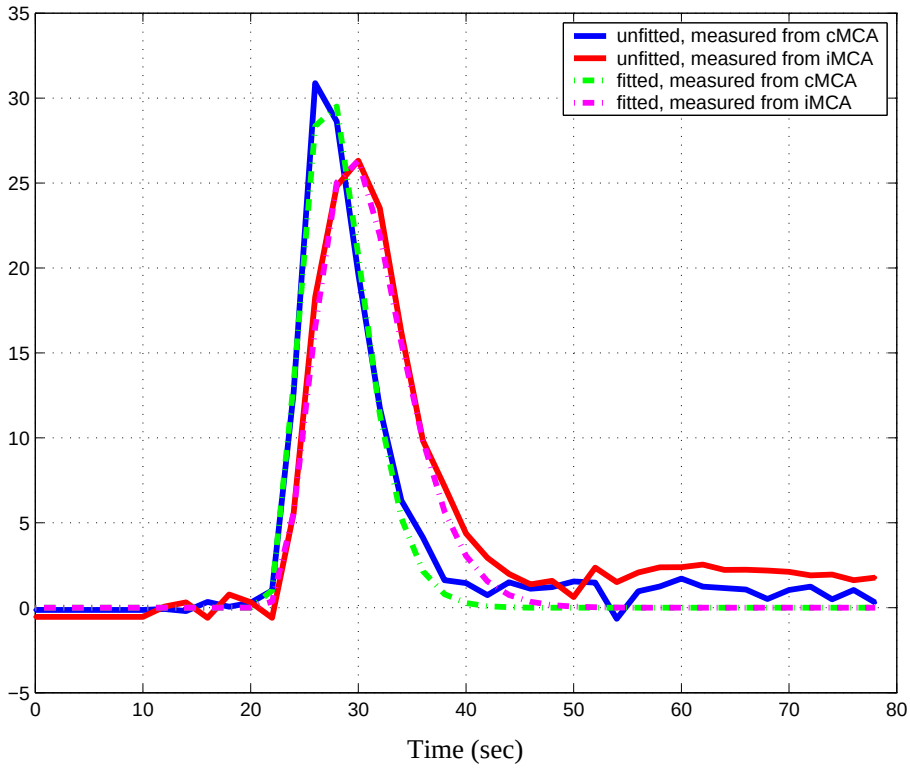

Figure 4.14: Global AIFs measured from MCAs for the same acute stroke patient shown in Fig.4.13

volunteers, the VTF obtained in the two hemispheres were determined similar. In contrast, discrepancies were observed for different regions in acute stroke patient study. Although, the FWHMs in all three ipsilateral ROIs are much larger than that obtained in the contralateral ROI, our results demonstrated that the core and the final T_2 infarction exhibited much smaller power in comparison to that obtained in other brain regions in stroke patients. This is consistent with the hypothesis that in humans DWI abnormality is the marker of ischemic infarction, while PWI/DWI mismatch is an estimate of the at-risk but still viable tissue which may be salvaged if perfusion is restored on time. Although our study has a limited sample size, we have demonstrated that the VTF may provide an alterative means of assessing tissue perfusion status.

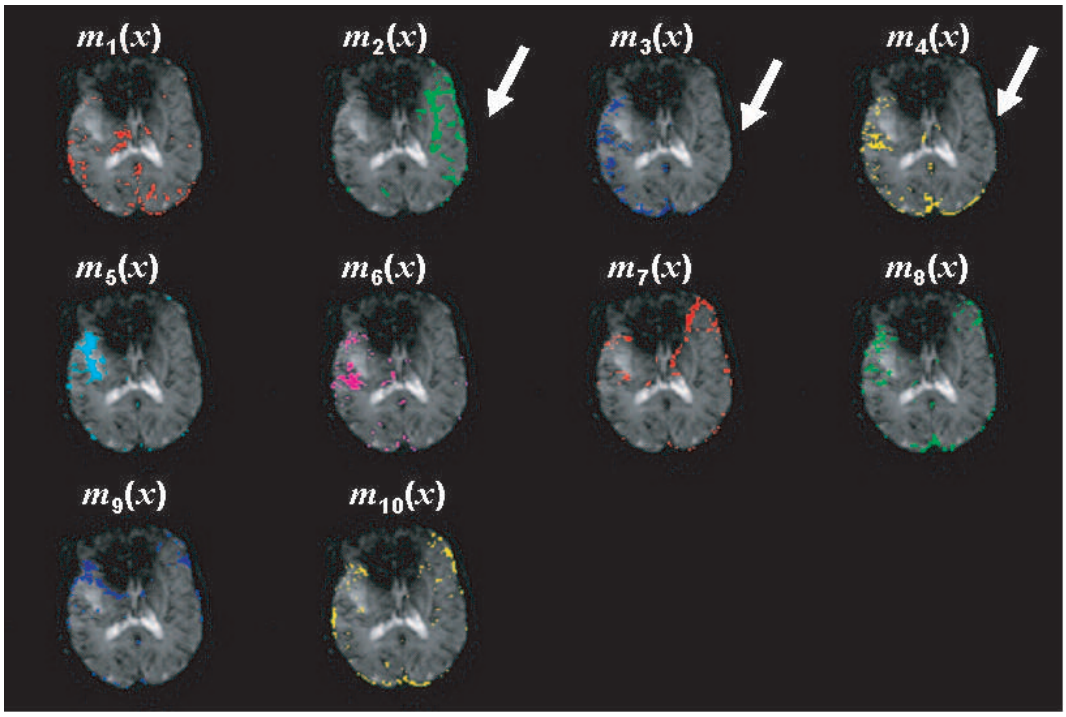

(a) Highly expressed voxels overlaid on the acute PWI images

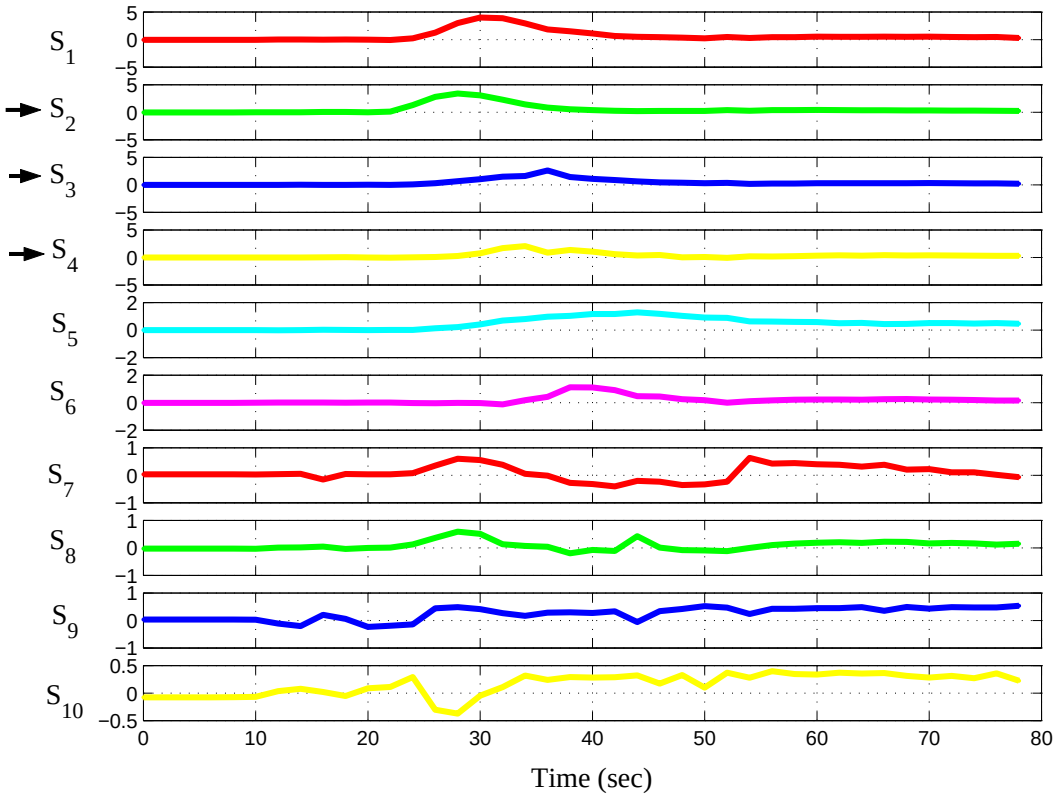

(b) Temporal characteristics of the spatial components

Figure 4.15: Spatial ICA analysis of the DSC perfusion data acquired from the same acute stroke patient shown in Fig.4.13

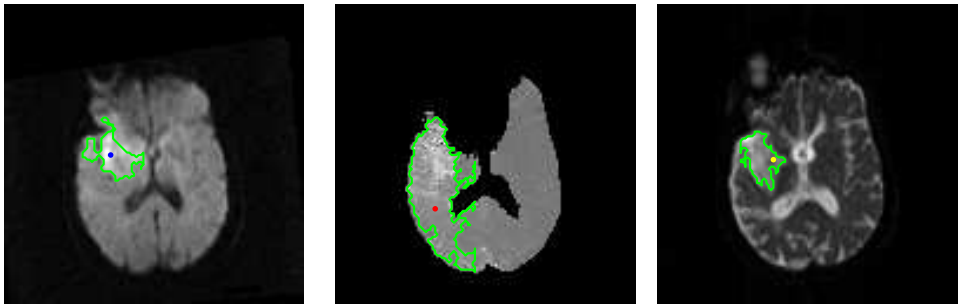

(a) A core voxel (b) A PWI/DWI mismatch voxel (c) A final infarction voxel

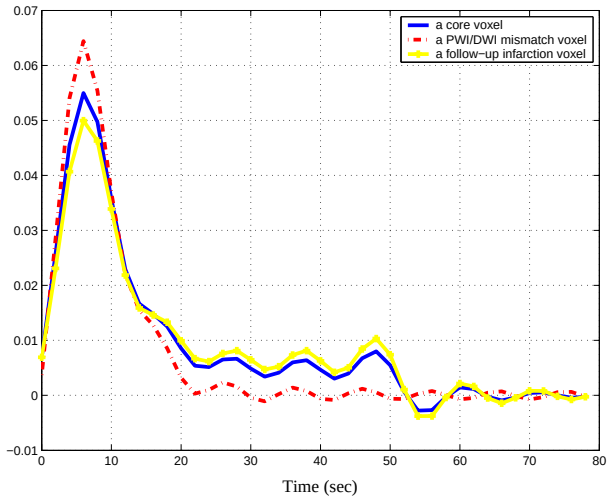

(d) GAIF was measured from cMCA

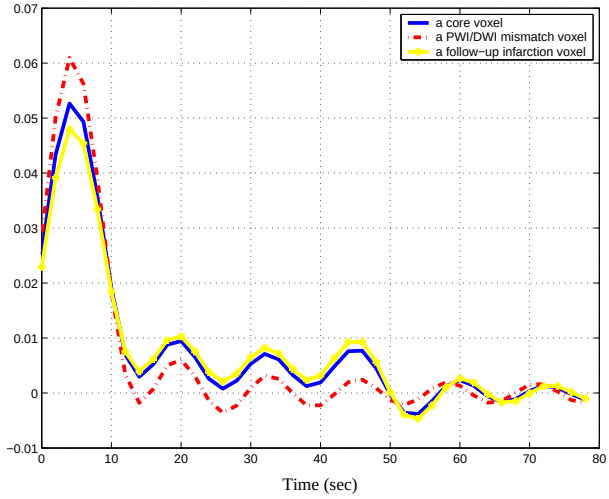

(e) GAIF was measured from iMCA

Figure 4.16: VTF variation at different voxels for the same acute stroke patient shown in Fig.4.13

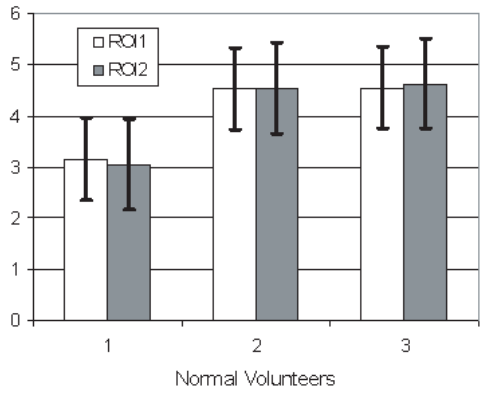

(a) FWHM (sec)

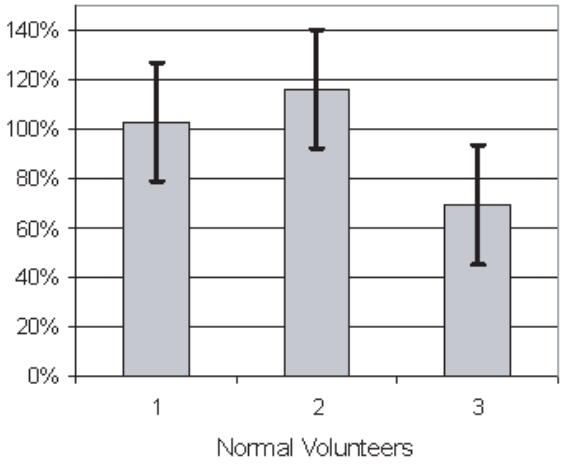

(b) Normalized EVTF (%)

Figure 4.17: FWHM (sec) and normalized EVTF (%) of VTF for the normal volunteer study

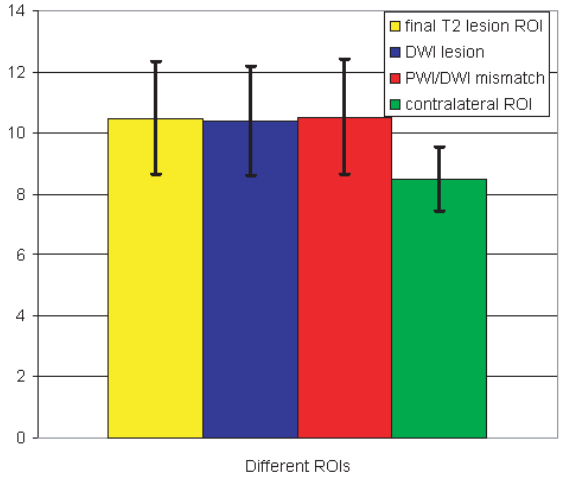

(a) GAIF was measured from cMCA

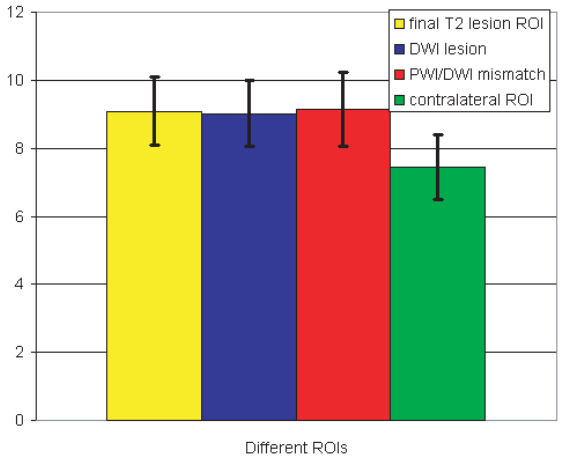

(b) GAIF was measured from iMCA

Figure 4.18: FWHM (sec) of VTF for the acute stroke patient study

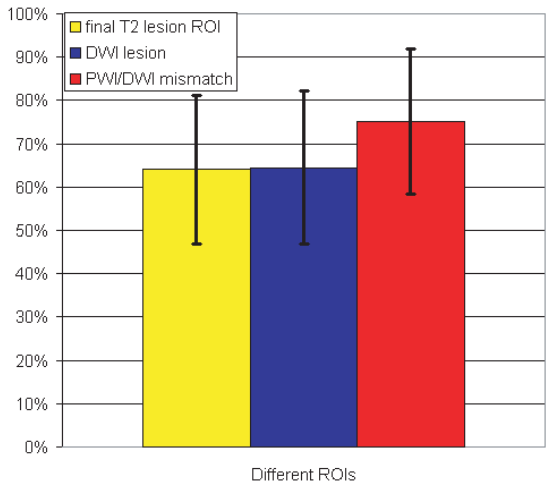

(a) GAIF was measured from cMCA

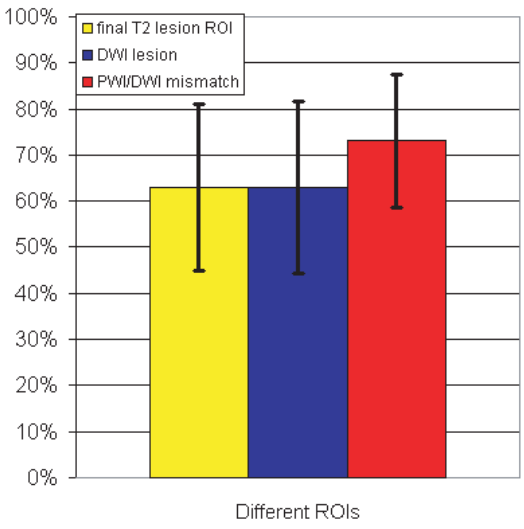

(b) GAIF was measured from iMCA

Figure 4.19: Normalized EVTF (%) of VTF for the acute stroke patient study

Chapter 5

Modelling Cerebral Blood Flow Heterogeneity using DSC MR Data

5.1 Introduction

Using SVD, it has been shown that bolus delay and dispersion between the AIF and tissue concentration curves may induce flow quantification error. While bolus delay effects may be minimized by using a deconvolution method [6] or by defining ICA-based local arterial input functions [33], [71], bolus dispersion may not be corrected for without the knowledge of vasculature of the blood vessel bed.

A mathematical modelling tool describing the delay and dispersion of material being transported within the blood was first developed by King *et al.* [72, 73]. Wilke *et al.* [74] and Kroll *et al.* [75] later applied the derived coronary circulation model to MR data to measure myocardial blood flow noninvasively. The arteriolar and capillary compartments in their models were described separately by assigning fixed relative dispersion and variable volumes to the arteriolar vascular paths, and a fixed volume to the capillary bed. Østergaard *et al.* [52] extended the vascular model to cerebral circulation to obtain flow rates independently of major vessel delay and dispersion. Since the capillary density

[6] This method is less sensitive to bolus delay.

varies greatly among different tissues in the brain, to obtain a robust model for all brain tissues with the same basic model parameters, the microvascular volume was made a free parameter in [52]. And it was assumed that the dispersion only takes place in the large vessel.

Using ICA, local arterial sources may be identified by applying spatial ICA to tissue curves throughout the entire brain parenchyma. In this study, we extended the cerebral vascular model to separate the vasculature between the major vessel and the tissue of interest further into two parts. The first part between the major vessel and local vessel were modelled as parallel small arteries and the second part between the local vessel to the tissue was modelled as parallel capillaries. By adjusting the input mean flow rate, the volumes of small arteries and capillaries, and the local flow rates in each small artery and each capillary, flow heterogeneity in both small arteries and capillary bed may be modelled and thus the bolus delay and dispersion dependence on cerebral flow estimation may be minimized.

The vascular model was fitted to normal rat cerebral MR data for validation purposes. The estimated flow rates were also compared to established values and those obtained using the SVD method. In addition, using numerical simulation, the sensitivity of the vascular model to tracer delays was compared to that of the SVD approach. The results demonstrate that the developed model yields gray matter (GM) to white matter (WM) flow ratios in good agreement with the established values, as well as those obtained by the SVD method.

5.2 Vascular Model

We built on the vascular model previously described by Kroll *et al.* [75] and Østergaard *et al.* [52] to normal rat cerebral MR data. Let $C_{ga}(t)$ and $C_{la}(t)$ be the AIFs measured at a major vessel and a local vessel respectively. In addition, let $C_T(t)$ be the measured tissue residue curve. The vasculature between the major vessel and any local vessel was modelled as 5 small vessels in parallel as shown in Fig. 5.1. Each small artery was modelled as a delay line with the delay determined by the volume V_{sv}. The vasculature between any local vessel and the tissue of interest was, in contrast, modelled as 6 capillaries in parallel. Each capillary was modelled as a delay line with the delay determined by the fractional vol-

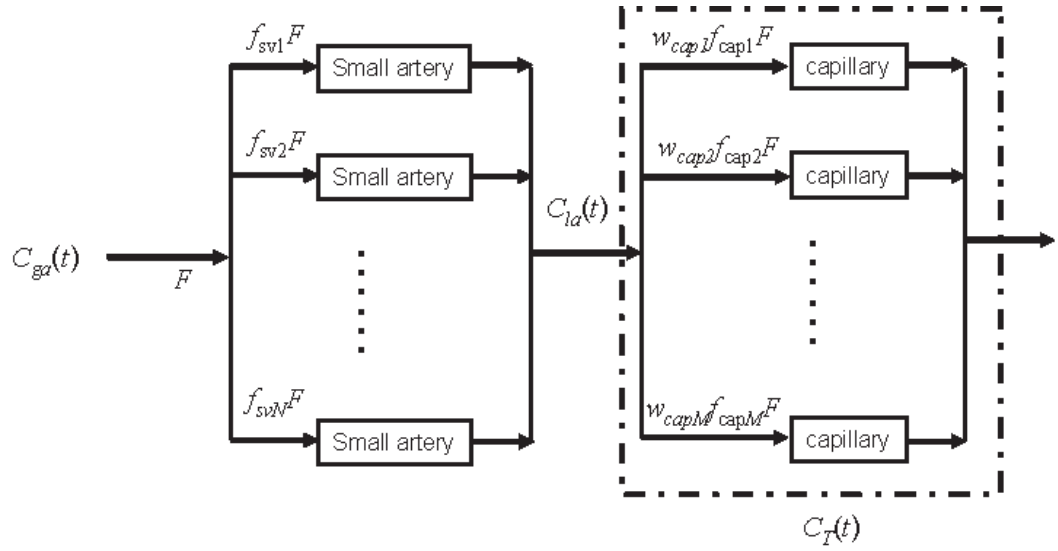

Figure 5.1: Overview of our cerebral vascular model

ume V_{cap} and a relative dispersion [72]. By characterizing the model by several parameters, more stable flow rates may be obtained in comparison to the conventional SVD approach.

5.2.1 Modelling Small Arteries

A global AIF, $C_{ga}(t)$, was measured from signal changes at a major vessel such as middle cerebral artery. Assuming the observed tissue curves can be decomposed into spatially segregated and independent components, spatial ICA was applied to tissue curves throughout the brain parenchyma. A local AIF dataset was then constructed using the arterial sources determined on the basis of both spatial maps and temporal characteristics of the components.

The pathway between the global AIF and any local AIF, $C_{la}(t)$, may be modelled as N parallel small arteries. In this study, N was fixed to 5 to reduce the computational complexity. Each small artery was then modelled as a pure delay line with delay τ_{sv_i} $(i = 1, \cdots, N)$. Let F be the mean input bulk blood flow measured in ml/min. The input flow is then directed to N pathways in parallel, and flow heterogeneity is achieved by assigning a relative local bulk blood flow f_{sv_i} $(0 < f_{sv_i} < 1)$ to each small artery. In one minute, $f_{sv_i}F$

ml of blood can be delivered through the i^{th} small artery. We thus have $\sum_{i=1}^{N} f_{sv_i} F = F$, or

$$\sum_{i=1}^{N} f_{sv_i} = 1. \tag{5.1}$$

Also assume each small artery has the same bulk blood volume V_{sv} (ml), hence, in $V_{sv}/f_{sv_i}F$ minutes, V_{sv} ml of blood can be delivered through the i^{th} small artery. The delay for the i^{th} small artery is thus

$$\tau_{sv_i} = V_{sv}/f_{sv_i}F \ \ (sec). \tag{5.2}$$

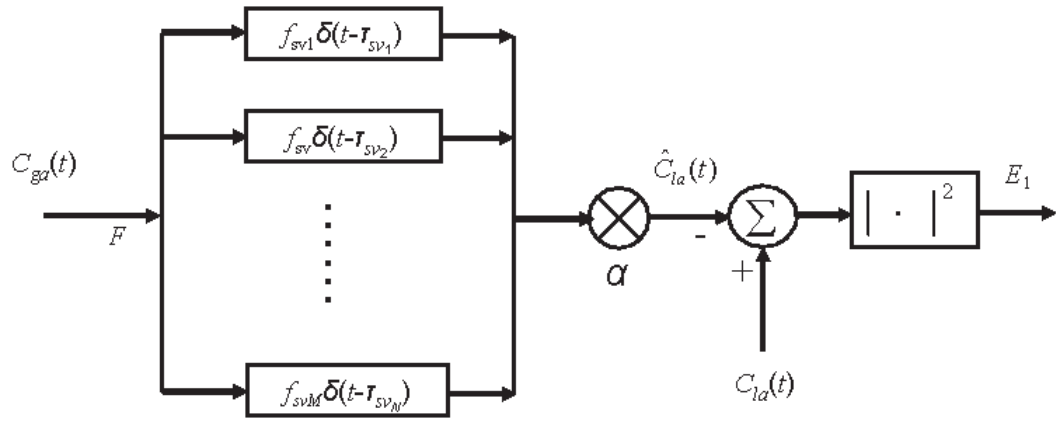

Figure 5.2: Cerebral vascular model for small arteries

Since in one minute, $f_{sv_i}F$ ml bulk blood can be delivered through the i^{th} small artery, the concentration of the contrast agent in that small artery, thus, should be proportional to f_{sv_i} $(i = 1, \cdots, N)$. In addition, considering that the global AIF can deliver blood to hundreds of small local AIFs in the brain, there is no mass conservation for any pair of the global AIF and any particular local AIF. As shown in Fig. 5.2, the estimated local AIF and the estimation error are then reflected by Eqs. (5.3-5.4) respectively,

$$\hat{C}_{la}(t) = \sum_{i=1}^{N} \alpha f_{sv_i} C_{ga}(t - \tau_{sv_i}) \ \ (0 < \alpha < 1), \tag{5.3}$$

$$E_1 = |C_{la}(t) - \hat{C}_{la}(t)|^2. \tag{5.4}$$

5.2.2 Modelling Tissue Residue Functions

Tissue curve, $C_T(t)$, was measured either from a gray matter or white matter voxel. The pathway through the local vessel to the tissue may be modelled as M parallel capillaries. Each capillary was then modelled as a pure delay line followed by a dispersion filter. In this study, M was fixed to 6 to reduce computational complexity.

Assuming F ml of blood is delivered to 100 g of tissue of interest in one minute, let f_{cap_i} be the relative local perfusion flow in the i^{th} capillary. In addition, let w_{cap_i} be the fraction of the tissue having local flow $f_{cap_i}F$, i.e. if the total tissue mass is 100 g, then the mass of the i^{th} capillary is $100w_{cap_i}$ g. We thus have,

$$\sum_{i=1}^{M} w_{cap_i} = 1. \tag{5.5}$$

Similarly, since in one minute, F ml of blood can be delivered to the tissue of interest, we have $\sum_{i=1}^{M} w_{cap_i} f_{cap_i} F = F$, or

$$\sum_{i=1}^{M} w_{cap_i} f_{cap_i} = 1. \tag{5.6}$$

Assume each capillary has the same volume V_{cap} (ml/100g) and the same relative dispersion (RD), RD_{cap}. Each capillary may be modelled as a delay operator with delay of τ_{cap_i} sec followed by a Gamma filter with fixed RD of 0.48. In general, let T be a random variable with a probability density function $h(t)$ defined on $[0, a]$ with mean $\bar{t}$ and standard deviation σ. The relative dispersion of $h(t)$ is defined as $RD = \sigma/\bar{t}$.

Let the impulse response of each Gamma filter be $G_i(a_i, b_i, t)$ which is given by:

$$G_i(a_i, b_i, t) = \frac{1}{b_i^{a_i}\Gamma(a_i)} t^{a_i - 1} e^{-t/b_i} \quad (a_i > 0, b_i > 0, t \geq 0). \tag{5.7}$$

The mean and variance of the Gamma filter are $\bar{t}_{\Gamma_i} = a_i b_i$ and $\sigma_{\Gamma_i} = b_i\sqrt{a_i}$ respectively. Then the relative dispersion of each Gamma filter is:

$$0.48 = \sigma_{\Gamma_i}/\bar{t}_{\Gamma_i} = 1/\sqrt{a_i}. \tag{5.8}$$

Let the MTTs for each capillary and the Gamma filter be $\bar{t}_{cap_i}$ (sec) and $\bar{t}_{\Gamma_i}$ (sec), respectively. Then $\bar{t}_{cap_i}$ is given by:

$$\bar{t}_{cap_i} = \frac{V_{cap}}{f_{cap_i} F} = \tau_{cap_i} + \bar{t}_{\Gamma_i} \ \ (sec). \tag{5.9}$$

Since the delay line is not dispersive, the standard deviation of each capillary is thus equal to that of each Gamma filter. The RD of each capillary is thus given by:

$$RD_{cap} = \sigma_{\Gamma_i}/\bar{t}_{cap_i} = 0.48\bar{t}_{\Gamma_i}/\bar{t}_{cap_i} = 0.48 a_i b_i/\bar{t}_{cap_i}. \tag{5.10}$$

From Eqs. (5.8, 5.10), we can adjust the parameters of the Gamma filter to obtain any desired RD ($0 < RD \leq 0.48$) for each capillary:

$$a_i = 1/(0.48)^2, b_i = 0.48 \cdot RD_{cap} \cdot \bar{t}_{cap_i} \ \ (i = 1, \cdots, M), \tag{5.11}$$

$$\bar{t}_{\Gamma i} = \bar{t}_{cap_i} \cdot RD_{cap}/0.48 \ \ (i = 1, \cdots, M), \tag{5.12}$$

$$\tau_{cap_i} = \bar{t}_{cap_i} - \bar{t}_{\Gamma i} = (0.48 - RD_{cap}) \cdot \bar{t}_{cap_i}/0.48 \ \ (i = 1, \cdots, M). \tag{5.13}$$

As shown in Fig. 5.3, the output of the capillary bed is given by:

$$C_{capout}(t) = \sum_{i=1}^{M} w_{cap_i} f_{cap_i} C_{la}(t - \tau_{cap_i}) \otimes G_i(a_i, b_i, t). \tag{5.14}$$

The estimated relative residue tracer mass, $\hat{Q}_T(t)$ (mg/ml), is given by Eq. (5.15), which may be viewed as the approximation of the measured residual tracer concentration, $C_T(t)$, in the tissue.

$$\hat{Q}_T(t) = F \int_0^t C_{la}(\tau) d\tau - F \int_0^t C_{capout}(\tau) d\tau. \tag{5.15}$$

The error between the estimated residue tracer mass and the measured tissue residual is then:

$$E_2 = |C_T(t) - \hat{Q}_T(t)|^2. \tag{5.16}$$

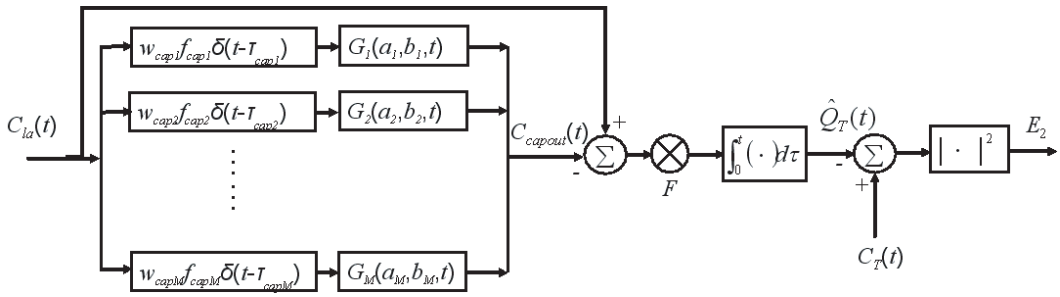

Figure 5.3: Cerebral vascular model for capillary bed

5.2.3 Model Analysis

In the physiological literature, the CBF and CBV values in gray matter and white matter are different. Different initial conditions, lower and upper bounds should be used to separate GM and WM. Gray matter and white matter ROIs were segmented based on cerebral blood volume maps ([11, 76, 77]). Using Matlab optimization toolbox, F, V_{sv}, V_{cap} and RD_{cap} were adjusted to obtain optimal fits to both the local AIF and the tissue concentration curve by minimizing the error $E_1 + E_2$ subject to the following constraints: $0 < \alpha < 1$, $\sum_{i=1}^{N} f_{sv_i} = 1$, $\sum_{i=1}^{M} w_{cap_i} = 1$, and $\sum_{i=1}^{M} w_{cap_i} f_{cap_i} = 1$.

For normal rat gray matter tissue, the typical values of the parameters are: F = 100∼140 ml/100g/min, V_{sv} = 0.6∼ 1.5 ml/100g, and V_{cap} = 0.75∼2.2 ml/100g. The initial conditions were F = 120 ml/100g/min, V_{sv} = 1 ml/100g, V_{cap} = 1.5 ml/100g and RD_{cap} = 0.1. For normal rat white matter, the typical values of the parameters are: F= 40∼80 ml/100g/min, V_{sv} = 0.4∼0.9 ml/100g, V_{cap} = 0.55∼1.3 ml/100g. The corresponding initial conditions were F = 55 ml/100g/min, V_{sv} = 0.65 ml/100g, V_{cap} = 0.9 ml/100g and RD_{cap} = 0.1 for normal rat white matter tissue.

5.3 Model Validation

Tissue curves were obtained from gray matter and white matter voxels respectively. And CBF values were also obtained by deconvolving the tissue curves with the global AIF using SVD, and were compared to those obtained with the vascular model fits. In addition,

the gray-to-white matter flow ratios obtained from the model were compared with those obtained using the SVD method.

To simulate the effects of bolus delays on flow estimation, the tissue concentration time curve measured at a gray matter voxel from one normal rat was delayed up to 2.88 seconds in steps of 0.24 second by linear interpolation. Flow rates were again obtained using the SVD method and the vascular model fits of the delayed tissue curves for comparison purpose.

5.4 Results

DSC MR data were measured from three normal rats with TR of 0.48 seconds, and TE of 13 milliseconds. A total of 120 images were acquired for each slice. Fig. 5.4 shows the global AIF measured from MCA and a constructed local AIF using spatial ICA for one normal rat. Typical tissue concentration time curves as well as the corresponding model fits obtained from a gray matter voxel and a white matter voxel are shown in Figs. 5.5-5.6 respectively. The vascular model provided excellent fits to the experimental data. Notice the model takes into account the observed earlier tracer arrival in tissue with higher flow rates (gray matter: CBF=100.15 ml/100g/min, white matter: CBF=59.46 ml/100g/min). The χ^2-values for the fits are $\chi^2 = 235.20$ and $\chi^2 = 194.81$ for the gray matter and white matter voxels respectively.

Fig. 5.7 shows the flow rates determined by the vascular model fits and the SVD approach respectively. Twelve voxels were randomly chosen from one normal rat. The mean gray matter flow rates are 119.10±20.17 ml/100g/min and 123.00±14.48 ml/100g/min with the vascular model and the SVD approach, respectively. In addition, the mean white matter flow rates are 65.42±14.24 ml/100g/min and 70.83±10.54 ml/100g/min with the vascular model and the SVD approach, respectively. As shown from Fig. 5.7, it is clear that in general, the flow rates obtained using the vascular model fits are in agreement with those obtained using SVD for normal rats.

Fig. 5.8 shows the gray-to-white matter flow ratios determined by the vascular model fits plotted against corresponding ratios in identical regions obtained by the SVD approach. Also shown is the linear regression line for the ratios: $y = 1.35x - 0.48$ ($r^2 = 0.81$). The line of identity was within the 95% confidence intervals of a common linear fit.

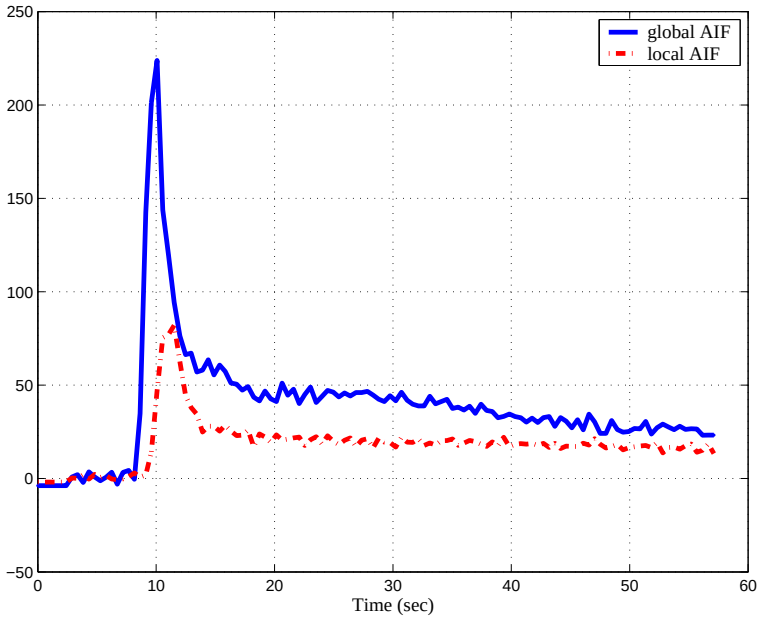

Figure 5.4: Global and local AIFs obtained from one normal rat

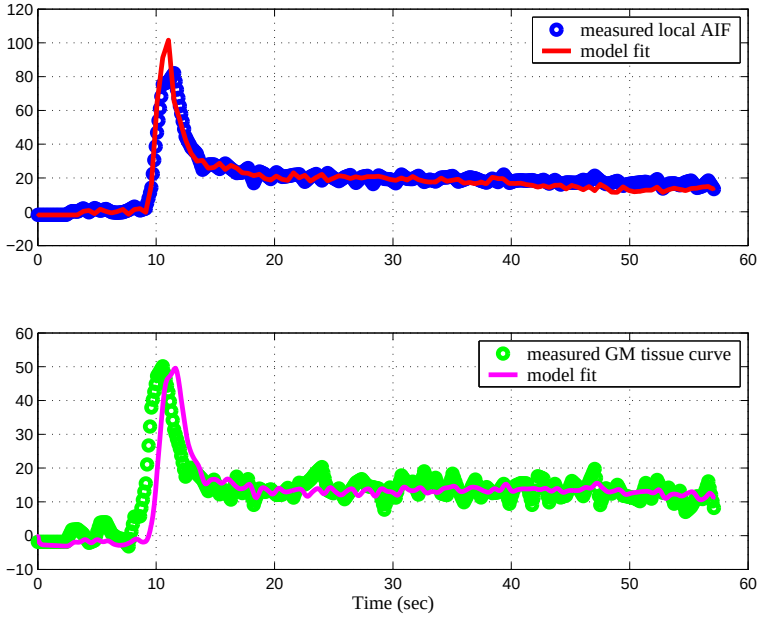

Figure 5.5: Vascular model fits for a gray matter voxel

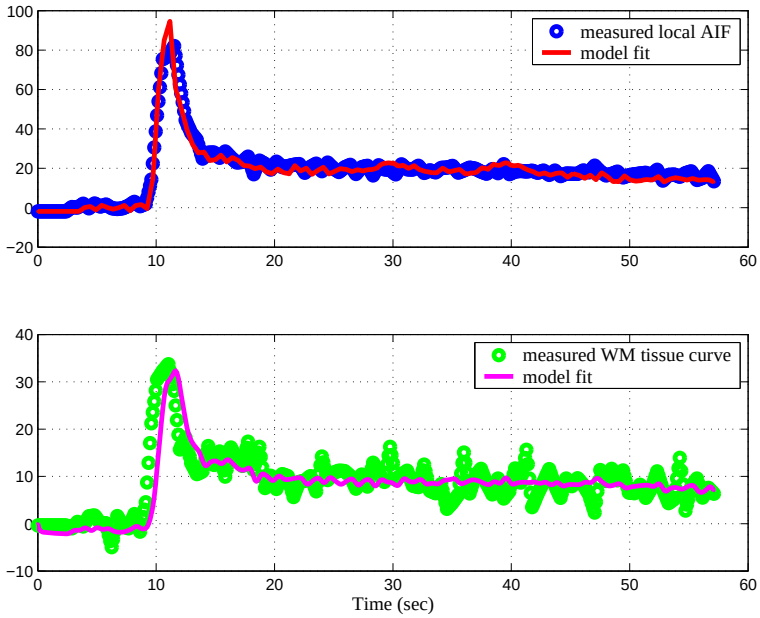

Figure 5.6: Vascular model fits for a white matter voxel

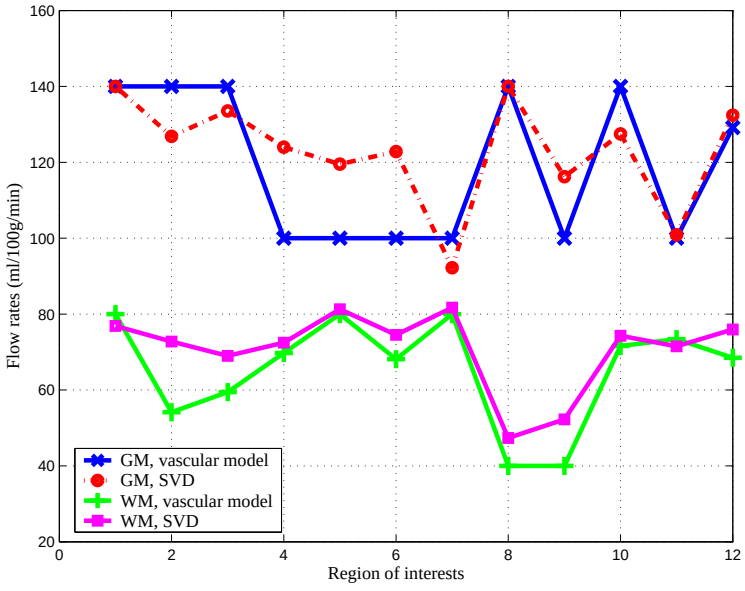

Figure 5.7: Regional flow rates by model fits and SVD approach

region	vascular model	SVD approach
1	1.75	1.82
2	2.58	1.74
3	2.35	1.94
4	1.43	1.71
5	1.25	1.47
6	1.47	1.65
7	1.25	1.13
8	3.50	2.96
9	2.50	2.22
10	1.96	1.72
11	1.36	1.41
12	1.89	1.74
mean ± SD	1.94±0.68	1.79 ± 0.46

Table 5.1: Regional GM-to-WM flow ratio in one normal rat

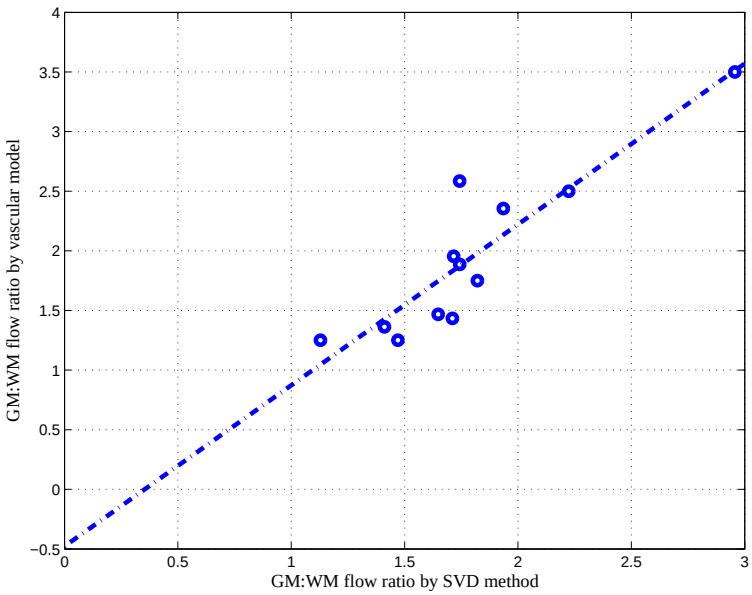

Figure 5.8: GM-to-WM flow ratio by model fits plotted against those obtained by SVD

Notice the agreement between gray-to-white flow ratios determined by the model and SVD approach, respectively. Shown in Table 5.1, the mean gray-to-white flow ratio obtained by the model fits (1.94±0.68) is in excellent agreement with that determined by the SVD approach (1.79±0.46). These values are also in agreement with values determined by PET study (2∼2.5).

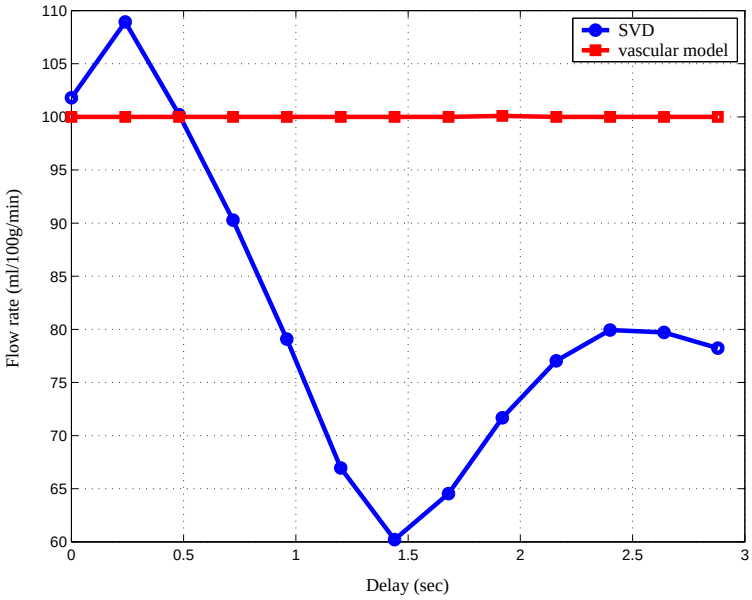

Figure 5.9: Effects of bolus delay on flow rates for the SVD approach and the vascular model respectively

Fig. 5.9 shows the effect of bolus delay on flow rates for the vascular model and the SVD approach, respectively. One gray matter voxel was chosen from a normal rat. Vascular model and SVD values were obtained from identical regions. The SVD approach substantially underestimates flow rates when tracer arrival delays are present. We remark that with a model approach, however, flow estimates are remarkably independent of delays.

In conclusion, more stable cerebral CBF quantification may be obtained by modelling flow heterogeneity in both small arteries and capillary bed. The proposed vascular model was tested on normal rat data. The results show that the model fits yield flow rates and gray-to-white matter flow ratios in agreement with both the established values and those obtained by the SVD method. Moreover, simulation shows that the vascular model is less sensitive to bolus delay in comparison to the conventional SVD approach. Although

the model is only tested on normal rat data, we have demonstrated that the vascular model may improve flow quantification greatly.

Chapter 6

Future Research Arenas

In this chapter, we briefly summarize the contributions of this dissertation, and also present some possible further development to extend our work.

6.1 Summary

Our first contribution in this work is the development of a new methodology of recirculation removal using temporal ICA for both normal and ischemic brain tissues. An alternative approach to correct bolus delay between the global AIF and tissue curves on CBF quantification is then proposed by estimating bolus arrival time for each 5×5 ROI using temporal ICA. Subsequently, a novel tool to estimate vascular transport function noninvasively based on spatial ICA is developed. The estimated VTF may offer an alternative interpretation of assessing tissue perfusion status. An extended vascular model is finally described to model cerebral flow heterogeneity. More stable flow quantification can be obtained in comparison to conventional voxel-by-voxel SVD approach.

6.2 Possible Future Research

In this section, we list several potential topics related to this thesis that might constitute good leads for future research.

In Chapter 5, we applied an extended vascular model to normal rat cerebral MR data. The vasculature between a major vessel and a tissue of interest is further separated into two parts, i.e one part describing the pathway between the major vessel to local vessel, and followed by another part describing the pathway between the local vessel to the tissue. By adjusting several parameters, the model yields flow rates in agreement with both the SVD results and established values. In addition, the model is much less sensitive to bolus delay in comparison to the conventional SVD approach. This may be further justified by applying the same model to ischemic stroke rat data. In case of ischemia, the bolus delay and dispersion between the AIF and tissue curves are more severe. The SVD approach, thus, may induce significant CBF quantification error. However, since the delay and dispersion are taken into account in the model by delay lines and Gamma filters, the vascular model approach should greatly improve CBF quantification for stroke rat data.

Bibliography

[1] Villringer A., Rosen B. R., Belliveau J. W. *et al.*, "Dynamic imaging with lanthanide chelates in normal brain: contrast due to magnetic susceptibility effects", Magnetic Resonance in Medicine, 1988, Vol. 6, pp.164–174.

[2] Østergaard L, Weisskoff RM, Chesler DA, Gyldensted C, Rosen B., "High resolution measurement of cerebral blood flow using intravascular tracer bolus passages. I. Mathematical approach and statistical analysis", Magn Reson Med 1996;36:715–725.

[3] Stewart G. N., "Researches on the circulation time in organs and the influences which affect it, part I through III", Journal of Physiology, 1894, Vol. 15, pp.1–89.

[4] Meier P. and Zierler K. L., "On the theory of the indicator-dilution method for measurement of blood flow and volume", Journal of Applied Physiology, 1954, Vol. 6, pp. 731–744.

[5] Belliveau JW, Rosen BR, Kantor HL, Rzedzian RR, Kennedy DN, McKintry RC *et al.*, "Functional cerebral imaging by susceptibility-contrast NMR", Magn Reson Med 1990;14:538–546.

[6] Axel L, "Cerebral blood flow determination by rapid-sequence computed tomography-a theoretical analysis", Radiology 1980;137:679–686.

[7] Woods RP, Cherry SR, Mazziotta JC, "Rapid automated algorithm for aligning and reslicing PET images", J Comput Assist Tomogr. 1992;16:620–633.

[8] Woods RP, Grafton ST, Holmes CJ, Cherry SR, Mazziotta JC, "Automated image registration, I: general methods and intrasubject, intramodality validation", J Comput Assist Tomogr. 1998;22:139 –152.

[9] Comon P, "Independent component analysis: a new concept?", Signal Processing 1994; 36:287–314.

[10] Schellinger PD, Fiebach JB, Hacke W., "Imaging-based decision making in thrombolytic therapy for ischemic stroke: present status", Stroke 2003;34:575–583.

[11] Rosen BR, Belliveau JW, Vevea JM, Brady TJ, "Perfusion imaging with NMR contrast agents", Magn Reson Med 1990;14:249–265.

[12] Rempp KA, Brix G, Wenz F, Becker CR, Guckel F, Lorenz WJ, "Quantification of regional cerebral blood flow and volume with dynamic susceptibility contrast-enhanced MR imaging", Radiology 1994;193:637–641.

[13] Aronen HJ, Glass J, Pardo FS, Belliveau JW, Gruber ML, Buchbinder BR, Gazit IE, Linggood RM, Fischman AJ, Rosen BR, Hochberg FH, "Echoplanar MR cerebral blood volume mapping of gliomas", Acta Radiol 1995;36:520–528.

[14] Guckel FJ, Brix G, Schmiedek P, Piepgras Z, Becker G, Kopke J, Gross H, Georgi M., "Cerebrovascular reserve capacity in patients with occlusive cerebrovascular disease: assessment with dynamic susceptibility contrast-enhanced MR imaging and the acetazolamide stimulation test", Radiology 1996;201:405–412.

[15] Østergaard L, Sorensen AG, Kwong KK, Weisskoff RM, Gyldensted C, Rosen BR, "High resolution measurement of cerebral blood flow using intravascular tracer bolus passages. II. Experimental comparison and preliminary results", Magn Reson Med 1996;36:726–736.

[16] Sorensen AG, Tievsky AL, Ostergaard L, Weisskoff RM, Rosen BR, "Contrast agents in functional MR imaging", J Magn Reson Imag 1997;7:47–55.

[17] Thompson Jr HK, Starmer F, Whalen RE, McIntosh HD, "Indicator transit time considered as a Gamma variate", Circ Res 1964;14:502–515.

[18] Davenport R, "The derivation of the gamma-variate relationship for tracer dilution curves", J Nucl Med 1983;24:945–948.

[19] Bell AJ, Sejnowski TJ, "An information-maximization approach to blind separation and blind deconvolution", Neural Comput 1995;7: 1129–1159.

[20] Cardoso JF, "Blind Signal Separation: Statistical Principles. Proc IEEE, Special Issue on Blind Identification and Estimation", 1998;90, 2009–2026.

[21] Hyvärinen A, Oja E, "A fast fixed-point algorithm for independent component analysis", Neural Comput 1997;9:1483–1492.

[22] Hyvärinen A, Oja E, "Independent component analysis: algorithms and applications", Neural Networks 2000;13:411–430.

[23] Hyvärinen A, Karhunen J, Oja E, "Independent component analysis", New York: John Wiley & Sons; 2001.

[24] Hyvärinen A., "Fast and Robust Fixed-Point Algorithms for Independent Component Analysis", IEEE Transactions on Neural Networks 10(3):626–634, 1999.

[25] Biswal BB, Ulmer JL, "Blind source separation of multiple signal sources of fMRI data sets using independent component analysis", J Comput Assist Tomogr 1999;23:265–271.

[26] McKeown MJ, Makeig S, Brown GG *et al.*, "Analysis of fMRI data by blind separation into independent spatial components", Hum Brain Map 1998; 6:160–188.

[27] McKeown MJ, Sejnowski TJ, "Independent component analysis of fMRI data: examining the assumptions", Hum Brain Map 1998;6:368–372.

[28] McKeown MJ, Makeig S, Brown GG *et al.*, "Spatially independent activity patterns in functional MRI data during the stroop color-naming task", Proc Natl Acad Sci USA 1998;95:803–810.

[29] McKeown MJ, Hansen LK, Sejnowski TJ, "Independent component analysis of functional MRI: What is signal and what is noise?", Curr Opin Neurobiol 2003;13:620–629.

[30] Moritz C, Haughton VM, Cordes D, Quigley M, Meyerand M., "Whole-brain functional MR image activation from a finger-tapping task examined with independent component analysis", Am J Neuroradiol 2000;21:1629–1635.

[31] Arfanakis K, Cordes D, Haughton VM, Moritz CH, Quigley MA, Meyerand ME, "Combining independent component analysis and correlation analysis to probe interregional connectivity in fMRI task activation datasets", Magn Reson Imag 2000;18:921–930.

[32] Carroll TJ, Haughton VM, Rowley HA, Cordes D, "Confounding effect of large vessels on MR perfusion images analyzed with independent component analysis", Am J Neuroradiol 2002;23:1007–1012.

[33] Calamante F, Mrup M, Hansen LK, "Defining a local arterial input function for perfusion MRI using independent component analysis", Magn Reson Med 2004;52:789–797.

[34] Kao YH, Guo WY, Wu YT, Liu KC, Chai WY, Lin CY *et al.*, "Hemodynamic segmentation of MR brain perfusion images using independent component analysis, thresholding, and Bayesian estimation", Magn Reson Med 2003;49:885–894.

[35] Arfanakis K, Cordes D, Haughton VM, Carew JD, Meyerand ME, "Independent component analysis applied to diffusion tensor MRI", Magn Reson Med 2002;47:354–363.

[36] Levenberg K, "A Method for the Solution of Certain Problems in Least Squares", Quart. Appl. Math, 1944;2:164–168.

[37] Marquardt DW, "An algorithm for least squares estimation of non-linear parameters", J. Sot. Ind. Appl. Math, 1963;11:431–441.

[38] Bevington PR, "Data Reduction and Error Analysis for the Physical Sciences", second edition, New York: McGraw-Hill;1992.

[39] MacKay D.J.C, "Bayesian model comparison and backprop nets", Proc Neural Information Processing Systems 1992;4:839-846.

[40] Hansen LK, Larsen J., Kolenda T, "Blind Detection of Independent Dynamic Components", Proc IEEE ICASSP 2001;5:3197–3200.

[41] ICAML Matlab code, ISP group, DTU, http://isp.imm.dtu.dk/toolbox.

[42] Diamantaras K. I. and Kung S. Y., "Principal Component Neural Networks: Theory and Applications", NY: Wiley, 1996.

[43] Tipping M. and Biship C, "Probabilistic principal component analysis", Technical Report NCRG/97/010, Neural Computing Research Group, Aston University, September 1997.

[44] Roweis S, "EM algorithms for PCA and SPCA", Advances in Neural Information Processing Systems 1997;10:626–632.

[45] Welling M., Weber M., "A Constrained EM Algorithm for Independent Component Analysis", Neural Computation. 2001;13:677–689.

[46] Attias H., "Independent factor analysis", Neural Computation. 1999;11:803–851.

[47] van Osch MJP, Vonken EPA, Bakker CJG, Viergever MA, "Correcting partial volume artifacts of the arterial input function in quantitative cerebral perfusion MRI", Magn Reson Med 2001;45:477-485.

[48] Lin W, Celik A, Derdeyn C, An H, Lee Y, Videen T, Østergaard L, Powers WJ, "Quantitative measurements of cerebral blood .ow in patients with unilateral carotid artery occlusion: a PET and MR study", J Magn Reson Imag 2001;14:659-667.

[49] Calamante F, Gadian DG, Connelly A, "Delay and dispersion effects in dynamic susceptibility contrast MRI: simulations using singular value decomposition", Magn Reson Med 2000;44:466-473.

[50] Calamante F, Yim PJ, Cebral JR, "Estimation of bolus dispersion effects in perfusion MRI using image-based computational fluid dynamics", NeuroImage 2003;19:341-353.

[51] Wu O., Østergaard L. *et al.*, "Effects of tracer arrival time on flow estimates in MR perfusion-weighted imaging", Magnetic Resonance in Medicine. 2003;50:856–864.

[52] Østergaard L., Chesler D. A., Weisskoof R. M. *et al.* , "Modeling cerebral blood flow and flow heterogeneity from magnetic resonance residue data", Journal of Cerebral Blood Flow and Metabolism, 1999, Vol. 19, pp. 690–699.

[53] Calamante F., Gadian D. G., Connelly A., "Quantification of perfusion using bolus tracking magnetic resonance imaging in stroke: assumptions, limitations, and potential implications for clinical use", Stroke, 2002, Vol. 33, pp. 1146–1151.

[54] Østergaard L., Johannsen P., Host-Poulsen P. *et al.*, "Cerebral blood ow measurements by magnetic resonance imaging bolus tracking: comparison with [(15)O]H2O positron emission tomography in humans", Journal of Cerebral Blood Flow and Metabolism, 1998, Vol.18, pp. 935–940.

[55] Wu O., stergaard L., *et al.*, "Tracer arrival timing-insensitive technique for estimating flow in MR perfusion-weighed imaging using singular value decomposition with a block-circulant deconvolution matrix", Mag. Reson. Med., 50, 164–174, 2003.

[56] Wu Y., An h., Krim H., Lin W., "Intracranial Vascular Transfer Function in Acute Stroke Patients", Brain '05 and BrainPET '05, Amsterdam, The Netherlands, 2005.

[57] Barber PA, Darby DG, Desmond PM, *et al.*, "Prediction of stroke outcome with echo-planar perfusion- and diffusion-weighted MRI", Neurology 1998; 51:418-426.

[58] Baird AE, Benfield A, Schlaug G, *et al.*, "Enlargement of human cerebral ischemic lesion volume measured by diffusion weighted magnetic resonance imaging", Ann Neurol 1997; 41:581-589.

[59] Tong DC, Yenari MA, Albers GW, OBrien M, Marks MP, Moseley ME, "Correlation of perfusion- and diffusion-weighted MRI with NIHSS score in acute (6.5 hour) ischemic stroke", Neurology 1998; 50:864-870.

[60] Schwamm LH, Koroshetz WJ, Sorensen AG, *et al.*, "Time course of lesion development in patients with acute stroke", Stroke 1998; 29:2268-2276.

[61] Warach S, Dashe JF, Edelman RR, "Clinical outcome in ischemic stroke predicted by early diffusion-weighted and perfusion magnetic resonance imaging: a preliminary analysis", J Cereb Blood Flow Metab. 1996;16:53-59.

[62] Karonen JO, Vanninen RL, Liu Y, *et al.*, "Combined diffusion and perfusion MRI with correlation to single-photon emission CT in acute ischemic stroke: ischemic penumbra predicts infarct growth", Stroke 1999; 30:1583-1590.

[63] Sorensen AG, Copen WA, Ostergaard L, Buonanno FS, Gonzalez RG, Rordorf G, Rosen BR, Schwamm LH, Weisskoff RM, Koroshetz WJ, "Hyperacute stroke: simultaneous measurement of relative cerebral blood volume, relative cerebral blood flow, and mean tissue transit time", Radiology. 1999;210:519-527.

[64] Neumann-Haefelin T, Wittsack HJ, Wenserski F, Siebler M, Seitz RJ, Modder U, Freund HJ, "Diffusion- and perfusion-weighted MRI: the DWI/PWI mismatch region in acute stroke", Stroke. 1999;30:1591-1597.

[65] Astrup J, Siesjo BK, Symon L, "Thresholds in cerebral ischemia: the ischemic penumbra", Stroke 1981; 12:723-725.

[66] Furlan M, Marchal G, Viader F, Derlon JM, Baron JC, "Spontaneous neurological recovery after stroke and the fate of the ischemic penumbra", Ann Neurol 1996; 40:216-226.

[67] Sunshine JL, Tarr RW, Lanzieri CF, Landis DMD, Selman WR, Lewin JS, "Hyperacute stroke: ultrafast MR imaging to triage patients prior to therapy", Radiology 1999; 212:325-332.

[68] Tong DC, Albers GW, "Diffusion and perfusion magnetic resonance imaging for the evaluation of acute stroke: potential use in guiding thrombolytic therapy", Curr Opin Neurol. 2000;13:45-50.

[69] Schellinger PD, Jansen O, Fiebach JB, Heiland S, Steiner T, Schwab S, Pohlers O, Ryssel H, Sartor K, Hacke W, "Monitoring intravenous recombinant tissue plasminogen activator thrombolysis for acute ischemic stroke with diffusion and perfusion MRI", Stroke. 2000;31:1318-1328.

[70] Marks MP, Tong DC, Beaulieu C, Albers GW, de Crespigny A, Moseley ME, "Evaluation of early reperfusion and i.v. tPA therapy using diffusionand perfusion-weighted MRI", Neurology. 1999;52:1792-1798.

[71] Wu Y., An h., Krim H., Lin W, "Correcting Bolus Delay Confounds on Flow Estimations using Independent Component Analysis in Perfusion Weighted Images", ISMRM 05, Miami beach, Florida, 2005.

[72] King RB, Deussen A, Raymond GM and Bassingthwaighte JB, "A vascular transport operator", Am J Physiol 1993;265: H2196–H2208.

[73] King RB, Raymond GM and Bassingthwaighte JB, "Modeling blood flow heterogeneity", Ann Biomed Eng 1996;24: 352–372.

[74] Wilke N, Kroll K, Merkle H, Wang Y, Ishibashi Y, Xu Y, Zhang J, Jerosch HM, Muhler A and Stillman AE and *et al.*, "Regional myocardial blood volume and flow: first-pass MR imaging with polylysine-Gd-DTPA", J Magn Reson Imaging 1995;5: 227–237.

[75] Kroll K, Wilke N, Jerosch HM, Wang Y, Zhang Y, Bache RJ and Bassingthwaighte JB, "Modeling regional myocardial flows from residue functions of an intravascular indicator", Am J Physiol 1996;271: H1643–H1655.

[76] Rosen BR, Belliveau JW, Aronen HJ, Kennedy D, Buchbinder BR, Fischman A, Gruber M, Glas J, Weisskoff RM, Cohen MS, *et al.*, "Susceptibility contrast imaging of cerebral blood volume: human experience", Magn Reson Med 1991;22: 293–299.

[77] Rosen BR, Belliveau JW, Buchbinder BR, McKinstry RC, Porkka LM, Kennedy DN, Neuder MS, Fisel CR, Aronen HJ, Kwong KK, *et al.*, "Contrast agents and cerebral hemodynamics", Magn Reson Med 1991;19: 285–292.